MICROSTRUCTURE DEVELOPMENT IN LITHIUM LANTHANUM TITANATE SOLID ELECTROLYTE

Petruša Borštnar

Doctoral Dissertation
Jožef Stefan International Postgraduate School
Ljubljana, Slovenia

Supervisor: Assoc. Prof. Dr. Nina Daneu, Jožef Stefan Institute, Ljubljana, Slovenia

Evaluation Board:
Prof. Dr. Miran Čeh, Chair, Jožef Stefan Institute, Ljubljana, Slovenia
Dr. Elena Chernyshova, Member, National Institute of Chemistry, Ljubljana, Slovenia
Dr. Vesna Šrot, Member, Max Planck Institute for Solid State Research, Stuttgart, Germany

MEDNARODNA PODIPLOMSKA ŠOLA JOŽEFA STEFANA
JOŽEF STEFAN INTERNATIONAL POSTGRADUATE SCHOOL

Petruša Borštnar

MICROSTRUCTURE DEVELOPMENT IN LITHIUM LANTHANUM TITANATE SOLID ELECTROLYTE

Doctoral Dissertation

RAZVOJ MIKROSTRUKTURE V TRDNEM ELEKTROLITU NA OSNOVI LITIJEVEGA LANTANOVEGA TITANATA

Doktorska disertacija

Supervisor: Assoc. Prof. Dr. Nina Daneu

Ljubljana, Slovenia, October 2024

Acknowledgments

First, I would like to thank my supervisor Assoc. Prof. Dr. Nina Daneu for giving me an opportunity for research work and introducing me to the world of microscopy. Thank you for sharing your knowledge, providing invaluable guidance throughout the years, and offering help and support in every aspect of my doctoral studies. I am grateful for always taking the time to discuss my results, your patience, and unwavering perseverance.

I am grateful to the members of the evaluation board, Prof. Dr. Miran Čeh, Dr. Elena Chernyshova, and Dr. Vesna Šrot, for your time and effort in reviewing my dissertation.

I would like to thank Prof. Dr. Goran Dražić for all suggestions regarding simulations and insightful discussions that contributed to improving my work.

My thanks also go to David Fabijan for developing the Python scripts used for simulations and to Medeja Gec for preparing TEM samples. I am grateful to all other colleagues who contributed to my doctoral research in any way.

I would also like to thank Jan Žuntar and Blaž Jaklič for the many chats, your help with my research, and your constant positivity.

A special thanks go to Tina Radošević, Daška Mohar, Nina Kuzmić, Uroš Hribar, Lea Gazvoda, and Alja Čontala for your companionship from the very start of my PhD journey. Thank you for all the conversations and laughs shared during morning coffees and lunches. Without you, these past years would not have been nearly as enjoyable.

Last, but not least, I am very grateful for all the encouragement received from my family and friends throughout the course of my studies.

I would like to acknowledge the funding provided by the Slovenian Research Agency.

Abstract

All-solid-state batteries are one of the key technologies for future energy storage and the transition to a climate-neutral society. They offer improved safety, stability, and a broader operating temperature range compared to conventional batteries with liquid electrolyte. Perovskite $Li_{0.33}La_{0.56}\square_{0.11}TiO_3$ (LLTO) is recognized as one of the most promising solid electrolytes, however, its performance is hindered by the presence of grain boundaries, which exhibit orders of magnitude lower conductivity values than the grains. Microstructures with larger grain sizes are desirable to reduce the impact of grain boundaries and improve overall performance.

In this dissertation, LLTO samples with varying initial La:Ti ratios and excess Li were prepared with solid-state synthesis. In sufficiently Li- and La-rich LLTO compositions, microstructure development starts at around 1100 °C with the formation of plate-like grains composed of layered Ruddlesden-Popper (RP)-type $Li_2La_2Ti_3O_{10}$ phase with periodic structure and structurally related non-periodic sequences. These grains undergo exaggerated growth and develop into large plate-like grains with thicknesses of up to 10 µm and lengths over 100 µm. Theoretical calculations confirmed that the formation of RP-type sequences is energetically favored and precedes the formation of the LLTO perovskite phase. Microstructure development continues with the crystallization of LLTO perovskite, epitaxially on the plate-like grains and as individual smaller grains with thinner in-grain RP-type lamellae, resulting in bimodal microstructure.

The structural and compositional characteristics of the lamellae were thoroughly investigated by scanning transmission electron microscopy in combination with image simulations. Periodic sequences of the $Li_2La_2Ti_3O_{10}$ phase consist of pseudo-perovskite blocks separated by a Li-rich layer. Thin in-grain lamellae exhibit a non-periodic structure, with pseudo-perovskite blocks of varying thicknesses. At around 1250 °C, pronounced ion exchange occurs in non-periodic sequences between the Li-rich RP layers and the neighboring Ti and La layers. The degree of ion exchange was estimated by quantitative HAADF-STEM analysis. The thermal instability of the RP-type defects leads to their gradual recrystallization to LLTO.

At higher sintering temperatures (1350 °C), all sequences of RP-type defects completely recrystallize to LLTO. Furthermore, the smaller LLTO grains recrystallize onto the large plate-like seed grains via Ostwald ripening. This process results in the development of dense microstructures with LLTO grains measuring up to 100 µm in diameter. This method represents a novel and straightforward approach for the preparation of coarse-grained LLTO ceramics with total ionic conductivity in the range of 10^{-4} S/cm.

Povzetek

Baterije s trdnim elektrolitom so ena izmed ključnih tehnologij za shranjevanje energije in prehod v podnebno nevtralno družbo v prihodnosti. V primerjavi z baterijami s tekočim elektrolitom so take baterije bolj varne, stabilne in imajo širši temperaturni razpon delovanja. Perovskit $Li_{0.33}La_{0.56}\square_{0.11}TiO_3$ (LLTO) velja za enega najbolj obetavnih trdnih elektrolitov, vendar pa je učinkovitost tega materiala zmanjšana zaradi prisotnosti mej med zrni, ki imajo izrazito nižje vrednosti prevodnosti v primerjavi z zrni. Mikrostruktura LLTO z večjimi zrni bi tako zaradi manjšega prispevka mej imela boljšo ionsko prevodnost.

V sklopu disertacije so bili s konvencionalnim sintranjem v trdnem stanju pripravljeni vzorci LLTO z različnimi začetnimi razmerji La:Ti in presežkom Li. Pri sestavah z zadostnim presežkom Li in La se razvoj mikrostrukture začne pri približno 1100 °C z nastankom podolgovatih zrn, ki so sestavljena iz faze $Li_2La_2Ti_3O_{10}$ tipa Ruddlesden-Popper (RP) s periodično strukturo in strukturno sorodnimi neperiodičnimi zaporedji. Ta zrna izkazujejo pretirano rast in se razvijejo v velika podolgovata zrna z debelino do 10 µm in dolžino preko 100 µm. Teoretični izračuni so potrdili, da je nastanek zaporedij tipa RP energetsko ugodnejši in poteka pred nastankom perovskita LLTO. Razvoj mikrostrukture se nadaljuje s kristalizacijo perovskita LLTO, epitaksialno na podolgovatih zrnih in kot individualna zrna s tanjšimi lamelami tipa RP znotraj zrn, kar vodi v razvoj bimodalne mikrostrukture.

Sestava in struktura lamel tipa RP sta bili raziskani z vrstično presevno elektronsko mikroskopijo v kombinaciji s simulacijami. Periodična zaporedja faze $Li_2La_2Ti_3O_{10}$ so sestavljena iz psevdo-perovskitnih blokov, ločenih z Li-bogato plastjo. Tanjše lamele znotraj LLTO zrn imajo neperiodično strukturo s psevdo-perovskitnimi bloki različne debeline. Pri približno 1250 °C v neperiodičnih zaporedjih pride do ionske izmenjave med Li-plastmi in sosednjimi Ti- in La-plastmi. Stopnja ionske izmenjave je bila ocenjena s kvantitativno analizo HAADF-STEM slik. Defekti tipa RP zaradi toplotne nestabilnosti postopno rekristalizirajo v LLTO.

Pri višjih temperaturah sintranja (1350 °C) vsa zaporedja defektov tipa RP popolnoma rekristalizirajo v LLTO. Poleg tega manjša zrna LLTO rekristalizirajo na velika podolgovata zrna preko Ostwaldovega zorenja. Proces vodi do razvoja goste mikrostrukture z LLTO zrni velikosti do 100 µm. Predstavljena metoda je inovativen način priprave LLTO keramike z velikimi zrni in ionsko prevodnostjo okoli 10^{-4} S/cm.

Contents

List of Figures

List of Tables

Abbreviations

ADF	... Annular Dark Field
APB	... Anti-Phase Boundary
ASSB	... All-Solid-State Battery
BF	... Bright-Field
BSE	... Backscattered Electrons
DFT	... Density Functional Theory
EBSD	... Electron Backscatter Diffraction
EDS	... Energy-Dispersive X-Ray Spectroscopy
EELS	... Electron Energy Loss Spectroscopy
ELNES	... Energy Loss Near Edge Structure
FFT	... Fast Fourier Transform
FTIR	... Fourier Transform Infrared Spectroscopy
HAADF	... High-angle Annular Dark Field
ICP-MS	... Inductively Coupled Plasma Mass Spectrometry
ICP-OES	... Inductively Coupled Plasma Optical Emission Spectroscopy
LA-ICP-MS	... Laser Ablation Inductively Coupled Plasma Mass Spectrometry
LiPON	... Lithium Phosphorus Oxynitride
LISICON	... Li^+ Superionic Conductor
LLTO	... $Li_{3x}La_{2/3-x}\square_{1/3-2x}TiO_3$
ND	... Neutron Diffraction
NMR	... Nuclear Magnetic Resonance
RP	... Ruddlesden-Popper
SALT	... Single-Atom-Layer Trap
SEM	... Scanning Electron Microscopy
STEM	... Scanning Transmission Electron Microscopy
TEM	... Transmission Electron Microscopy
TDS	... Thermal Diffuse Scattering
XRD	... X-Ray Diffraction
XPS	... X-Ray Photoelectron Spectroscopy

Symbols

a	... lattice spacing
d	... spacing between lattice planes
D	... grain diameter
e	... charge of ions
F	... electric field
I	... atomic column intensity
La-C	... La columns inside the pseudo-perovskite block
La-E	... La columns at the edge of the pseudo-perovskite block
n	... number of La-rich layers in pseudo-perovskite block
n	... order of diffraction
n_i	... the number of ions per unit volume
Q	... quenched
r	... atomic radius
R	... the occupancy with La^{3+} ions
S	... order parameter
t	... tolerance factor
Ti-C	... Ti columns inside the pseudo-perovskite block
Ti-E	... Ti columns at the edge of the pseudo-perovskite block
u	... octahedral factor
Z	... average atomic number of the atomic column
□	... vacancy
α-LLTO	... LLTO with pseudocubic modification
β-LLTO	... LLTO with tetragonal modification
θ	... incident angle
λ	... wavelength
μ_i	... mobility of ions
σ	... ionic conductivity
σ_{bulk}	... bulk (grain) ionic conductivity
σ_{gb}	... grain boundary ionic conductivity
σ_{total}	... total ionic conductivity

Chapter 1

Introduction

An increasing global energy demand coupled with apparent consequences and challenges of global warming underscores the urgency of transition to a climate-neutral society that focuses on renewable and clean energy sources, like solar and wind, as well as safe and reliable energy storage [1], [2], [3]. One of the key technologies for future energy storage in mobile, stationary, and other applications, are batteries (Figure 1.1) [4], [5]. Batteries that rely on toxic and unstable organic liquid electrolytes are reaching their limits in terms of optimization potential [6], [7]. Replacement of the flammable and hazardous liquid electrolyte with solid electrolyte therefore represents the new generation of batteries, i.e. all solid-state batteries (ASSBs) [8]. A tremendous research effort has been devoted to enhancing ASSBs' performance, especially capacity, charging rates, cycle life, and long-term stability [9], [10], [11], [12], [13]. The absence of a liquid component improves safety and enables superior energy and power density, making ASSBs particularly attractive for applications where reliability and security are crucial. Furthermore, ASSBs offer increased energy storage capacity with a smaller carbon footprint, thus paving the way for more compact and powerful devices [14], [15].

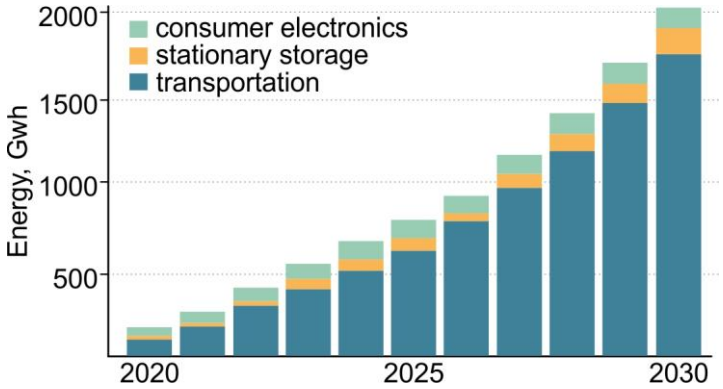

Figure 1.1: Projected annual battery demand by application (adapted by [16]).

As the new generation of batteries is expected to become a key actor in different technological applications, solid-state materials still face limitations that impede their scale-up for commercialization, especially poor electrolyte ionic conductivity and interface compatibility, and slow electrode process kinetics. Overcoming these challenges requires further systematic studies, development of new materials, optimization of synthesis and properties of current solid-state materials, and finally a thorough characterization with advanced techniques. This approach is essential to advance the battery materials and achieve demands for the commercial viability of solid-state batteries.

1.1 All-Solid-State Batteries

Replacement of the conventional liquid electrolyte with a solid electrolyte would resolve most safety drawbacks and enhance battery performance. The intrinsic solid nature of electrolytes in ASSBs enables them to operate reliably across a much wider temperature range between −30 and 100 °C, whereas batteries with liquid electrolytes face a significant performance degradation at low temperatures and deteriorate rapidly at temperatures above 60 °C [17]. Owning to the superior volumetric energy density, meaning they deliver greater battery capacity per unit volume, solid electrolytes are not only more compact but also lighter. This is important for the miniaturization of devices with maintained or improved performance [4], [18], [19]. The structure of an ASSB consists solely of a cathode, anode, and solid electrolyte that are in close interfacial contact, facilitating electrochemical reactions and ensuring mechanical stability which allows for simpler design [13], [20]. The operational principle during charging involves the deintercalation of Li^+ ions from the cathode to the anode through a conductive electrolyte and the transfer of electrons to the anode via an external circuit (Figure 1.2). Contrary to a liquid electrolyte, the solid electrolyte not only conducts the Li^+ during the cycling process but also acts as a separator and binder, preventing electrode contact and potential short circuits within the battery [21], [22].

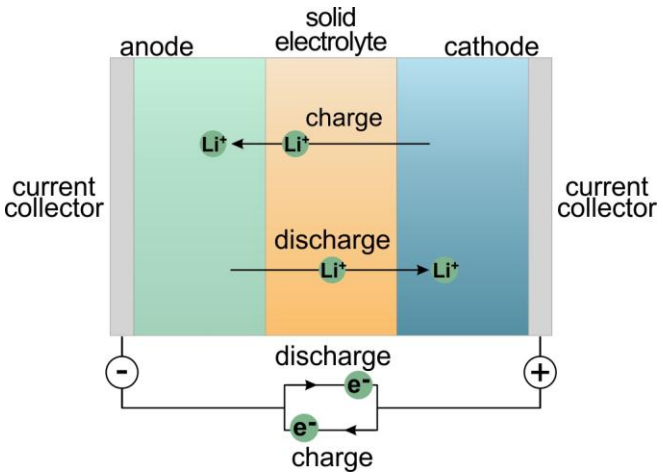

Figure 1.2: ASSB structure and working principle.

Despite the significant advantages of ASSBs, their large-scale production and application still need to overcome technological challenges. Further research is required to reach the solid electrolyte peak performance, especially the ionic conductivity and chemical stability. It is also essential to enhance the interfacial contact of the solid electrolyte with electrodes. Since the solid electrolyte cannot conform to the electrode surface as a liquid electrolyte, poor contact causes increased resistance and decreased performance [23]. The interface can be additionally degraded during cycling as the volume of the electrodes changes and can lead to dendrite formation, which can result in short-circuiting of the battery. Dendrites can grow also in a solid electrolyte due to possible electronic conductivity and the presence of grain boundaries, defects, and voids [24]. To build comprehensive models that predict battery behavior, it is crucial to understand the processes during charge and discharge, like electrode and electrolyte degradation, phase transitions, volume expansion, and formation of unstable solid-electrolyte interphase [2], [14], [25], [26], [27]. The new knowledge and developments are vital for manufacturing high-

quality and scalable materials for ASSBs with improved performance, supporting advancements in electrical vehicles, electronic devices, and various new technologies [9], [28]. Finally, it is also important to address the aspect of availability of raw materials, their cost for scale-up production of sustainable batteries, and the potential of recyclability of battery components [5], [28], [29].

Considering the fact that the performance of ASSBs is directly affected by the electrolyte, the selection of solid electrolyte is of high importance and needs to fulfill several parameters [18], [19], [29], [30]:

- high ionic bulk conductivity and low grain boundary and interfacial resistance,
- negligible electronic transport (transference number $\sigma_{Li}/\sigma_{total}$ close to 1),
- thermal and chemical stability over the operation temperature range,
- sufficient mechanical strength,
- high electrochemical stability window,
- compatibility with electrodes,
- low activation energy,
- environmental friendliness.

Solid electrolytes are categorized into three groups: organic polymer solid electrolytes, organic-inorganic composite solid electrolytes, and solid-state electrolytes (Figure 1.3) [4].

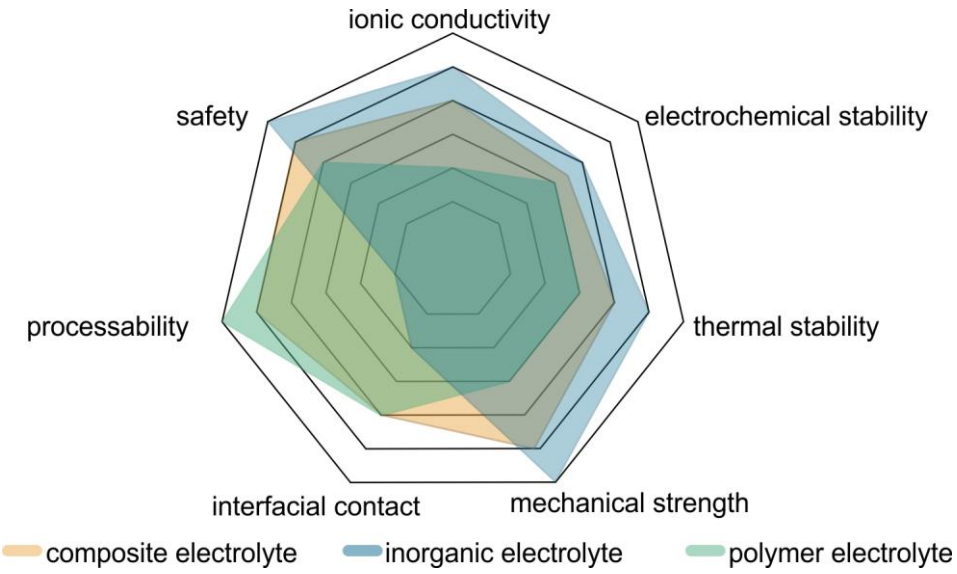

Figure 1.3: Comparison of different types of solid electrolytes (adapted by [31]).

While polymer electrolytes can form high-quality contacts with electrodes due to their flexibility, they have poor mechanical stability and generally low ionic conductivity at room temperature. Organic-inorganic composite electrolytes offer very high ionic conductivities and interface characteristics, but they suffer from safety issues [32], [33]. Solid-state inorganic electrolytes can exhibit high ionic conductivities in the range of 10^{-2} to 10^{-3} S/cm at room temperature, which is comparable to currently used liquid electrolytes. Their advantage lies in good mechanical stability, relatively good chemical stability, and wide operating temperature range [14]. The group of solid-state oxide electrolytes consists of numerous diverse materials and is generally divided into several groups (Figure 1.4).

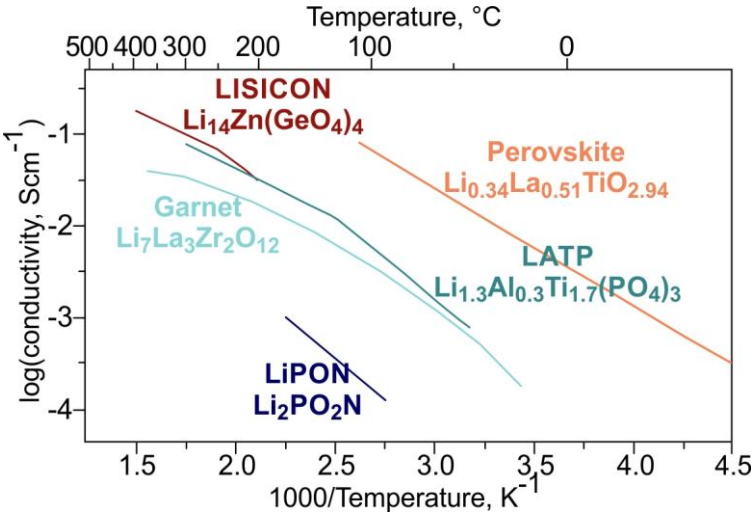

Figure 1.4: Arrhenius plots for ionic conductivities of selected solid inorganic electrolytes (adapted by [26], [34]).

Electrolytes based on titanium phosphates, like $Li_{1.5}Al_{0.3}Ti_{1.7}(PO_4)_3$ (LATP), have a three-dimensional framework structure and exhibit relatively high ionic conductivities, good chemical and mechanical stability, and low production cost [35], [36]. The iconic conductivity can be enhanced by doping and sintering optimization. Their potential is challenged by the presence of a nonconductive secondary phase and poor interfacial performance [36], [37].

LISICON (Li^+ superionic conductor) electrolytes are germanium oxides based on Li_3PO_4 structure. Certain compositions can exhibit high electrochemical stability and a wide electrochemical window [38]. While combining different elements in the structure can significantly improve ionic conductivity, the presence of rare and costly elements, sensitivity to moisture, and low ionic conductivity at room temperature hinder their practical application [11], [39].

Garnet-type electrolytes based on $Li_7La_3Zr_2O_{12}$ have good electrochemical and thermal stability, compatibility with electrodes, and a wide electrochemical window. They crystallize in tetragonal or cubic modification, the latter is stable at higher sintering temperatures. The short migration path of Li^+ in garnet with cubic symmetry yields the highest reported ionic conductivity among solid electrolytes [40]. Disadvantages that impede their application are related to the high costs of rare-earth elements for the production of the material, instability in air at room temperature, and complex synthesis process for high-quality ceramics because of the pyrochlore phase formation [11].

LiPON (lithium phosphorus oxynitride) typically exhibits an amorphous structure and has negligible electronic conductivity and high electrochemical stability. Owing to its easy growth in the form of thin films with sputtering techniques, it is considered for applications as a solid electrolyte in thin film micro batteries [18], [41]. Relatively low ionic conductivity and costly fabrication process impede its commercial viability.

Perovskites represent a wide group of compounds with the general formula ABO_3. Due to their high ionic radii tolerance, they are characterized by high structural and compositional flexibility, which enables tailoring of their functional properties, making them a promising candidate for solid electrolytes [42]. Lithium lanthanum titanate (LLTO), with the general formula $Li_{3x}La_{2/3-x}\square_{1/3-2x}TiO_3$ has attracted much interest due to its high ionic conductivity at room temperature [43]. This compound is chemically and thermally stable in the air and is also environmentally friendly as it does not decompose to toxic products. Moreover, it has a wide electrochemical window, enabling operation over a broad

range of voltages [33]. The highest ionic conductivity of LLTO in the order of 10^{-3} S/cm at room temperature was measured in composition with x=0.11 ($Li_{0.33}La_{0.56}\square_{0.11}TiO_3$), where the presence of many vacancies in the A-sites enables fast migration of Li through the lattice [44]. While the bulk conductivity of LLTO is one of the highest among Li-ion-conducting oxides and is sufficiently high for all-solid-state battery applications, the total conductivity is reduced by grain boundaries for several orders of magnitude [45], [46], [47]. The development of a solid electrolyte based on LLTO ceramics and the characterization of its structural and chemical properties will be the main topic of this doctoral dissertation.

1.2 $Li_{3x}La_{2/3-x}TiO_3$ Perovskite

$Li_{3x}La_{2/3-x}\square_{1/3-2x}TiO_3$ (LLTO) with perovskite-type structure is one of the promising candidates for solid electrolytes as it exhibits high ionic bulk conductivity compared to other electrolytes, has high thermal stability, and high transference number (between 0.5 and 0.9) [32], [33]. The activation energy for conduction is below 0.4 eV [44]. Its superior ionic conductivity was first reported by Inaguma et al. in 1993 [44] and Kawai et al. in 1994 [48]. Since then, extensive research effort has been invested into the study of this material for application as a solid electrolyte.

1.2.1 Perovskite-type structure

LLTO belongs to a wide group of materials with a perovskite-type structure, characterized by structural and compositional versatility and excellent stability [49]. Perovskites occur as natural minerals and much more common as functional materials. The flexibility of the perovskite structure facilitates various substitutions and nonstoichiometry on both, cationic and anionic sites [49], [50], [51]. This can be used for modification of physical properties and enables correlations between composition, structure, and properties. Perovskite oxides, therefore, exhibit interesting functional properties like dielectric, conductive, catalytic, optical, photocatalytic, and magnetic properties, and are intensively studied as materials for wide-range technological applications in electronics, photovoltaics, and fuel cells [50], [52], [53].

The general formula of single oxide perovskites is ABO_3. The aristotype perovskite structure with the body-centered cubic arrangement of atoms (space group *Pm3m*) can be found in mineral tausonite $SrTiO_3$ at room temperature and ambient pressure conditions (a=0.3905 nm). In cubic structure, the larger A-site cations (Sr in $SrTiO_3$) occupy central positions (positions ½,½,½) of the cubic close-packed sublattice and are coordinated with 12 oxygen atoms (dodecahedral coordination). The smaller B-site cations (Ti in $SrTiO_3$) are typically transition metals and occupy cube corner positions 0,0,0. They are octahedrally coordinated by oxygen anions (on positions ½,0,0; 0,½,0 and 0,0,½), forming an infinite 3D framework of corner-shared BO_6 (TiO_6 in $SrTiO_3$) octahedra [54]. The A-O bonds exhibit ionic character, while the bonds between B-site cations and O anions in the octahedra have predominantly covalent character [55].

In the ideal cubic perovskite structure, the ratio between A-O bond and A-B bond lengths is equal to √2, and the size ratio between cations corresponds to the Goldschmidt tolerance factor 1. Goldschmidt factor applies ionic radii at room temperature to estimate the possibility for the formation of a stable perovskite structure and is defined as

$$t = \frac{r_A + r_O}{\sqrt{2}(r_B + r_O)} \quad \text{(Eq. 1)},$$

where r_A, r_B, and r_O are effective ionic radii of the A, B, and O ions, respectively. A stable perovskite structure has t value between 0.75 and 1. Another factor indicating the stability of the perovskite structure is the octahedral factor u, defined as

$$u = \frac{r_B}{r_O} \quad \text{(Eq. 2)}.$$

The tolerance factor t can be used as a measure of the degree of distortion from the ideal structure. The distortion occurs to minimize the strain due to the different ion sizes and results in a reduction of symmetry (tetragonal, trigonal, orthorhombic) [56]. Perovskites with a tolerance factor different from 1 exhibit more complex structures, with displacements of B-site cations, tilts and rotation of the octahedra, and distortions of the octahedra (Figure 1.5) [50], [57].

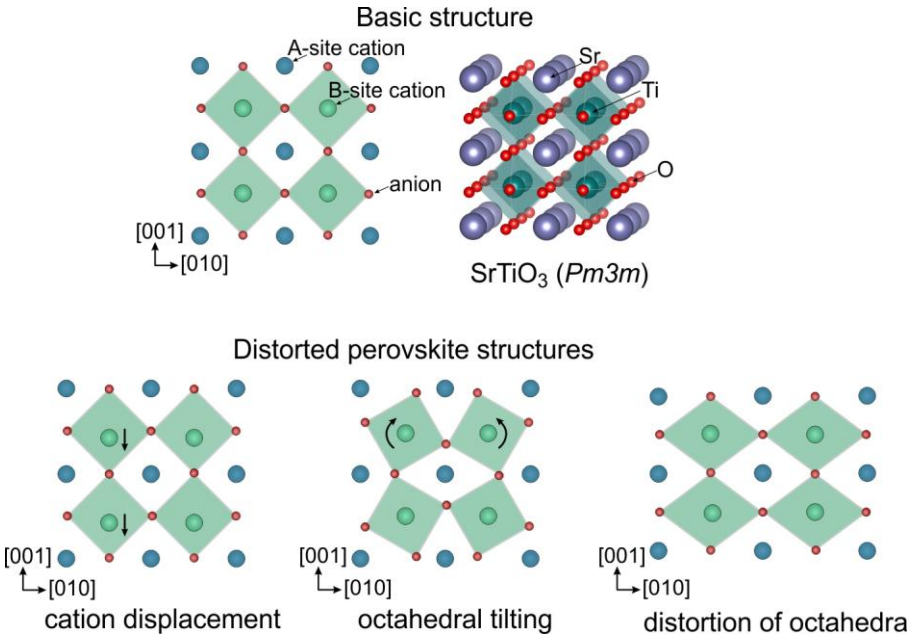

Figure 1.5: Structural variability in single ABO_3 perovskites.

Cation displacement from the centrosymmetric position is typical when the tolerance factor is larger than 1. Cation displacements in BO_6 octahedra occur along one of the symmetry axes of the octahedra to lower ground-state energy. It causes the formation of tetragonal, trigonal, and orthorhombic symmetries, depending on the direction and magnitude of displacements [50], [58], [59]. A cation can move along three tetrad axes passing octahedron vertices, four triad axes passing through centers of the opposing faces, or six diad axes passing through centers of the edges. Displacement of cations is temperature and pressure-dependent and has a large impact on the material's dielectric properties as it induces electrical polarity [50], [54]. For example, $PbTiO_3$ is a ferroelectric with a tetragonal structure at ambient temperature and pressure due to displacement of the cation in the octahedra and a paraelectric with cubic structure above Curie temperature at 489.9 °C [60].

Octahedral tilting occurs when the tolerance factor t smaller than 1. Tilting is usually associated with the presence of the A-site ions that are too small for the cuboctahedral cage, leading to tilting and rotation of the octahedra with 15 different crystallographic variants [50], [54], [55]. These distortions lower the symmetry of the perovskite and are temperature, pressure, and strain-sensitive [50]. For example, $CaTiO_3$ has an orthorhombic

structure at room temperature but with increasing temperature transforms to tetragonal and further to cubic symmetry [61]. Glazer (1972) proposed a notation to describe tilting by rotation along the x, y, and z axes along the three tetrad axes of the basic building octahedron ([100], [010], and [001] axes) using symbols of the type $a^{\#}b^{\#}c^{\#}$ [62], [63]. The positive (+) symbol denotes in-phase tilt (tilts of successive layers in the same directions), whereas the negative (–) symbol is for anti-phase tilts (tilts in opposite directions in two successive layers). The notation for the ideal cubic structure is $a^0a^0a^0$, which implies that there is no tilt along any of the axes [62].

Derivative compounds of the basic single ABO_3 perovskites are double perovskites $AA'B_2O_6$, where A-sites are partially substituted by different cations, and layered perovskites [57], [64], [65]. The strain energy due to the different sizes of cations on A-sites in double perovskites can be reduced by ordering, which can be random, rock salt, or alternating (Figure 1.6). When the overall valence of A- and B-sites is less than six, the missing charge is compensated by nonstoichiometry on anionic sites. The missing charge introduces (ordered) vacancies on the oxygen lattice [59]. The common characteristic of nonstoichiometric and layered perovskites are exchanging blocks of perovskite-like or pseudo-perovskite units (blocks) and layers with a different atomic arrangement, like rock salt layers in Ruddlesden-Popper phases [57], [66].

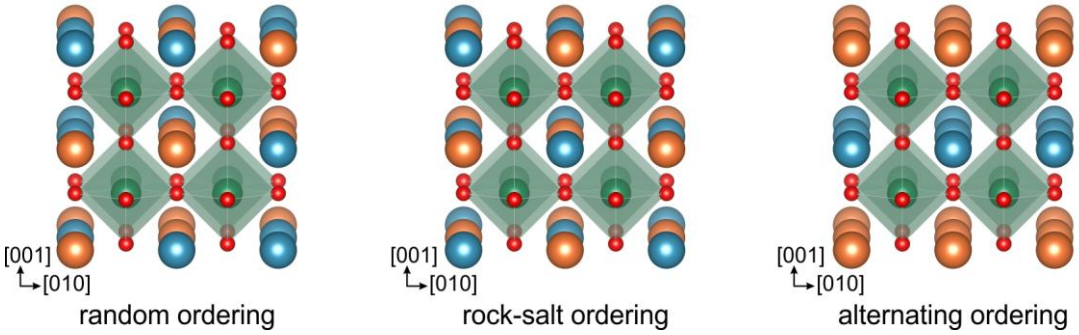

Figure 1.6: Types of ordering in double $AA'B_2O_6$ perovskites.

1.2.2 Layered perovskites

Generally, layered 2D perovskites have a modulated structure that can accommodate larger deviations from the basic ABO_3 stoichiometry. They consist of parent pseudo-perovskite blocks with ABO_3 structure and alternating interlayers. The compositional change is accommodated by changing the thickness of the pseudo-perovskite blocks or in the interlayers. These interlayers can facilitate ion transport and therefore exhibit reactions of ion exchange and intercalation [67], [68], [69]. Ordering of modulated structures results in the formation of homologous series [50], [70]. The three main groups of layered perovskites are Dion-Jacobson, Bi-containing Aurivillius phases, and Ruddlesden-Popper phases (Figure 1.7).

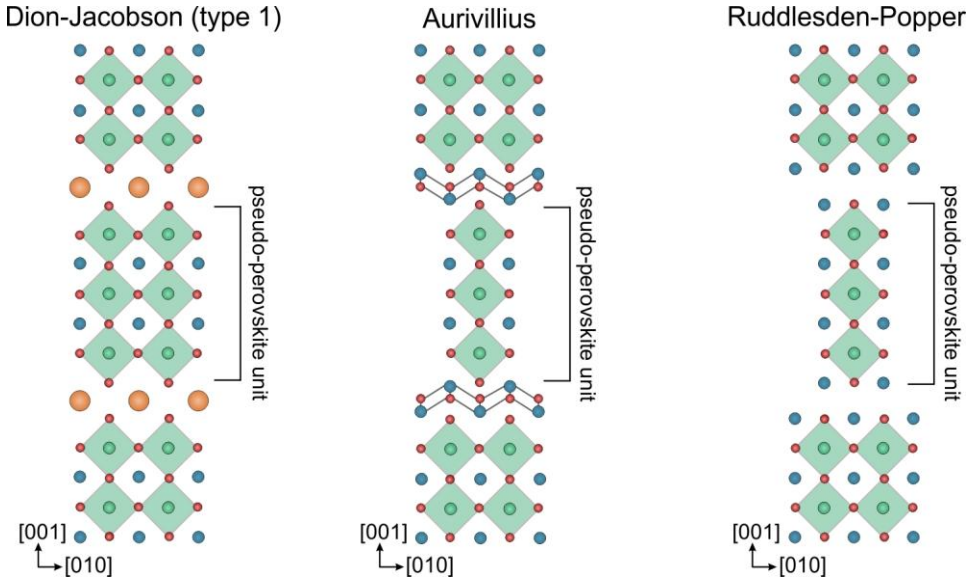

Figure 1.7: Schematic structures of the layered perovskite phases.

1.2.3 Ruddlesden-Popper phases

Ruddlesden-Popper (RP) phases have a general formula $A_{n+1}B_nO_{3n+1}$, where pseudo-perovskite blocks with n-layers are intercalated with AO layers adopting rock-salt structure [71]. The crystal structure of RP phases can also be described as a sequence of perovskite blocks in the [001] direction with a thickness of n octahedra, where each block is shifted relative to another for half of the unit cell in the [010] direction [50]. Such structures, where layers with almost identical structure and composition are arranged in a certain periodic stacking sequence, are typical for polysomes [72]. A-sites are commonly occupied by alkali earth elements and B-sites by tetravalent transition elements. Alternatively, A-sites can be occupied by rare earth elements, with a divalent state transition metal on the B-sites [73], [74]. A typical example of a RP-type phase is $Sr_{n+1}Ti_nO_{3n+1}$, where compounds with n=1, 2, and 3 can be prepared by traditional ceramic techniques [75].

Figure 1.8 presents structures of RP phases with n=1, 2, and 3 and an ideal tetragonal unit cell (space group *I4/mmm*), alongside the structure of a single perovskite for comparison. The structure of the first member A_2BO_4 adopts the K_2NiF_4 type 2D structure, where the corner-shared octahedra are connected only in one plane, forming an infinite ABO_3 layer in ab direction [64], [73]. The structure therefore consists of alternating pseudo-perovskite layers with a thickness of one unit cell and layers of AO with rock-salt structure in [001] direction [76]. Anisotropic features in the structure of RP phases with n=1 allow high variability in oxygen stoichiometry in comparison with ABO_3 perovskites. Due to higher oxygen diffusion, A_2BO_4 oxides can contain excess oxygen, where oxygen interstitial atoms are located inside the AO layer, or can be oxygen-deficient with oxygen vacancies in the perovskite layer. Oxygen defects can form due to doping or substitution of an A^{2+} with a cation of higher valence state (for example substitution of Sr^{2+} with La^{3+} in Sr_2TiO_4). The overall charge may be balanced by B-site transition metal with a mixed valence state [77], [78].

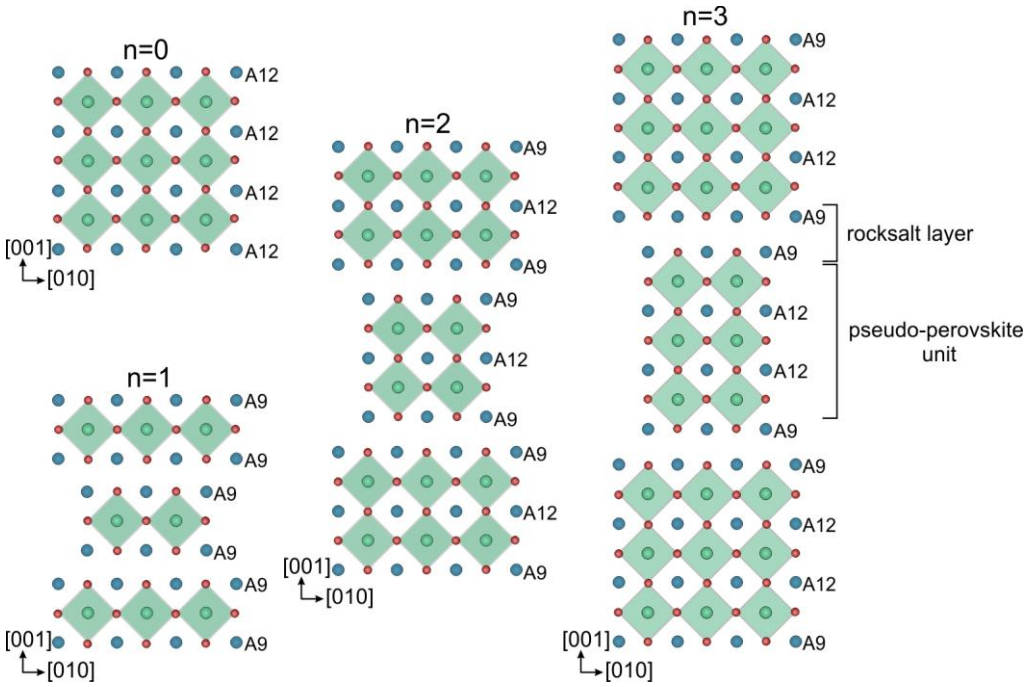

Figure 1.8: Crystal structure of single perovskite ABO_3 (n=0) and members of the $A_{n+1}B_nO_{3n+1}$ RP family with n=1, 2, and 3. The denotation of n represents the number of stacked perovskite-type layers separated by the rock salt-type A-O layer.

Members of the RP family with n=2 ($A_3B_2O_7$) and n=3 ($A_4B_3O_{10}$) contain two or three ABO_3 perovskite layers along the c-axis between the AO rock-salt layers, respectively. The coordination number of A-site cations in these members depends on their position; cations inside the pseudo-perovskite block have 12-fold coordination (denoted as A12 in Figure 1.8), while the coordination number of cations in the rock-salt layer is 9 (denoted as A9 in Figure 1.8). Two different crystallographic positions in n>1 allow the accommodation of different cations on A-site positions. Additionally, with a higher number of layers in pseudo-perovskite blocks, the number of anionic positions increases, leading to the formation of structures with greater compositional variation [78].

Due to the layered nature of RP phases and the presence of local nonstoichiometry in the rock-salt interlayer, they exhibit a wide variety of physical and chemical properties that cannot be obtained in compounds with a simple perovskite structure [79]. RP phases can form structural 2D defects inside perovskite matrix grains or thin films and can have a significant influence on the microstructure development and physical properties of the ceramics. In bulk ceramics, they form due to nonstoichiometry of the starting composition or the addition of specific dopants. In thin films, the formation of RP planar defects stems not only from nonstoichiometry of the initial composition [80] but is also a result of strain relaxation due to the substrate's surface steps [81] or lattice mismatch between epitaxial multilayer thin films [82] or between thin film and substrate [83].

1.2.4 Phase relations in the La_2O_3-TiO_2-Li_2O system

LLTO phases may be positioned into the ternary Li_2O-La_2O_3-TiO_2 phase diagram, which includes several binary and ternary oxides (Figure 1.9). Binary oxides comprise of lithium titanate phases Li_2TiO_3, $Li_4Ti_5O_{12}$ with spinel structure, and ramsdellite-type $Li_2Ti_3O_7$, all showing suitable properties for potential applications as anode materials [84], [85], [86]. On the other hand, lanthanum titanates consist of various phases such as La_2TiO_5, perovskite-

related layered $La_2Ti_2O_7$, and perovskite $La_{2/3}\square_{1/3}TiO_{3-\delta}$. The latter is an oxygen-deficient perovskite with 2/3 of A-sites occupied by La^{3+}, while one-third is vacant to obtain charge neutrality. $La_{2/3}\square_{1/3}TiO_{3-\delta}$ is unstable unless sintered in a protective (oxygen deficient) atmosphere or doped with at least a small amount of e.g. Li^+ or Al^{3+} [87], [88], [89], [90]. It is also the end-member of ternary perovskite oxides with the general formula $Li_{3x}La_{2/3-x}\square_{1/3-2x}TiO_3$ (LLTO) with x=0 (La:Ti=0.67) and the highest possible La occupancy. In the LLTO family of compounds, A-sites are occupied by Li^+ and La^{3+}, while some sites remain vacant (denoted by □). With a higher x-value, the amount of La decreases, whereas the amount of Li increases due to the substitution of one La^{3+} with three Li^+ ions for charge preservation. Simultaneously, the content of vacancies also decreases as two out of three Li^+ ions occupy sites of previous vacancies [32]. Finally, in LLTO with x=0.16 ($Li_{0.5}La_{0.5}TiO_3$, La:Ti=0.5), all A-sites are fully occupied with equal amounts of Li and La [91]. Another ternary oxide compound within the Li_2O-La_2O_3-TiO_2 phase diagram is the $Li_2La_2Ti_3O_{10}$ with La:Ti=0.67. It has a layered Ruddlesden-Popper-type perovskite structure, composed of $(La_2Ti_3O_{10})^{2-}$ pseudo-perovskite blocks shifted for 1/2 of the unit cell along the [001] direction and separated by an interlayer of four-fold coordinated Li^+ ions [92], [93].

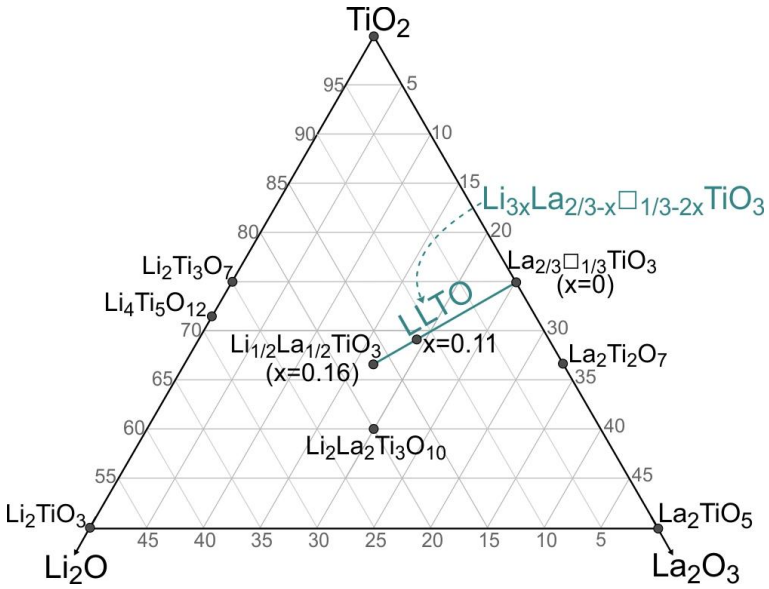

Figure 1.9: Phase diagram based on Li_2O-La_2O_3-TiO_2. LLTO compounds lie between end-members $La_{2/3}\square_{1/3}TiO_3$ and $Li_{1/2}La_{1/2}TiO_3$.

1.2.5 Structural characteristics of the perovskite-type (Li, La)-titanates

Perovskite-type (Li, La)-titanates that occur in the La_2O_3-TiO_2-Li_2O system are the $Li_{3x}La_{2/3-x}\square_{1/3-2x}TiO_3$ (LLTO) perovskites and the layered RP-type $Li_2La_2Ti_3O_{10}$ phase.

LLTO crystallizes in different symmetries, depending on the composition (ratio between Li, La, and vacancies) and synthesis conditions. At low x-values (0.03 to 0.08) LLTO has orthorhombic (space group *Pmmm* or *Cmmm*) or rhombohedral (space group *R-3c*) structure, mostly depending on the cooling rate from the sintering temperature [94], [95], [96]. These structures are slightly distorted due to a high fraction of A-site vacancies, which causes octahedral tilting. In an orthorhombic structure with space group *Cmmm*, the La^{3+} and Li^+ ions are arranged in off-centered positions at the A-sites (Figure 1.10a) [95], [97], [98].

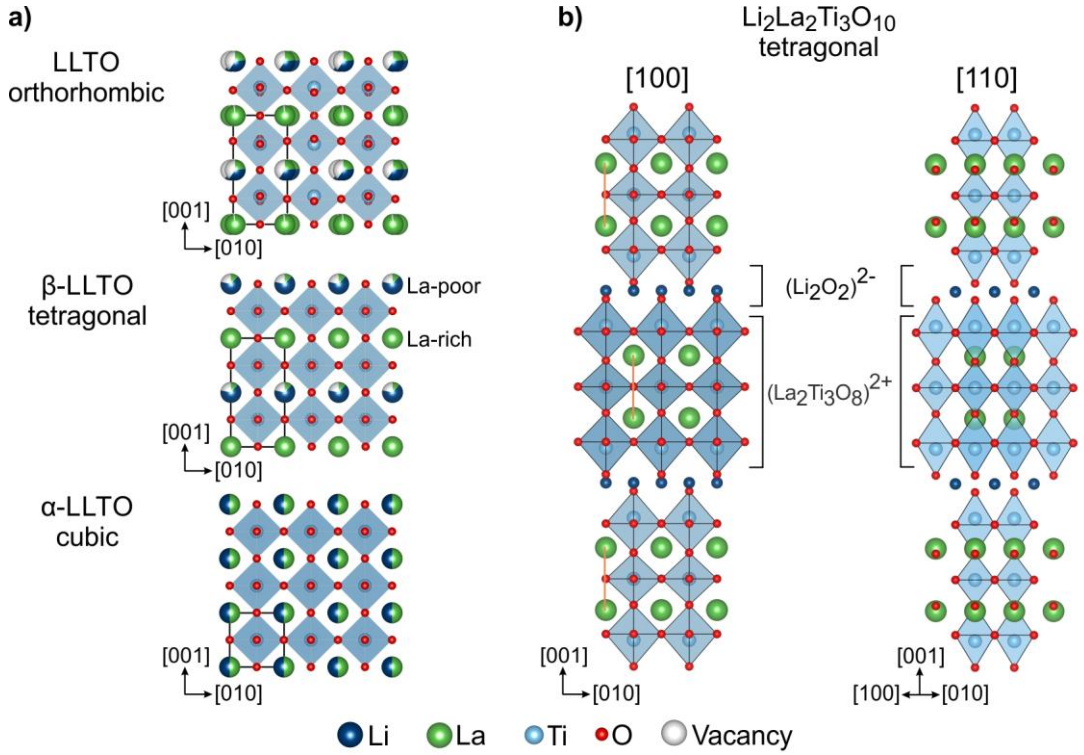

Figure 1.10: (a) Structure of LLTO depending on composition. (b) Structure of $Li_2La_2Ti_3O_{10}$ in [100] and [110] zone axis.

With an increasing x-value, A-sites are gradually more occupied. Compounds with x between 0.08 and 0.16 crystallize in different polymorphic modifications, depending on the excess of Li and synthesis conditions [94], [99], [100], [101], [102], [103]. The polymorphic modifications of LLTO slightly deviate from the ideal perovskite cubic cell [104] and the most reliable technique to distinguish between them is neutron diffraction (ND) [99], [101]. The main difference between the polymorphic modifications is the degree of ordering of the A-site species (Li^+, La^{3+}, vacancies). β-LLTO has tetragonal symmetry (space group *P4/mmm*) and is typically stabilized during slow cooling. It is composed of alternating La-rich and La-poor layers along the c-axis. In the La-rich layers, La^{3+} ions are predominant, while the La-poor layers contain mostly Li^+ and vacancies [48], [105], [106]. Ordering of perovskite structure results in the doubling of the unit cell along the c-axis ($c=2a_{pc}$) [44]. In diffraction experiments, compounds with this type of superstructure ordering yield additional reflections at d-values equal to twice the edge of the pseudocubic cell {h,k,l/2} [44], [48], [89]. An increase in Li^+ concentration (x-value) and/or quenching from high sintering temperatures cause Li^+, La^{3+}, and vacancies to be gradually more disordered, forming pseudocubic symmetry (α-LLTO) [104], [106], [107], [108]. In LLTO with x=0.16 (La:Ti=0.5), no vacancies are present in the structure and the A-sites are fully occupied by equal amounts of randomly arranged Li and La ions.

The order parameter in LLTO [108] is defined as

$$S = (R_{La\text{-}rich} - R_{dis})/(1 - R_{dis}) \qquad \text{(Eq. 3)},$$

where $R_{La\text{-}rich}$ is the occupancy with La^{3+} ions on A-sites in the La-rich layer of ordered β-LLTO and R_{dis} is the occupancy with La^{3+} ions in the (001) plane of disordered α-LLTO. It can be also estimated based on the intensity ratio between the (001) and (110) peaks

from the XRD pattern [105]. The transition from ordered to disordered structure is reversible when LLTO ceramic is subjected to quenching and annealing [105], [108].

Another ternary oxide in the Li_2O-La_2O_3-TiO_2 phase diagram is $Li_2La_2Ti_3O_{10}$, which belongs to the family of RP-type layered perovskites. It is composed of $(La_2Ti_3O_8)^{2+}$ pseudo-perovskite blocks shifted for 1/2 of the unit cell along the [001] direction (marked with orange lines in Figure 1.10b), whereas along the [110] zone axis, the shift is not observed. Unlike RP phases, where pseudo-perovskite blocks alternate with rock-salt layers, pseudo-perovskite blocks in $Li_2La_2Ti_3O_{10}$ are separated by $(Li_2O_2)^{2-}$ layers, in which the Li^+ ions are four-fold coordinated [92], [93]. The $(Li_2O_2)^{2-}$ layer resembles the $(Bi_2O_2)^{2+}$ interlayer in the Aurivillius phase $Bi_2O_2(Bi_2Ti_3O_{10})$. $Li_2La_2Ti_3O_{10}$ has a tetragonal structure with space group *I4/mmm* [92], [109].

Since the $Li_2La_2Ti_3O_{10}$ phase is composed of subsequent pseudo-perovskite blocks, there is a close structural relationship between the LLTO perovskites and the $Li_2La_2Ti_3O_{10}$ phase. The unit-cell parameters of different LLTO modifications exhibit an excellent fit with $Li_2La_2Ti_3O_{10}$ in the [100] direction [92], [102]. The misfit between the two phases is calculated according to the equation

$$\text{misfit} = \left|\frac{(a_1 - a_2)}{a_1}\right| * 100\% \qquad \text{(Eq. 4)},$$

where a_1 and a_2 are parallel distances of the two phases. The misfit between different LLTO modifications and $Li_2La_2Ti_3O_{10}$ in the [100] direction is below 1% (Table 1.1).

Table 1.1: Comparison of structural parameters of different LLTO modifications with $Li_2La_2Ti_3O_{10}$.

$\mathbf{Li_2La_2Ti_3O_{10}}$	$\mathbf{Li_{3x}La_{2/3-x}\square_{1/3-2x}TiO_3}$		
	x=0.063	**x=0.104**	**x=0.167**
Tetragonal (*I4/mmm*)	Orthorhombic (*Pmmm*)	Tetragonal (*P4/mmm*)	Cubic (*Pm3m*)
a=3.841 Å	a=3.865 Å misfit=0.62%	a=3.873 Å misfit=0.83%	a=3.870 Å misfit=0.76%

The structural similarity between phases and a good fit of the lattice parameters are prerequisites for the formation of oriented intergrowths, as well as for epitaxial contacts in thin films.

1.3 Lithium-Ion Conductivity in (Li, La)-Titanates

1.3.1 Conductivity in ceramic lithium electrolytes

In inorganic electrolytes, charge-carrier Li^+ ions act as mobile point species in the immobile framework [110]. Under the influence of an electric field F, Li^+ ions can move through the lattice by hopping to the vacancies, generating new vacancies at the original positions, or as interstitials by directly hopping or interstitial knock-off mechanism [11], [110]. Ionic conductivity can be expressed as

$$\sigma = n_i \, e \, \mu_i \qquad \text{(Eq. 5)},$$

where n_i is the number of ions per unit volume, e is the charge of ions and μ_i is their mobility. Ions should have sufficient energy to pass an energy barrier E_a and to exchange the site with a vacancy.

1.3.2 Bulk conductivity in LLTO

In LLTO, Li^+ ions act as the charge carriers, while La^{3+} ions stabilize the structure of the perovskite [91]. Li^+ ion transport follows the vacancy hopping mechanism, where Li^+ ions migrate through the lattice to adjacent vacancies through the bottleneck window formed by four neighboring oxygen ions that occupy corners of the TiO_6 octahedra (Figure 1.11) [48], [111]. As a result of Coulomb repulsion between Li^+ and La^{3+} ions, percolative channels in the lattice form for ionic conduction [97], where Li^+ ions follow diffusion pathways along the edges of the TiO_6 octahedra [112].

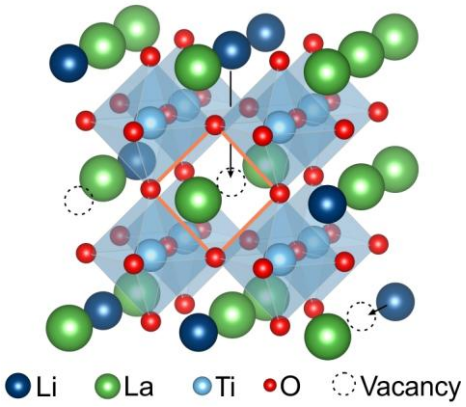

Figure 1.11: In LLTO, the Li^+ ions are transferred to the neighboring vacancies through a bottleneck formed by four oxygen ions.

The ionic conductivity in system $Li_{3x}La_{2/3-x}\square_{1/3-2x}TiO_3$ is proportional to the fraction of Li (3x) and mobility μ of Li^+, which depends on the number of vacancies (1/3–2x) [113], therefore

$$\sigma \propto 3x \cdot (1/3–2x) \qquad \text{(Eq. 6)}.$$

The conductivity of LLTO is a function of x-value with a maximum at around x=0.11 at room temperature (Figure 1.12) [48], [111]. In this LLTO composition, *i.e.* $Li_{0.33}La_{0.56}\square_{0.11}TiO_3$ (La:Ti=0.56), with disordered pseudocubic structure (α-LLTO), the ionic conductivity is in the range of 10^{-3} S/cm [111], [114]. In compositions with x higher than 0.11, the lower amount of vacancies consequently decreases the conductivity [97].

Optimal Li concentration or the concentration of the charge carriers that is necessary for high ionic conductivity [32] can be achieved by the addition of excess Li to the starting composition and/or covering the sample with sacrificial powder during sintering as it suppresses the loss of lithium [115].

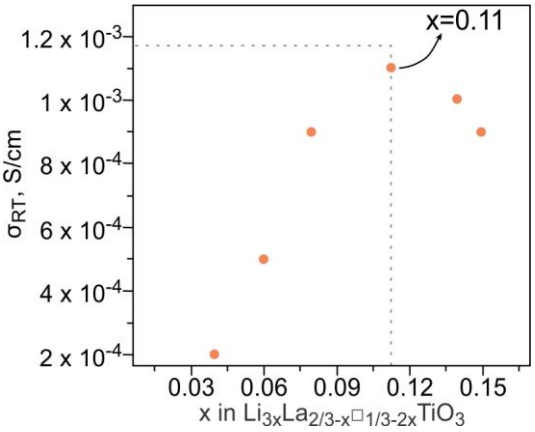

Figure 1.12: Ionic conductivity of LLTO at room temperature as a function of lithium content (x-value) (adapted by [48]).

The highest ionic conductivity is observed in a disordered cubic structure (α-LLTO), which is attributed to the isotropic 3D mobility of Li^+ in the lattice as the Li^+, La^{3+}, and vacancies are randomly distributed in the structure (Figure 1.13a) [114], [116], [117]. The disordered structure also has a lower activation energy for ionic conduction due to a slightly larger a-axis in comparison to the ordered β-LLTO [105], [108], [118], [119]. In ordered tetragonal β-LLTO (Figure 1.13b), migration of Li^+ is anisotropic because the transport is restricted to the La-poor layers (2D), where vacancies are predominant. Due to a low number of unoccupied sites in La-rich layers, the diffusion of Li^+ in these layers is limited [108], [120].

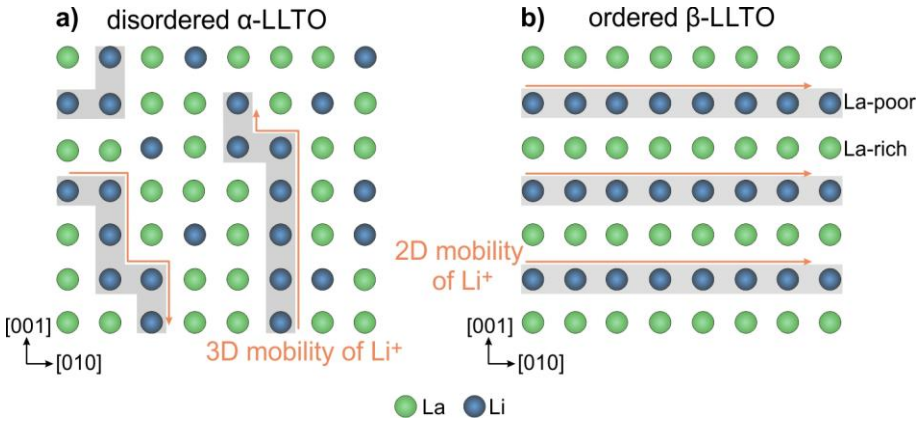

Figure 1.13: Mobility of Li^+ ions in (a) disordered and (b) ordered LLTO structure.

The bulk ionic conductivity in LLTO is primarily determined by the composition (the La/Li ratio) and the crystal structure (the degree of cation ordering). Additionally, the bulk conductivity depends on the size of the so-called bottleneck [12], [97], [121], [122].

Increasing the size of the bottleneck lowers the activation energy for the migration of Li^+ and enhances the ionic conductivity. The size of the oxygen bottleneck can be altered by octahedral tilting and/or changes in lattice parameters [97]. In single-crystal LLTO thin films, the conductivity can be controlled by epitaxial strain and size of the bottlenecks that stem from different in-plane lattice constants of substrates [123]. In polycrystalline ceramics, the bottleneck size increases with the dilatation of the A-site space (lattice parameter), which can be achieved by the substitution of La^{3+} with ions with larger radii.

Larger pathways through tilted and rotated TiO_6 octahedra facilitate ion mobility and thus increase ionic conductivity [114]. For example, improved conductivity was found for Sr-doped LLTO [114], [124], [125], [126], [127], not only because of a larger crystal lattice but also due to an increased number of charge carriers to satisfy the electroneutrality condition on A-sites [124]. Similar was observed for doping of LLTO with a small amount of Ba^{2+}, however, a continuing increase in doping concentration causes the formation of impurity $BaLa_2Ti_4O_{12}$ phase and local lattice deformations that result in inferior values of ionic conductivity [111], [128]. On the other hand, the substitution of La with smaller ions like Ca, Pr, Nd, or Sm does not significantly contribute to the enhancement of ionic conductivity. It generally leads to orthorhombic distortion and contraction of the bottleneck [129], [130]. The substitution of Ti in the octahedra with trivalent cations like Al improves the conductivity, while substitution with tetravalent atoms, such as Zr, Sn, Mn, and Gr, reduces it. This phenomenon suggests that the interatomic bond distances (the A-O and B-O bond distances), and also the bond strengths have a large influence on the electrostatic potential and Li^+ ion mobility in bulk LLTO [125], [131], [132], [133].

While LLTO shows high bulk ionic conductivity, the structurally related RP-type $Li_2La_2Ti_3O_{10}$ phase has low ionic conductivity, as all available 12-fold coordinated interstices inside the La-O layers are occupied with La atoms (100% occupancy). Since there are no vacancies in the Li-interlayer, $Li_2La_2Ti_3O_{10}$ shows no measurable ionic conductivity at room temperature. Ionic mobility in this phase could be induced by Li deficiency, resulting in vacancies in the Li-rich layer, or by La deficiency to promote Li transport in the [001] direction [109].

1.3.3 Total ionic conductivity of LLTO

The total ionic conductivity of polycrystalline LLTO-based ceramics is primarily determined by a combination of two main contributions, the conductivity of the grains or bulk conductivity and the conductivity of the grain boundaries. These contributions can be distinguished using impedance spectroscopy, where each contribution typically appears as a distinct semicircle in the Nyquist plot.

While the bulk ionic conductivity of LLTO, ranging from 10^{-3} to 10^{-4} S/cm, is already suitable for practical applications, the grain boundary conductivity is significantly lower, by several orders of magnitude. This disparity in conductivity between the bulk and grain boundaries is one of the main challenges in optimizing LLTO ceramics for use in solid-state electrolytes.

In addition to grain boundaries, other non-periodic features further reduce the total ionic conductivity of LLTO ceramics. These include domain boundaries, planar defects, secondary phases, and pores, all of which interrupt the Li^+ conduction pathways (Figure 1.14) [46], [134], [135], [136], [137]. The collective effect of various factors can significantly limit the performance of LLTO.

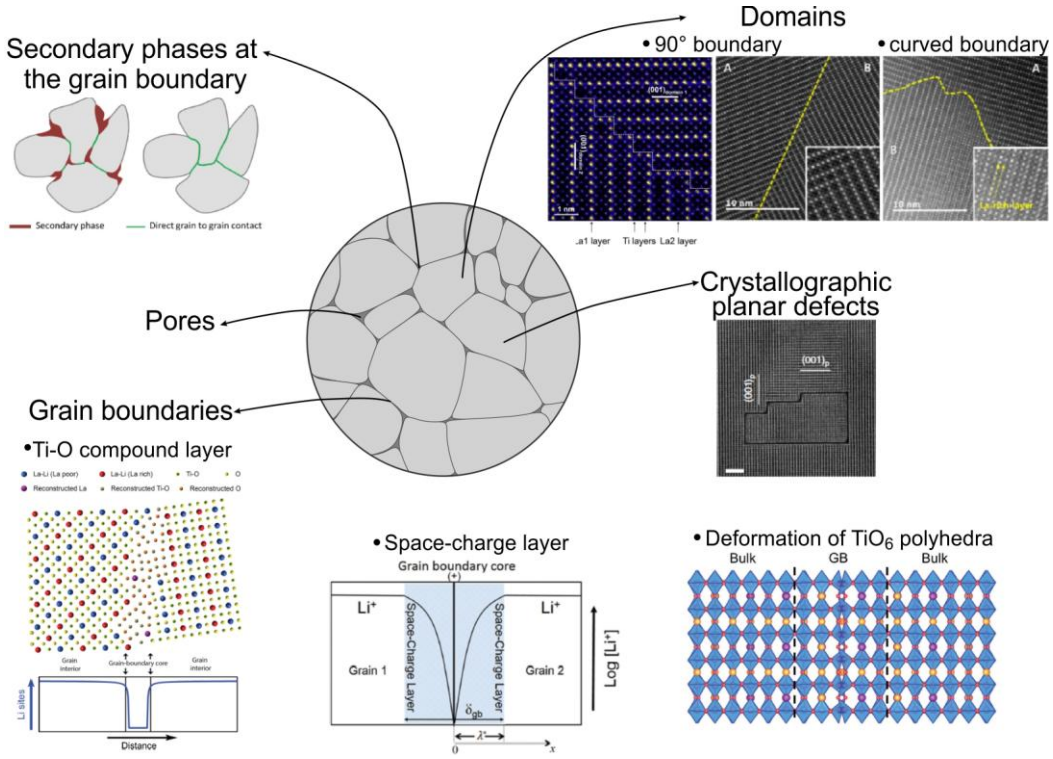

Figure 1.14: Factors that lower the total ionic conductivity of LLTO. They include secondary phases [45], pores, grain boundaries [46], [138], [139], crystallographic planar defects [136], and domain boundaries [135], [140].

Optimizing the ionic conductivity of LLTO is challenging due to the contradictory effect of synthesis requirements, for example, using high temperatures and dwell time during sintering promotes the formation of coarse grains, however, LLTO under such conditions tends to have a tetragonal structure and is prone to Li loss through evaporation.

1.3.3.1 Effect of domain boundaries

During cooling from high sintering temperatures, cubic LLTO transforms to tetragonal LLTO with an ordered structure. During the recrystallization, tetragonal domains develop along three equivalent [100] pseudocubic directions, with neighboring domains typically meeting at 90 ° domain boundaries [141]. The size of domains ranges from a few nanometers up to a few tens of nanometers, depending on Li^+ concentration [103], [134]. Intrinsic domain boundaries represent a limitation for Li^+ migration as a result of lattice mismatch; the ions transferred in La-poor layers of one domain are blocked by La-rich layers in another domain, where very high activation energy in La-rich layers (by order of magnitude) limits the diffusion of Li^+ ions [140]. Domain size, density and structure of domains, and shape of domain boundary depend on the sintering temperature, Li concentration, and cooling rate (x-value in LLTO) [120], [134]. Cooling of LLTO from high sintering temperatures (1400 °C) results in larger domains separated with straight boundaries [135]. Smaller domains that form during cooling from sintering temperatures below 1250 °C [96] usually have curved boundaries and low Li^+ conductivity [135].

1.3.3.2 Effect of crystallographic planar defects

Crystallographic planar defects are 2D interruptions of the otherwise perfectly periodic crystal structure and include stacking faults, anti-phase boundaries, and planar defects

with a locally different composition. Although these features are usually localized they can significantly influence the ionic transport, chemical, structural, and mechanical properties [142], as well as the microstructure development of the ceramics. Controlling the type, density, and distribution of planar defects is important for tailoring the properties of ceramic materials for specific applications.

Antiphase boundaries have been found in LLTO with composition x=0.11 prepared with a sol-gel process [142]. Antiphase boundaries develop along $(1\bar{1}0)$ planes of β-LLTO and feature interfacial atomic layer with rocksalt structure. They exhibit an increased diffusion barrier, which inhibits Li migration in bulk LLTO.

Additionally, Zhu et al. (2020) reported on planar defects forming closed loops along all {100} directions [136]. The authors define these non-periodic features as single-atom-layer traps that block the Li^+ ion migration and degrade the total ionic conductivity. They related the local structure and chemical composition of these defects to $(Li_{0.37}Ti_{0.33}O)^{0.31-}$ phase that is isostructural with {001} of the rock-salt γ-Li_2TiO_3 phase. With ab initio molecular dynamics they showed that the diffusivity of Li parallel to the defect is slower than in bulk LLTO due to compressed volume, whereas perpendicular transport of Li across the defect is blocked by neighboring La-rich layers and a low amount of vacancies.

1.3.3.3 Effect of grain boundaries

Grain boundaries have a few orders of magnitude lower ionic conductivity than the LLTO grains. Their low conductivity is related to lattice mismatch due to the random orientation of LLTO grains. It causes structural distortions like the deformation of TiO_6 polyhedra and the formation of a binary Ti-O compound layer that disables Li^+ transport [46], [47], [138]. Chemical changes at grain boundaries include a reduction of Ti^{4+} to Ti^{3+} and a decrease in La^{3+} [46] and Li^+ concentration [46], [135], [137], [143]. Depletion of Li^+ is caused by the positively charged grain boundary and the space-charge layer surrounding the grain boundary represents the physical origin of grain boundary resistance [47], [139].

Typically, the average size of LLTO grains in sintered ceramics is in the range of a few micrometers [47], [144]. As a result, the contribution of grain boundaries to the total conductivity is significant. Strategies to reduce the impact of grain boundaries on the total ionic conductivity involve processing in a moisture-free environment to avoid the formation of Li-rich secondary phases [45]. Additionally, the negative contribution of the grain boundaries to the total ionic conductivity can be mitigated by improving the ionic conductivity of grain boundaries and by preparation of coarse-grained LLTO ceramics with a lower fraction of grain boundaries.

Coarse-grained microstructure with improved density was achieved by sintering LLTO ceramics at higher temperatures and with the addition of excess Li to promote the formation of Li-rich boundaries that facilitate Li^+ ion mobility [135].

De Oliveira et al. (2014) reduced the volume fraction of grain boundaries by introducing $LaAlO_3$ single crystal seeds into the ceramic matrix. The newly formed LLTO composite with some exaggeratedly grown grains exhibited higher conductivity in comparison to the fine-grained LLTO ceramics [145]. The contribution of grain boundaries can be also reduced by templated grain growth using $La_2Ti_2O_7$ platelets [146]. Another approach is by doping with Sr^{2+} [111], [147], Ba^{2+} [128], Y^{3+} [148], and Nd^{3+} [149] to obtain larger LLTO grains or adding Al_2O_3 and SiO_2 that react with Li and form a thin amorphous interfacial layer at the grain boundaries, which promote Li^+ transfer between grains [150], [151].

1.4 Microstructure Development in Perovskite-Based Ceramics

1.4.1 Normal grain growth

During conventional solid-state sintering of ceramics, the calcined powder is exposed to high firing temperatures, which leads to densification and strengthening due to the diffusion of atoms. Grain growth reduces the amount of grain boundaries, that represent high-energy areas due to inefficient packing of the atoms. The process includes three stages (Figure 1.15) [152], [153], [154]:

1. In the initial state, the particles oscillate and rearrange. The adjacent particles start to form contact areas predominantly through surface diffusion of atoms. The driving force of the neck formation is the energy gradient from different curvatures of the particles and the necks. At this stage, there is no significant change in relative density (around 3%) or grain growth.
2. In the intermediate stage, the particles grow by merging of previously formed necks. The driving force for sintering is the elimination of interfacial, surface, and finally grain boundary area. The grain growth is still limited since the grains are separated by the pores, which form continuous channels along grain boundaries. The density reaches up to 93% of the theoretical value.
3. The final stage is characterized by excessive grain growth and reduction and isolation or even removal of the pores, which leads to the compaction of the powder to a dense pellet.

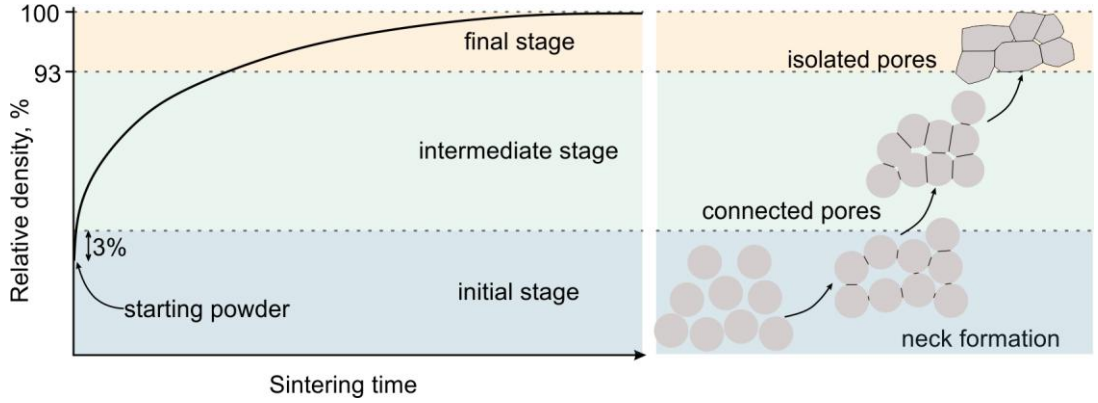

Figure 1.15: Typical densification curve of a powder with time during solid-state sintering (left), and schematics of grain growth during different sintering stages (right) (adjusted by [152], [155]).

Grain growth first occurs by movement of the material from the particle interior or grain boundary to the neck, which results in increasing the neck size and densification of the material. Further coarsening of the grains is governed by the movement of grain boundaries in order to obtain a larger radius of boundary curvature and thus reduce total grain boundary energy [153]. Larger grains will grow at the expense of the smaller grains according to the Ostwald ripening process, which decreases the number of grains and increases their size [152]. The grain boundaries move by short-range diffusion of atoms across the boundary in the opposite direction as the overall movement of the boundary (from the higher curvature to the lower curvature side). Since grain growth is a thermally-

activated process, higher sintering temperatures and faster diffusion of atoms can assist the formation of coarse microstructure [156], [157].

Sintering also influences the size and shape of the pores and contributes to the compaction of the powder and increased density [153]. Grain growth usually occurs with pore drag which slows down the movement of the grain boundary and distorts the pore shape [152]. As the grain growth continues, the pores are enclosed in spherical voids. During the growth, pores can detach from grain boundaries and remain trapped inside the grains, their further reduction would require lattice diffusion [153], [157].

1.4.2 Abnormal grain growth

Unlike normal grain growth, where grain size uniformly increases with sintering time and the size distribution is relatively invariable, abnormal or exaggerated grain growth causes bimodal grain size distribution with few extra large grains and many small grains [158].

Abnormal grain growth can be observed in single-phase systems but is more typical for multi-phase systems. It can stem from the bimodal distribution of initial particle sizes, pore pinning, preferential wetting, and the presence of impurities or dopants. In ceramics, abnormal grain growth is usually not desired, as it can have an adverse influence on the physical properties, especially mechanical, thermal, and electrical properties [153], [159].

The addition of a small amount of liquid phase or partial melting of one of the components during sintering can induce liquid-phase-assisted abnormal growth of grains. Partial wetting, caused by the presence of a small amount of liquid phase, leads to a nonuniform distribution of diffusion processes and hence exaggerated growth of certain grains. Such growth was observed for example in ZnO ceramics with small additions of Bi_2O_3 [160], [161].

The criterion to determine the start of exaggerated grain growth is

$$D_{max}/(D) > 5 \qquad \text{(Eq. 7)},$$

where D_{max} is the diameter of the maximum observed and (D) is the averaged three-dimensional grain diameter [162]. During annealing, some grains grow faster due to high local rates of interface migration, while the growth of other grains is negligible [158]. The growth of large grains stops after these grains impinge with each other [158], [163].

Anisotropic grain growth can be also related to the incorporation of dopants to specific crystal planes in a doped or slightly nonstoichiometric starting powder. This triggers the formation of crystallographic 2D defects [155], like anti-phase boundaries, twin boundaries, inversion boundaries, or polytype stacking faults [159], [160], [164], [165], [166]. These defects are embedded inside the matrix grains and have a locally different structure and composition. For example, doping of spinel $MgAl_2O_4$ with BeO leads to abundant {111} twinning of spinel, and at higher doping concentrations even to the formation of polytypic sequences. In the initial stages of grain growth, anisotropic growth of spinel occurs along the twin boundaries that accommodate Be ions [167].

Exaggerated grain growth results in the formation of elongated and faceted grains that are characterized by straight boundaries parallel to the long axis of the grain and a high aspect ratio in edge-on projection [157]. The phenomenon of fast and preferential growth of matrix grains as a result of the formation of planar defects was observed also in perovskite-based ceramics as described in the next chapter.

1.4.2.1 Exaggerated grain growth in oxide perovskite-based ceramics

In oxide perovskite-based ceramics, exaggerated grain growth was observed in $BaTiO_3$ sintered under reducing conditions, doped $CaTiO_3$, and nonstoichiometric $SrTiO_3$ and $CaTiO_3$. Such growth is related to phase transformations, and faceting due to the presence of attachment sites in the form of 2D defects like twin boundaries and RP defects.

In $BaTiO_3$, exaggerated and anisotropic grain growth is related to the phase transition from cubic to hexagonal $BaTiO_3$ modification. At lower temperatures and under reducing conditions, the exaggerated grain growth is related to the formation of (111) twin boundaries inside cubic $BaTiO_3$ grains [159], [168]. At higher temperatures and under reducing conditions, the phase transition occurs by dissolution of matrix cubic $BaTiO_3$ grains and precipitation of grains with hexagonal symmetry. The growth of hexagonal grains is analogous to the growth of (111) twins in cubic $BaTiO_3$ and is pronounced in the directions of the prismatic planes [159].

Polytype-induced anisotropic grain growth can also be triggered by doping, for example by doping $CaTiO_3$ with SrO or BaO [164], [165]. The dopants are incorporated into planar defects within the host crystal (Figure 1.16a), forming polysome sequences that structurally correspond to RP-type planar defects. These sequences are characterized by the interchanging of pseudo-perovskite blocks of varying thicknesses and composition of the main phase, and separated by layers with different chemistry and structure (Figure 1.16b) [169]. These sequences nucleate within the matrix crystallites at the initial stages of sintering. As the microstructure develops, the introduced anisotropy in the matrix grains causes them to preferentially grow in the direction of the polytype, leading to exaggerated grain growth [165].

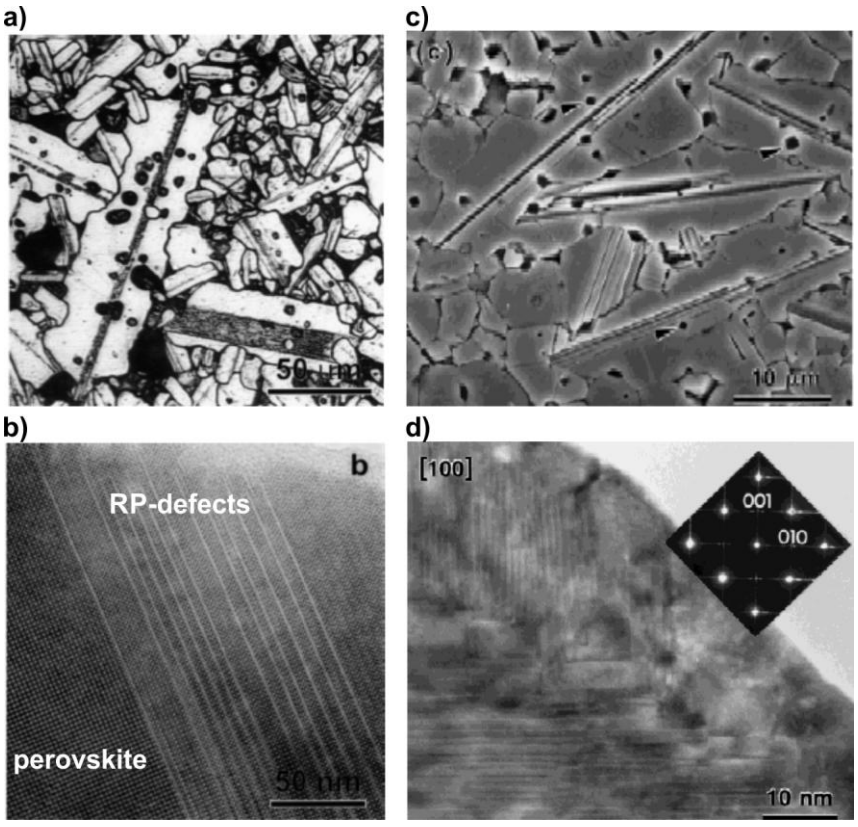

Figure 1.16: (a) Exaggerated growth in BaO-doped $CaTiO_3$. (b) Ordered polytypic sequence in $CaTiO_3$ perovskite matrix (adapted by [165]). (c) Planar defects in $SrTiO_3$ with excess SrO. (d) RP faults extend along [100] lattice planes (adapted by [166]).

Preferential exaggerated grain growth of the matrix grains in the direction parallel to the planar defects was also observed in $SrTiO_3$ and $CaTiO_3$ with a small excess of SrO and CaO, respectively [166], [169], [170]. The nonstoichiometry is compensated by the formation of RP defects (Figure 1.16c) [170]. Grains with planar defects exhibit elongated morphology and can even penetrate into neighboring grains, indicating a strong enhancing effect of these defects on grain growth. TEM studies suggest that RP faults extend along [100] lattice planes and are usually ordered (Figure 1.16d). In SrO-doped $SrTiO_3$ the exaggerated growth occurs at a sintering temperature of 1450 °C, however, at higher temperatures of 1640 °C the grain size is relatively uniform and the RP defects are present only in polytype-rich grains [166], indicating their high thermal stability.

1.5 Methods for Characterization of Li-Containing Materials

Li compounds are inherently challenging to characterize due to the light atomic weight of lithium. The low atomic number of Li (Z=3) limits its detectability in various analytical techniques. For instance, it causes weak electron and X-ray scattering in electron microscopy and X-ray diffraction, respectively, as well as weaker signals in spectroscopy methods such as nuclear magnetic resonance and mass spectrometry. Although various analytical techniques exist for the analysis of Li-containing materials (Figure 1.17), each comes with its own set of advantages and limitations, often failing to provide the full information and deliver comprehensive insights.

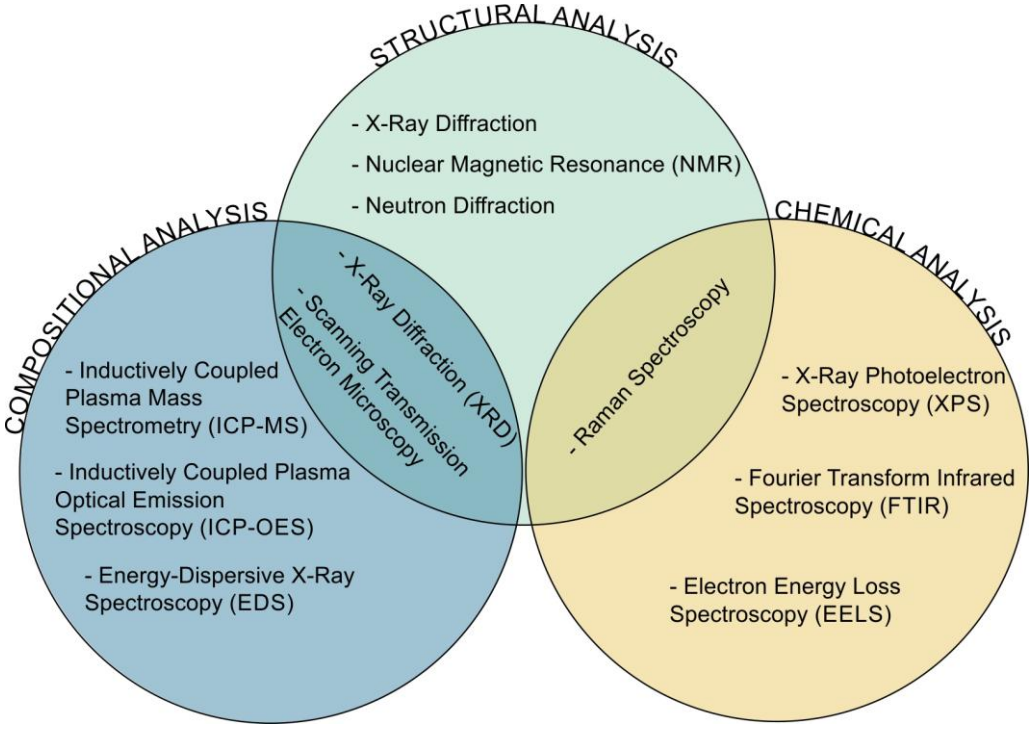

Figure 1.17: Characterization techniques categorized by the information they provide.

The most commonly applied techniques for the analysis of Li-ion batteries as one of the most important Li-containing materials are X-ray diffraction (XRD), neutron diffraction (ND), nuclear magnetic resonance (NMR), X-ray photoelectron spectroscopy (XPS), Raman and Fourier transform infrared spectroscopy (FTIR), inductively coupled plasma

mass spectrometry and optical emission spectroscopy (ICP-MS and ICP-OES) and microscopy methods, especially scanning electron microscopy (SEM) with energy-dispersive X-ray analysis (EDS) and scanning transmission microscopy (STEM) with EDS and electron energy loss spectroscopy (EELS).

ND and NMR spectroscopy provide structural information about the material. ND is similar to the XRD technique. As the neutrons interact directly with the nucleus of the atoms in the sample, this method is highly sensitive to light elements like lithium, even in the presence of heavier atoms. It enables the determination of the crystal space group, lattice parameters and precise atomic positions in the structure, including Li [107], [171]. ND is mostly used for the analysis of structural changes in electrode materials during cycling and enables insight into the mechanisms of Li intercalation and de-intercalation [172]. NMR offers detailed information about the local structural environment, such as the bonding of individual atoms. It is used for the investigation of molecular structure and dynamics in lithium-containing materials. This is especially important for studying the electrolyte-electrode interface and the structural analysis of the interface passivation layer [173].

Raman, FTIR, and X-ray photoelectron spectroscopy are methods for chemical analysis. Raman and FTIR spectroscopy are used to characterize molecular composition and structure, bonding characteristics, and functional groups. Raman spectroscopy also provides detailed structural information, such as the identification of different phases and polymorphs [174]. In lithium-containing compounds, Raman spectroscopy is mostly used to study intercalation processes [175], [176], while FTIR is commonly used for the identification of functional groups and studies of chemical bonding [177]. XPS provides information on the elemental composition of the sample surface (analyzing the topmost 10 nm) and enables investigation of surface oxidation states and chemical environments [178]. Li-containing materials can pose a challenge for XPS analysis due to binding-energy shifts. These shifts are related to the reactivity of lithium and the formation of a passivation layer containing Li-hydroxide and carbonate [179], [180].

In the following sections, the methods used for the characterization of materials within the thesis are described in greater detail, with an emphasis on STEM as the main characterization technique.

1.5.1 X-ray diffraction (XRD)

X-ray diffraction (XRD) is one of the most widely used analytical techniques for the identification of chemical composition and crystalline structure. The working principle includes the interaction of monochromatic X-rays with the sample and the collection of X-rays diffracted from the lattice planes of the material. At specific θ angles, parallel and coherent X-rays are elastically scattered from sets of lattice planes and interfere constructively, as defined by Bragg's law

$$2dsin\theta = n\lambda \qquad \text{(Eq. 8)},$$

where d is the spacing between lattice planes, θ is the incident angle, n is the order of diffraction and λ is the wavelength of X-rays. The intensity of the scattered beam is measured as a function of the scattering angle (2θ) [181], producing a diffraction pattern that is specific for each crystalline material.

XRD can also provide quantitative information like the determination of the crystallite size, the degree of preferred crystal orientation, and by using Rietveld refinement proportion of phases and lattice parameters. The information on the lattice constants is especially important for the functional properties of electrolyte materials since it affects

the lithium ion mobility and activation energy [182]. Furthermore, it can be used for tracking slight changes of the lattice parameters due to the incorporation of different dopant atoms into the crystal structure.

1.5.2 Inductively Coupled Plasma Mass Spectrometry (ICP-MS) and Optical Emission Spectroscopy (ICP-OES)

Inductively Coupled Plasma Mass Spectrometry (ICP-MS) and Optical Emission Spectroscopy (ICP-OES) are techniques that enable high-precision elemental analysis of bulk samples. In both methods, the sample is ionized with an inductively coupled plasma (a high-temperature Ar plasma). In ICP-MS the ions are subsequently transferred to the mass spectrometer detector, where ions are separated according to their mass-to-charge ratio [183]. ICP-OES measures light emitted by elements as electrons return to the ground state, with each element having a specific wavelength. While both methods are commonly used, ICP-MS has a higher detection limit and is more suitable for trace element analysis [184]. Quantification in both techniques is achieved by comparing the intensity of the measured signal to that of calibration standards.

Laser ablation ICP-MS (LA-ICP-MS) is a variant of ICP-MS that ablates the surface of a solid sample using a pulsed focused laser beam. The sample material is ionized and the plume of particles and ions is transferred to ICP-MS with argon or helium gas flow. The laser ablates features as small as 10 µm and the measurements are converted into maps, providing spatial information on elemental distribution [185]. The quality of the maps depends on the laser beam diameter, scanning rate and integration time (dwell time per mass) [186], [187], [188]. Using calibration standards, quantitative analysis of most elements with a detection limit of ppb or ppt, including Li, is possible [185].

1.5.3 Scanning Electron Microscopy (SEM) with Energy-Dispersive X-Ray Spectroscopy (EDS)

Scanning electron microscopy (SEM) is based on scanning a focused beam of accelerated electrons across the sample's surface, the interaction of the electron beam with the sample, and the collection of signals from different depths of the interaction volume in the sample with various detectors. The most commonly used signals for imaging are secondary electrons and backscattered electrons, which provide information on the surface's topography and composition, respectively.

In energy-dispersive X-ray spectroscopy (EDS), the primary beam electron ejects an inner shell electron from the sample, causing a transition of the outer shell electron to a lower energy state to fill the vacancy. During the transition, X-rays are generated with the energy corresponding to the energy difference between the orbitals. These X-rays are detected by a semiconductor detector, where each X-ray photon generates a specific number of electron-hole pairs for every 3.8 eV of X-ray energy. A negative voltage bias in the detector separates the electrons and holes, and the resulting current is collected. The current is then analyzed to determine the energy of the X-rays. Peaks in the EDS spectrum represent the characteristic X-ray energies of different elements, allowing for their identification and quantification [189].

Due to its low atomic number, Li emits X-rays with very low energy when excited, producing a weak signal that is below the detection limit for standard EDS systems. Additionally, low-energy X-rays of Li are prone to absorption by the detector window or air. Despite these limitations, EDS can be used for the indirect determination of lithium content in LLTO, based on the La:Ti ratio.

1.5.4 Scanning Transmission Electron Microscopy (STEM)

Scanning transmission electron microscopy (STEM) with electron energy loss spectroscopy (EELS) is an important tool for the research of battery materials because it provides local information on the structure and composition, unlike most other techniques, that acquire spatially averaged information [190]. Due to the small diameter of the electron probe in aberration-corrected STEM, spatial resolution below one angstrom can be reached, which is beneficial for atomic-scale analysis of structural specifics like planar defects and other interfaces.

The path of the electron beam passing through the STEM column is illustrated in Figure 1.18. Accelerated electrons are emitted from the electron gun. The acceleration voltage determines the energy of electrons, which affects their wavelength and is directly related to the spatial resolution, which is approximately half the wavelength of the electrons. For example, in a STEM operating at an accelerating voltage of 200 kV, the theoretical resolution can reach ~0.027 Å (2.7 pm). However, the actual spatial resolution is often lower due to probe and image aberrations. To mitigate these aberrations, advanced STEMs can be equipped with aberration correctors. For example, a probe corrector corrects the spherical aberrations in the electron beam before it interacts with the sample, enabling the beam to be focused into a much smaller spot size for improved spatial resolution in imaging [191]. Subsequently, a set of objective lenses focuses the beam on the sample, which is crucial for attaining higher image resolution. The focused beam is then rastered across the sample surface using scanning coils [192].

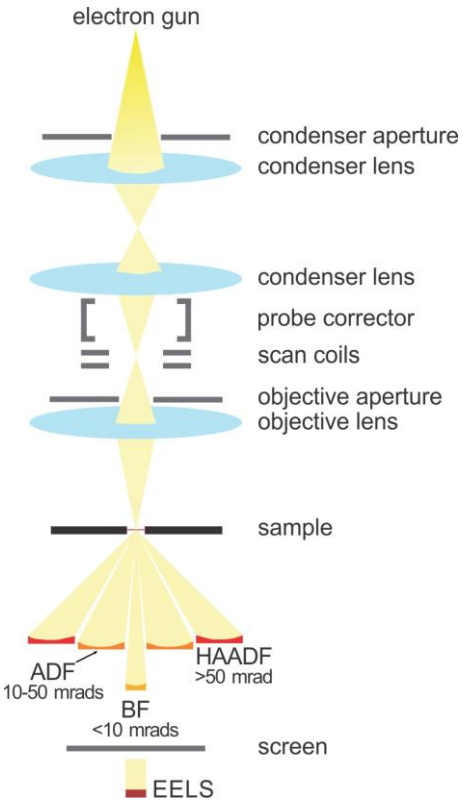

Figure 1.18: Schematics of STEM components (adapted by [193]).

The electrons from the beam diffract on the atomic columns of the specimen, and the signals are collected as a function of diffraction angle by detectors located in the diffraction

plane [192]. Electrons transmitted at low angles relative to the optic axis (<10 mrad) are detected on the bright-field (BF) detector, while higher-angle electrons (10-50 mrad) are collected at the annular dark field (ADF) detector. BF images are analogous to the phase-contrast image in conventional TEM, with mainly mass-thickness and diffraction contrast contributing to the image formation. ADF detector collects Bragg-diffracted electrons. Electrons scattered at very high angles (>50 mrad) are detected on the high-angle annular dark field (HAADF) detector, where the scattering intensity depends on the average atomic number of the atomic columns.

1.5.4.1 Atomic-scale HAADF-STEM

In STEM, the atomic-scale structural and indirectly also compositional features are imaged with a high-angle annular dark field (HAADF) detector by collecting transmitted electrons that were elastically scattered on atomic nuclei. The intensity contrast in HAADF-STEM images is sensitive to the average atomic number of the atomic column Z [194]. At first approximation, the intensity of atomic columns in HAADF-STEM images is proportional to Z^n, where n varies between 1.7 and 2, depending on the experimental parameters and sample specifics, such as thickness, which causes multiple scattering, and average composition [195], [196]. Heavier elements scatter more strongly, resulting in higher intensities of atomic columns, while lighter elements, especially in the presence of heavier atoms, produce weak signals on the HAADF detector. The light elements can be visualized in bright-field (BF) images.

While qualitative interpretation of atomic-scale HAADF-STEM images is relatively straightforward, quantitative evaluation can be misleading as the contrast can be altered by various factors, besides the average Z of the atomic column [196]. For this reason, comparing experimental images with simulations is necessary for accurate quantitative analysis of HAADF images.

The contrast in HAADF-STEM images is inherently influenced by electron microscope parameters, such as convergence angle, defocus, and detector angle [197], [198]. For example, a smaller convergence angle increases the projected atomic brightness and atom spot size. A larger detector angle range produces stronger intensities of the atomic columns; however, a small detector angle can lead to the detection of other signals like Bragg reflections [195].

While the primary source of contrast in HAADF (Z-contrast) imaging is Rutherford elastic scattering, inelastic scattering of electrons also occurs due to the thermal vibrations of atoms around their equilibrium positions, known as thermal diffuse scattering (TDS) [199]. Phonon scattering is incoherent and results in a diffuse intensity distribution [196], [200].

Additionally, atomic column intensities depend on sample thickness. The intensity and the contribution of the background monotonically increase with the thickness [196], [201]. Nevertheless, at a critical thickness of around 60 nm, the intensity of atomic columns remains relatively constant due to the beam broadening to the neighboring columns [201].

The variation in contrast is also dependent on beam propagation, especially in thicker samples. The beam can focus along the atomic column, i.e. dechanneling effect, or scatter to the neighboring columns, i.e. cross-talk [202]. Dechanneling can occur due to slight misorientation of the sample, which decreases the signal-to-noise ratio of atomic columns [203]. These effects are also related to the composition of the column and its surrounding columns. The channeling of the probe can enable the determination of the depth of an impurity atom because the probe further down the column from the impurity atom is more focused and atoms scatter to higher angles, which increases their intensity [204]. Balades et al. (2018) showed that the intensity is also transferred between neighboring atomic

columns with different compositions, from columns with higher average Z to columns with smaller Z [205].

High-angle scattering is dominated by 1s Bloch states (eigenstates) with the lowest energy. These states are localized around the atomic columns, where the electron density amplitude peaks at the center of the columns. However, other states can also contribute to the signal, especially if the atomic columns are closely spaced, which can lead to excitation of the neighboring columns, or when the columns contain heavier atoms (have a high average atomic number) [206], [207]. It was found that for heavier atoms, the 1s states are also excited at smaller thicknesses, but the oscillations diminish to the surroundings due to the dephasing of unbound states. At larger thicknesses around 40–60 nm, 2s states with longer wavelengths are also excited, which contributes to the higher intensity of heavier columns with increasing thickness. The excitation of 2s states also influences the intensity in structures with different degrees of ordering. In disordered structures where lighter and heavier atoms are randomly distributed in the columns, the intensity of atomic columns with the same thickness is higher in comparison to the ordered lattice. This suggests that in an ordered structure, heavier columns mostly contribute to the intensity with 2s Bloch states, but the average intensity is largely reduced by the lighter columns. On the other hand, in disordered structures, the 2s states are excited in all columns, yielding a higher average intensity of these columns (Figure 1.19a) [207]. The arrangement of atoms along the atomic column also influences the intensity of a specific column. The channeling of the probe and thus the intensity of the atomic column is enhanced when lighter atoms occupy the topmost columns in comparison to columns with alternating ordering of atoms (Figure 1.19b) [208].

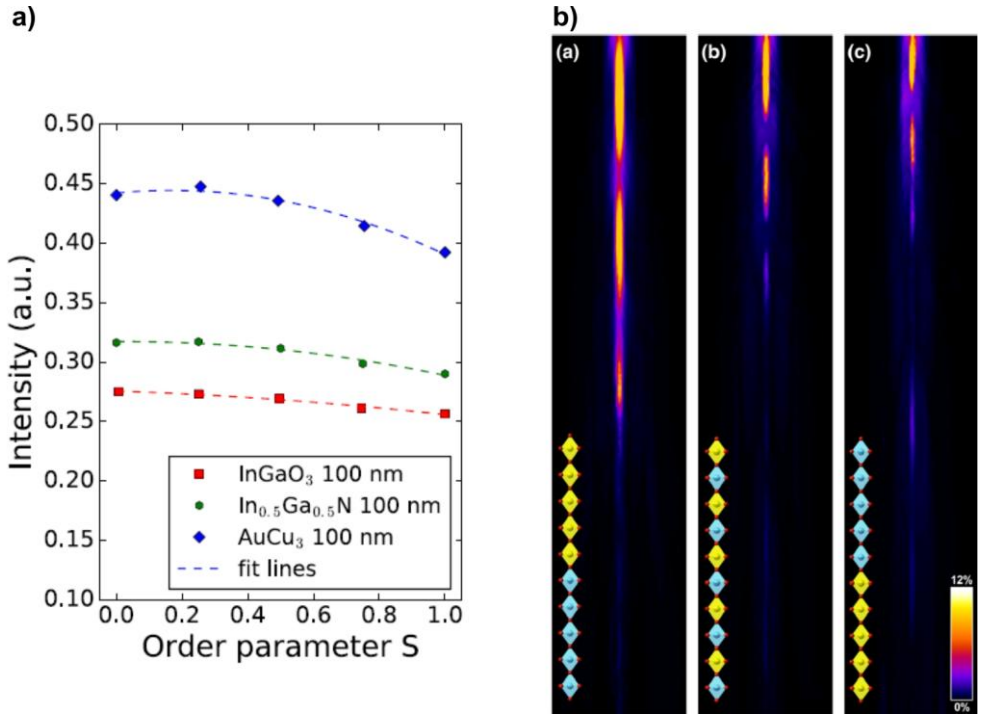

Figure 1.19: (a) Intensity in structures with a thickness of 100 nm and different compositions and varying long-range order. S = 0 denotes a completely random distribution of atoms, while S = 1 denotes a perfectly ordered crystal (reproduced from [207]). (b) Scattering of the probe in atomic column with identical composition of $Cr_{0.5}Re_{0.5}$ and different arrangement of atoms along the column. Yellow atoms represent Cr and blue atoms represent heavier Re atoms (reproduced from [208]).

Finally, the HAADF-STEM intensity is affected by the presence of an amorphous layer on the sample surface, which usually forms during the TEM sample preparation. The presence of an amorphous layer reduces the contrast in HAADF images because a portion of the probe intensity is partially transformed into a Gaussian background [209]. This can lead to incorrect quantitative determination of atomic column composition or specimen thickness [210].

1.5.4.2 Quantitative analysis of atomic-scale STEM HAADF-STEM images

In order to quantify atomic-scale HAADF-STEM images, experimental images must be compared to image simulations. Different approaches have been developed to simulate HAADF-STEM images, like the Bloch-wave or Behte method and the multi-slice frozen phonon simulations. The Bloch-wave simulations are mostly used for materials with a small unit cell and periodic structure and describe the wave function of multiple scattering electrons by three-dimensional Bloch waves [211].

Multi-slice frozen phonon simulations replicate the propagation of a probe through a specimen and can be used for the quantitative interpretation of experimental HAADF-STEM images. Simulations successfully reproduce most features of the experimental images and describe the propagation of the wave function through the crystal with discrete alternating steps. First, the simulation calculates the phase shift of the electron beam that interacts with the specimen potential in one slice. Secondly, the phase-shifted probe propagates to the next layer in the atomic column. The steps are repeated until the electron beam reaches the exit surface [212].

To obtain better agreement with the experimental images, simulations also include TDS on the HAADF detector, in addition to the elastic wave function. TDS is modeled by averaging the scattered intensity for random atom displacements, referred to as the frozen phonon approximation [212], [213]. The approximation considers that the interaction time between beam electrons and a specimen is much shorter than the vibration period of the specimen atoms [214] and also accounts for other effects on the intensity, like probe channeling [215].

Besides matching the experimental microscope parameters and specimen orientation and tilt with simulations, accurate comparison of images also requires normalization of image intensity to the incident beam intensity [216]. HAADF-STEM image intensity is a combination of atomic column intensities and the background signal, which gives a non-local signal and arises from average scattering from the material. For this reason, the experimental image background needs to be subtracted from the image intensity [217]. This procedure is not needed for simulated images as the TDS included in the calculation scales background and column intensities by the same factor and does not produce large background intensity as in experimental images [201].

Comparison of HAADF-STEM images with simulations offers valuable insights into factors that predominately contribute to the image contrast and can help with the optimization of microscope parameters. More importantly, simulations assist the interpretation of experimental data, providing information on sample thickness and quantitative details on the compositional changes, thus facilitating a deeper understanding of processes on the atomic scale.

1.5.4.3 Electron Energy-Loss Spectroscopy (EELS)

When passing through the specimen, some electrons lose their energy due to collisions with electrons in the sample. This inelastic scattering causes energy losses that typically range from 0 eV to 3 keV. After the interaction of electrons with the samples, the electrons pass through the spectrometer (magnetic prism), where they are separated based on their

absolute energy using a magnetic field that is perpendicular to the electrons' momentum. The dispersed electrons are detected by a detector, which measures the intensity of electrons at different energy losses. The resulting EELS spectrum shows intensity as a function of the energy loss and is composed of three main parts: the zero-loss peak, low-loss region, and core loss region (Figure 1.20).

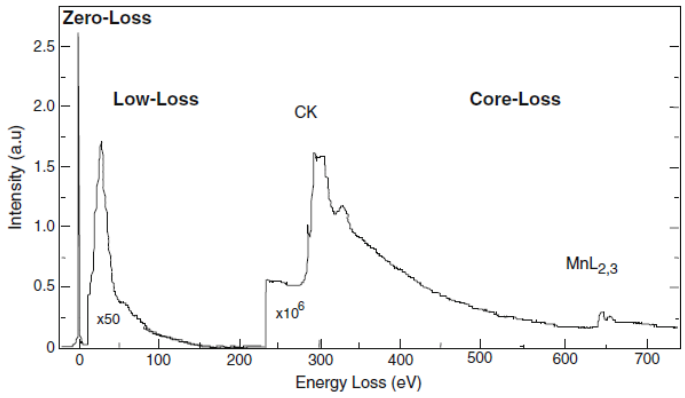

Figure 1.20: EELS spectrum with three main regions (from [193]).

The zero-loss peak (0 to 10 eV) corresponds to electrons that did not undergo any significant energy loss. It can be used for the calculation of the sample thickness at the analyzed position [193]. Additionally, it provides a reference position for the rest of the spectrum. The width of the zero-loss peak defines the energy spread of the electron source and can be improved by using a monochromator. The low-loss region (10 to 60 eV) represents the energy losses that are associated with weakly bound outer shell electrons. Low-loss edges are a result of plasmon excitations (resonance of valence electrons) and valence-to-conduction band transitions. The high-energy loss region (>60 eV), also referred to as the energy loss near edge structure (ELNES), appears due to core-shell ionization, where the electrons are excited to an unoccupied higher-lying state or free electron state [218]. Each species has a characteristic ionization energy and can be used for elemental analysis of the sample. Additionally, by inspecting the fine ELNES structure, electronic structure, bonding, and valence information can be extracted [192], [193]. With increasing sample thickness, the beam electrons undergo multiple scattering as they interact with the sample, which reduces the signal-to-background ratio and the visibility of the EELS edges [218].

EELS spectra can be acquired as single spectra from selected sample regions (point, area). Alternatively, EELS spectra can be acquired in spatially resolved maps referred to as spectrum imaging (SI), where information about electron energy loss is collected for each pixel in a scanned image, providing detailed spatial and spectral information [219].

Chapter 2

Research Aim and Hypothesis

The research of solid electrolyte materials is crucial for the development of more efficient and reliable energy storage solutions in the context of greener and more sustainable energy technologies. The research is not only limited to obtaining materials with high ionic conductivity but also to understanding the fundamentals of chemical and structural properties of electrolyte materials and underlying mechanisms that lead to superior properties. This thesis focuses on the development of double perovskite oxide lithium lanthanum titanate (LLTO), a material that according to previous research holds great potential for applications as a solid electrolyte.

In LLTO, the total ionic conductivity is significantly reduced by resistive grain boundaries. Gaining a deeper understanding of microstructure development in LLTO ceramics can provide valuable insights for the improvement of the electrical properties, necessary for the enhancement of its performance in battery applications.

The primary goal of the dissertation is to prepare coarse-grained LLTO ceramics with conventional solid-state synthesis. This will be achieved through optimization of the synthesis parameters such as the starting compositions in terms of the La:Ti ratio and sintering conditions. The dissertation extends to the investigation of the role of planar defects on grain growth, microstructure development, and functional properties for applications of LLTO as a solid electrolyte. A substantial part of the work is dedicated to quantitative structural and compositional characterization of LLTO ceramics with RP-type defects using frozen phonon multi-slice image simulations in order to advance the fundamental understanding of the atomic-scale processes and their implications for final functional properties.

Combining various advanced characterization techniques the following questions will be addressed within the proposed doctoral dissertation:

1. How to prepare coarse-grained LLTO ceramics with solid-state sintering?
2. What impact does the starting composition have on LLTO grain growth?
3. What is the correlation between starting powder composition, microstructure, and functional properties?
4. How does Li:La:Ti ratio in the initial LLTO composition influence the formation of RP-type defects?
5. What is the structure and composition of RP-type defects within LLTO?
6. What are the thermodynamic reasons for the specific microstructure development in LLTO with La:Ti=0.605?

The results of the doctoral dissertation are divided into five main parts. The first part focuses on the influence of the synthesis parameters and starting LLTO composition on the structure and microstructure of LLTO ceramics. In the second part, a detailed atomic-scale analysis of the planar defects inside the LLTO with an initial La:Ti ratio of 0.605 is described. A thermodynamic study of the formation and recrystallization of RP-type defects is given in the third part. The fourth part provides a comprehensive description of microstructure development in LLTO with 0.605 under the influence of RP-type planar defects. The final part of this dissertation presents the measurement of ionic conductivities in prepared LLTO samples.

The findings of this doctoral dissertation are published in Journal of the European Ceramic Society with the title *Exaggerated Grain Growth and the Development of Coarse-grained Microstructures in Lithium Lanthanum Titanate Perovskite Ceramics* and in journal ACS Nano with the title *Transient Ruddlesden–Popper-Type Defects and Their Influence on Grain Growth and Properties of Lithium Lanthanum Titanate Solid Electrolyte.*

Chapter 3

Materials and Methods

3.1 Sample Preparation

Ceramic pellets were prepared according to the conventional solid-state approach from the starting Li_2CO_3 (99.998%, Alfa Aesar), La_2O_3, (99.99%, Alfa Aesar), and TiO_2 (≥99.9%, Sigma Aldrich) powders. La_2O_3 powder was annealed at 800 °C for 10 hours before weighing to remove the absorbed water. All the compositions contained 20 mol% Li_2CO_3 excess to compensate for the loss of lithium due to volatilization during the high-temperature sintering. The amount of excess Li_2CO_3 was chosen according to the preliminary experiments and literature data. The initial composition corresponds to the stoichiometric starting powder $Li_{0.33}La_{0.56}\square_{0.11}TiO_3$ phase with excess Li_2CO_3, and a molar ratio of the starting compounds is Li_2CO_3:La_2O_3:TiO_2 = 0.011:0.0151:0.054. Other samples contain different additions of La_2O_3, resulting in molar ratios between starting components Li_2CO_3:La_2O_3:TiO_2 as given in Table 3.1 and presented in molar percentages in a ternary phase diagram in Figure 3.1.

Table 3.1: Starting compositions of prepared LLTO samples.

Sample name	Molar ratio			La:Ti ratio
	Li_2CO_3	La_2O_3	TiO_2	
La:Ti=0.560	0.011	0.0151	0.054	0.560
La:Ti=0.589	0.011	0.0158	0.054	0.589
La:Ti=0.605	0.011	0.0163	0.054	0.605
La:Ti=0.622	0.011	0.0167	0.054	0.622

The starting powders were mixed and homogenized in a planetary ball mill with ZrO_2 balls at 200 rpm for 0.5 hour in ethanol. After drying the homogenized mixture at 120 °C, the obtained powders were pressed in pellets with a diameter of 10 mm at a uniaxial pressure of 100 MPa and calcined at 800 °C for 8 hours in a tube furnace. The calcined pellets were crushed, milled, dried, and re-pressed into pellets. Final sintering was performed at different temperatures from 1100 °C to 1350 °C for 12 hours in air with heating and cooling rates of 10 °C/min. In addition, compositions were quenched after sintering at 1350 °C.

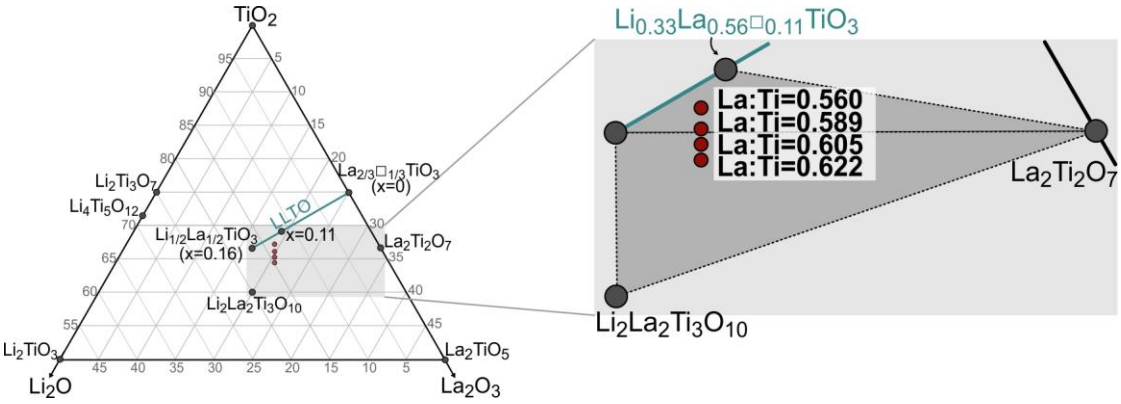

Figure 3.1: Initial compositions of the LLTO samples positioned in the ternary phase diagram.

3.2 Characterization Techniques

3.2.1 Phase analysis

Identification of the crystalline phases was carried out by X-ray diffraction (XRD; Empyrean, Malvern PANalytical, Malvern, United Kingdom) with Cu radiation (k = 1.54187 Å) and equipped with a PIXcel 1D detector in scanning line mode. Data were acquired in Bragg-Brentano geometry within an angular range of 10° to 70° 2θ with a step size of 0.026° 2θ and a collection time of 100 s per step. Phase analysis was performed using PANalytical X'Pert Highscore Plus V 5.2 with the PDF-4 database.

3.2.2 Densification kinetics

To determine the optimal sintering temperature for LLTO samples, densification plots were recorded on a heating-stage microscope (Ernst Leitz GmbH, Wetzlar, Germany). For the analysis, the calcined powder was compacted in a steel die to obtain pellets with a diameter of 3 mm. The analyses were performed in the temperature range up to 1350 °C with a heating rate of 10 °C/min.

3.2.3 Density measurements

The absolute density of the samples after sintering at 1350 °C was measured in absolute ethanol according to the Archimedes method.

3.2.4 Microstructure analyses

For the analysis of microstructural characteristics, the sintered pellets were transversely cut in half and the cross-sections were ground and polished, finally with 0.25 µm diamond paste. Microstructural observations were performed on a scanning electron microscope (SEM; Thermo Fisher Quanta 650 ESEM, Massachusetts, USA) with a thermionic electron source, equipped with an energy dispersive X-ray spectrometer for chemical analysis of the samples (EDS; Oxford Instruments, AZtec Live, Ultim Max SDD 40 mm^2). First, polished cross-sections were examined and afterward, the cross-sections were thermally etched for ~15 minutes at a temperature ~100 °C below the sintering temperature to reveal important microstructural features such as grains, grain boundaries, and planar defects.

3.2.5 Atomic-scale analyses

Samples for scanning transmission electron microscopy (STEM) were prepared by the conventional TEM sample preparation approach. 3 mm disks were cut from the samples, mechanically thinned to around 100 µm, and dimpled to ~20 µm in the disc center (Dimple grinder, Gatan Inc., Warrendale). The dimpled samples were ion-milled to electron transparency using 4 keV Ar ions at an angle of 8° from both sides (PIPS 691, Gatan Inc., Pleasanton, USA). Prior to the TEM analyses, the samples were coated with a thin layer of carbon to prevent charging under the high-energy electron beam.

STEM analyses were performed on probe-corrected atomic-resolution scanning TEM (STEM; JEOL ARM200 CF, Jeol Ltd., Tokyo, Japan). Atomically-resolved images were collected using a high-angle annular dark-field (HAADF) detector with inner and outer semi-angles of 68 and 180 mrad, respectively. Stacks of images (10 frames) were acquired at a higher scanning speed (dwell time of 4 µs/px, image size 512 x 512 px) to minimize image distortions due to specimen drift and scanning distortions and improve the signal-to-noise ratio.

3.2.6 Quantitative analysis of experimental STEM images

For quantitative analysis of experimental atomic-scale HAADF-STEM images, atomic column intensities were normalized by subtracting the detector background signal [220]. Then, the positions of atomic columns with subpixel accuracy were determined using 2D Gaussian fitting ("Gauss fit on spot" plugin, ImageJ). The local maxima in the images were determined using the "Find Maxima" algorithm in ImageJ, while pixel intensities of each atomic column were integrated within an approximated 2D Gaussian profile [221]. The mask size for the determination of atomic column intensity was set approximately at full width at half maximum (FWHM) of the atomic column intensity profile.

Simulations of HAADF-STEM images were carried out using quantitative image simulation software QSTEM with multislice method and frozen phonon approximation [222]. The following microscope parameters were used: acceleration voltage 200 kV, chromatic aberration Cc 1.1 mm, probe convergence semi-angle 24 mrad, annular detector angular range from 68 to 180 mrad, and energy spread dE = 0.4 eV. 30 phonon configurations at a temperature of 300 K were calculated with included thermal diffuse scattering (TDS), which causes inelastic phonon excitation.

Crystal models for image simulations were constructed based on the crystal structures of $Li_2La_2Ti_3O_{10}$ [92] and visualized using Vesta [223]. The starting model of the structure with thicknesses of 510.9 Å (35644 atoms) was prepared in XYZ format. The starting model was initially simulated in their original form. Further, the model was modified in terms of thickness, atomic column positions (*e.g.* relaxation across the RP-type defects), and composition to replicate the specific features observed in the experimental images. Models with different ion exchange rates in the atomic columns next to the RP-type defects and modified composition of layers in pseudo-perovskite block to match the $Li_{0.33}La_{0.56}TiO_3$ phase were prepared using Phyton code written by David Fabijan. The absolute intensities of the individual atomic columns in simulated HAADF images were determined using the same procedure as for the experimental images.

To determine lattice distortions and local strain, Geometric Phase Analysis (GPA) [224], [225] was performed in Digital Micrograph software.

3.2.7 Laser Ablation Inductively Coupled Plasma Mass Spectrometry (LA-ICP-MS)

The instrumental setup for LA-ICP-MS measurements was comprised of a laser ablation system (193 nm ArF* excimer; Analyte G2 Teledyne Photon Machines Inc., Bozeman, MT). The LA-system was equipped with a standard active two-volume ablation cell (HelEx II), including the Aerosol Rapid Introduction System (ARIS, Teledyne CETAC Technologies) for fast aerosol washout. The LA unit was coupled to a quadrupole ICP-MS instrument (Agilent 7900x, Agilent Technologies, Santa Clara, CA). Ablation parameters were as follows: laser energy density 3.0 J/cm^2; repetition rate 250 Hz; beam diameter 3 μm; dosage 10; and total acquisition time for ICP-MS acquisition 0.04 s (with corresponding dwell times for specific nuclides: ^{7}Li 15 ms; ^{47}Ti 8 ms; and ^{139}La, 8 ms). Other parameters were based on model predictions for the fastest possible mapping times, avoidance of aliasing, minimal blur, and maximal S/N ratios [188], [226]. The ablated material was transported from the ablation cell to the ICP using helium as a carrier gas and argon was added as a make-up gas before the torch of the ICP. Data processing and image analysis were performed using the software packages HDIP (Teledyne Photon Machines Inc., Bozeman, MT) and ImageJ. The LA-ICP-MS analyses were performed in collaboration with Dr. Martin Šala from the Department of Analytical Chemistry at the National Institute of Chemistry in Ljubljana, Slovenia.

3.2.8 First-principle calculations

First-principles computations based on density functional theory (DFT) [227] were used for thermodynamical phase stability evaluation and density of states computation. Perdue-Burke-Ernzerhof (PBE) Generalized Gradient Approximation (GGA) exchange-correlation [228] and Projector Augmented-Wave (PAW) pseudo-potential [229] implanted in Vienna Ab initio Simulation Package (VASP) [230], [231] were adopted for the first-principles computations. The LLTO models ($Li_3La_{11}Ti_{18}O_{54}$ and $Li_6La_{10}Ti_{18}O_{54}$) were built according to experimental XRD results [103], [232] and the Ti- and O-deficient LLTO atomic model was built by removing 1 Ti atom and 2 O atoms from $Li_{0.33}La_{0.56}TiO_3$. Atomic models of $Li_2La_2Ti_3O_{10}$ and stable compounds in the Li-La-Ti-O quaternary system were taken from the Materials Project database [233]. All of the computations were converged to 10^{-4} eV energy convergence and 10^{-2} eV/Å force convergence. The k-point meshes used for $Li_{0.167}La_{0.61}TiO_3$, $Li_{0.33}La_{0.56}TiO_3$, and Ti- and O-deficient $Li_{0.33}La_{0.56}TiO_3$ total energy and density of states computations were $2 \times 2 \times 3$ and $4 \times 4 \times 6$, respectively.

Phase stability evaluation was conducted by finding the most stable combination of compounds within the Li:La:Ti:O = 11:15:25:78 stoichiometry by calculating the decomposition energies of the main reaction products, including $Li_{0.167}La_{0.61}TiO_3$, $Li_{0.33}La_{0.56}TiO_3$, Ti- and O-deficient LLTO, and $Li_2La_2Ti_3O_{10}$, by Equation 9 [234]:

$$E^{decomposition} = n_0 E^{formation}_{main\ product} + \sum n_i E^{formation}_{compounds} \quad \text{(Eq. 9)},$$

where $E^{decomposition}$ is the decomposition energy; $E^{formation}_{main\ product}$ and $E^{formation}_{compounds}$ are the formation energies of main reaction products ($Li_{0.167}La_{0.61}TiO_3$, $Li_{0.33}La_{0.56}TiO_3$, Ti- and O-deficient $Li_{0.33}La_{0.56}TiO_3$, and $Li_2La_2Ti_3O_{10}$) and stable compounds in the Li-La-Ti-O quaternary system, respectively. n_0 and n_i are the coefficients of the compounds that can fulfill the stoichiometry (Li:La:Ti:O = 11:15:25:78). The first-principle calculations were carried out in collaboration with Prof. Dr. Shih-Kang Lin and Dr. Che-An Lin from the National Cheng Kung University, Tainan, Taiwan.

3.2.9 Ionic conductivity measurements

For ionic conductivity measurements, the Au electrodes were sputtered on both sides of ceramic pellets in a BAL-TEC SCD 005 sputter system with a sputtering current of 20 mA and a sputtering time of 300 s for each of the electrodes. The impedance spectra of the samples were measured with a Novocontrol Beta-N impedance analyzer (Montabaur, Germany) at room temperature (25 °C) in a frequency range from 10 Hz to 17 MHz by applying a voltage perturbation of 100 mV. The total ionic conductivity of each sample was estimated based on the Equation 10:

$$\sigma = \frac{d}{S \times R} \qquad \text{(Eq. 10)},$$

where σ (S/cm), R (ohm), d (cm), and S (cm^2) are the conductivity, resistance, thickness, and electrode area, respectively. Ionic conductivity measurements were performed in collaboration with Jan Žuntar from Jožef Stefan Institute, Ljubljana, Slovenia.

Chapter 4

Results and Discussion

4.1 Micro-Scale Characteristics of LLTO Ceramics with Variable La:Ti Ratios

LLTO samples with varying La:Ti ratios and different thermal treatments (sintering temperature and cooling regime) were characterized to investigate how the initial LLTO composition influences the densification behavior, crystallization, phase composition, and microstructure development.

The main goal of this part of the research was to determine whether it is possible to prepare coarse-grained LLTO ceramics with a reduced contribution of grain boundaries. The preparation approach is based on a concept that has been previously demonstrated in perovskite oxide ceramics [159], [166], [169], where triggering the formation of RP-type planar defects and sequences has a significant influence on microstructure development in perovskite-based ceramics. Grains in which RP-type defects nucleate exhibit exaggerated grain growth in the direction of the defects and these grains develop into large grains with plate-like morphology.

4.1.1 Densification kinetics

Densification kinetics of the samples with variable La:Ti ratio were studied with a heating-stage microscope to determine the optimal sintering temperature of calcined and homogenized LLTO powders. All samples start to densify at ~ 900 °C (Figure 4.1).

The sample with stoichiometric composition for the formation of LLTO (La:Ti=0.560) shows the steepest curve, indicating the fastest densification rate of all samples. Densification is strongly accelerated at 1030 °C and reaches the fastest densification rate at around 1100 °C. Fast shrinking of the sample continues until 1140 °C and is completed at 1200 °C. According to the Li_2O-TiO_2 phase diagram, this might indicate the formation of a liquid phase between Li-oxide and TiO_2 [235].

On the other hand, samples with increasing La:Ti ratio exhibit slower densification rates, and the temperature of accelerated shrinking is systematically shifted to higher temperatures. The onset of fastest densification for the La:Ti=0.622 sample occurs at ~100 °C higher temperature than in the stoichiometric composition. The densification process of the samples with higher La:Ti ratios is also completed at higher temperatures.

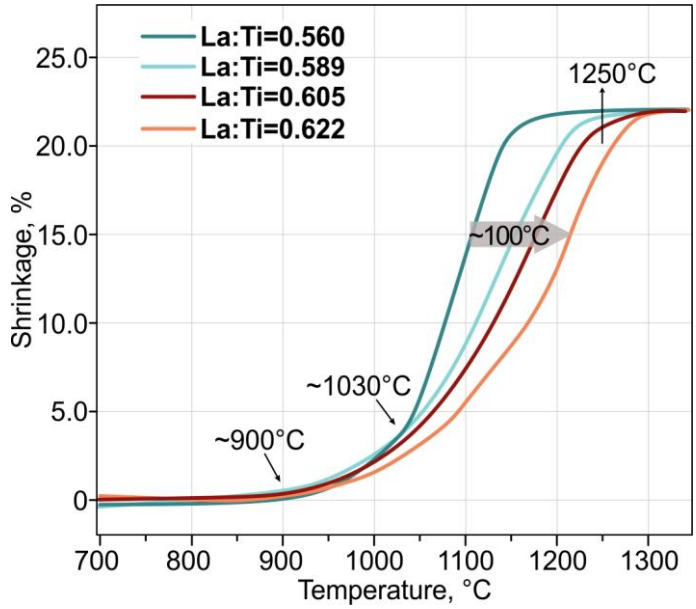

Figure 4.1: Densification curves of the samples with different nominal compositions showing the shift of the fastest shrinking rate to higher temperatures as a result of higher La_2O_3 additions.

Based on the densification kinetics, the optimal sintering temperature for the study of microstructure development in LLTO is above 1300 °C, where the samples reach their maximum density. High-density ceramics with lower fraction of grain boundaries, pores, and other types of defects is beneficial for ionic conductivity. It is also convenient for the preparation of samples (polished cross-sections) for microstructural characterization. In order to study the influence of temperature on the microstructural properties of the samples with different La:Ti ratios, we analyzed cross-sections after sintering at 1250 °C, just before the samples reached their final density, and after 1350 °C when the samples were fully densified as higher sintering temperatures enhance diffusion rates and promote further microstructure development. The sintering temperature is a critical factor in the synthesis of the LLTO system, as it significantly affects both the LLTO structure (modification) and its properties [236], [237].

4.1.2 Phase analysis

According to the XRD patterns, slowly-cooled samples after sintering at 1250 °C and 1350 °C crystallize in tetragonal β-LLTO (*P4/mmm*) modification (#01-087-0935), regardless of their La_2O_3 content (Figure 4.2a, b). In addition to tetragonal LLTO reflections, the XRD pattern of the sample with stoichiometric composition for the targeted $Li_{0.33}La_{0.56}TiO_3$ phase (La:Ti=0.560) contains reflections of TiO_2 rutile (ICSD #01-080-2531, marked with asterisks) and a weak reflection around 20° 2θ, indicating the presence of a small amount of $Li_2Ti_3O_7$ secondary phase (ICSD #00-034-0393, marked with rectangle) after sintering at 1250 °C. When sintered at 1350 °C, the majority of rutile reflections in this sample disappear, while the reflection from the $Li_2Ti_3O_7$ phase remains visible in the diffraction pattern. No secondary phases are observed in the samples with a higher La:Ti ratio.

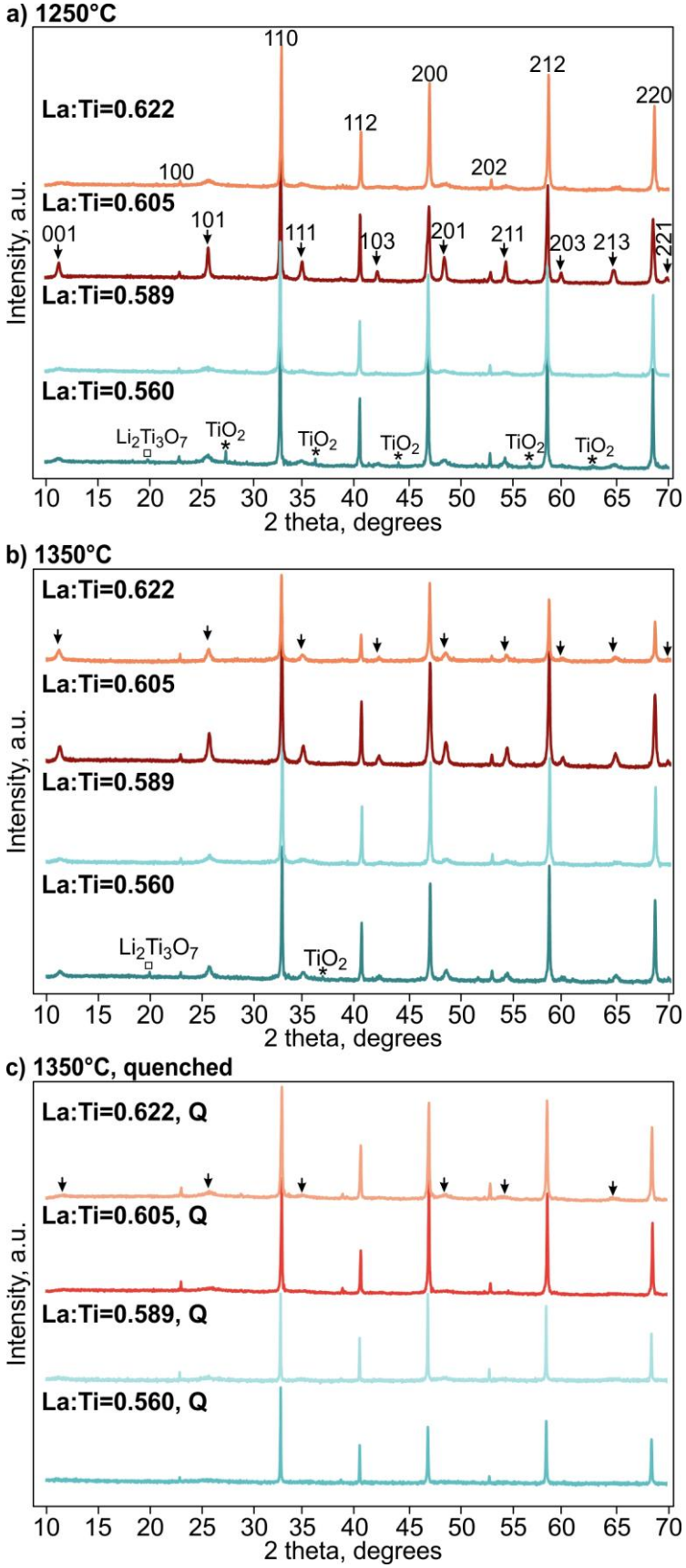

Figure 4.2: XRD patterns of LLTO ceramics with different La_2O_3 additions after sintering at (a) 1250 °C, (b) 1350 °C, and (c) quenched from 1350 °C.

The tetragonal β-LLTO modification is characterized by alternating La-rich and La-poor layers along the c-axis, which leads to the doubling of the unit cell in this direction [48], [236]. In the XRD pattern, this feature is reflected in the presence of superstructure reflections (marked with arrows in Figure 4.2) alongside reflections typical for perovskites with the ideal cubic symmetry, as indexed on the XRD spectra of La:Ti=0.622 sample sintered at 1250 °C. The most indicative reflection for the tetragonal LLTO modification with a doubled unit cell along the c-axis is the (001) reflection at 11° 2θ. In pseudocubic symmetry, this reflection would be indexed as {1/2,0,0} [89]. The intensity of the superstructure reflections varies greatly among the samples. The sample with a nominal La:Ti ratio of 0.605 exhibits the highest intensity of superstructure reflections, whereas in other samples, their intensity is comparatively weaker. The La:Ti=0.589 sample after sintering at 1250 °C shows the weakest superstructure reflections.

The XRD patterns of samples quenched from 1350 °C (Figure 4.2c) display sharp and intense reflections characteristic of pseudocubic LLTO. In the sample with La:Ti ratio of 0.622, some broad, low-intensity superstructure peaks are still present. This observation suggests that while quenching generally promotes the stabilization of cubic LLTO, the low-intensity superstructure peaks in the sample with a high La:Ti ratio may indicate the presence of small tetragonal domains within the cubic LLTO structure.

Since polycrystalline LLTO ceramics can consist of different LLTO modifications [106], [108], the (200) reflection and intensity ratio between (100) and (101) reflections were investigated in more detail. In orthorhombic LLTO modification, the (200) reflection shows characteristic splitting to three peaks due to the small differences in lattice parameters (a≠b≠c) [89], [102], [135]. However, in the synthesized samples, the (200) peaks are sharp and show only one maximum around 46.9° 2θ (d_{hkl}=0.194 nm), which is a typical value of the cubic or tetragonal modification (Figure 4.3). The slight shifts of the (200) reflections could be related to variations in the ratio between the cubic and tetragonal phases with different lattice parameters or may stem from instrumental error.

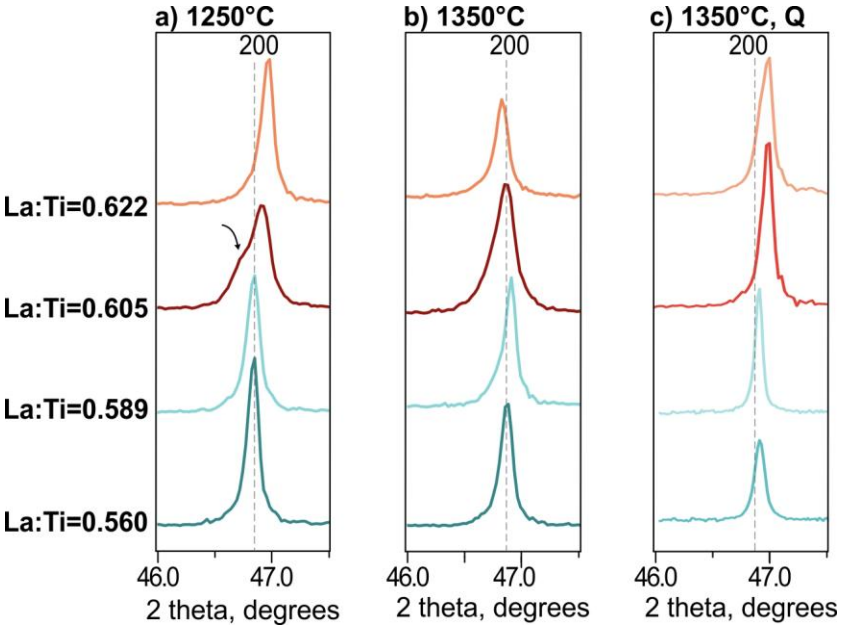

Figure 4.3: Sections of the XRD patterns that include (200) reflection for samples sintered at (a) 1250 °C, (b) 1350 °C, and (c) after quenching from 1350 °C.

The reflection from the La:Ti=0.605 sample after sintering at 1250 °C is broader and contains a shoulder peak at lower 2θ (marked by an arrow). A similar, though much weaker, shoulder peak is also observed in the quenched sample with La:Ti=0.622. This suggests the presence of another LLTO modification or phase structurally related to LLTO. After sintering of La:Ti=0.605 sample at 1350 °C, the (200) reflection becomes noticeably broader and asymmetric compared to other samples, but no additional reflection is observed.

Variable intensities of superstructure reflections in the XRD spectra indicate that the samples contain different fractions of cubic and tetragonal LLTO modifications. To estimate the relative volume fractions of both modifications, the intensity ratio between the cubic $I_{c(100)}$ at 22.9° 2θ and tetragonal $I_{t(101)}$ reflection at 25.7° 2θ was calculated (Figure 4.4) [128]. A higher value of the ratio suggests a greater proportion of the cubic phase, while a lower value indicates a predominant tetragonal modification or the presence of large tetragonal domains. Samples sintered at 1250 °C (represented by full circles) typically exhibit lower tetragonality than the samples after sintering at 1350 °C (represented by open circles), except for the sample La:Ti=0.605, where the amount of tetragonal phase is slightly higher after sintering at 1250 °C. Overall, the La:Ti=0.605 sample contains the highest fraction of the tetragonal phase. The sample with the highest La:Ti ratio of 0.622 sintered at 1250 °C has the highest fraction of the cubic phase among all samples but exhibits a large increase in the amount of tetragonal phase after sintering at 1350 °C.

As assumed from the broad and small superstructure peaks in the quenched samples, the calculated $I_{(100)}/I_{(101)}$ ratios reach much higher values in comparison to the slowly-cooled samples, which confirms that these samples mainly contain cubic LLTO modification.

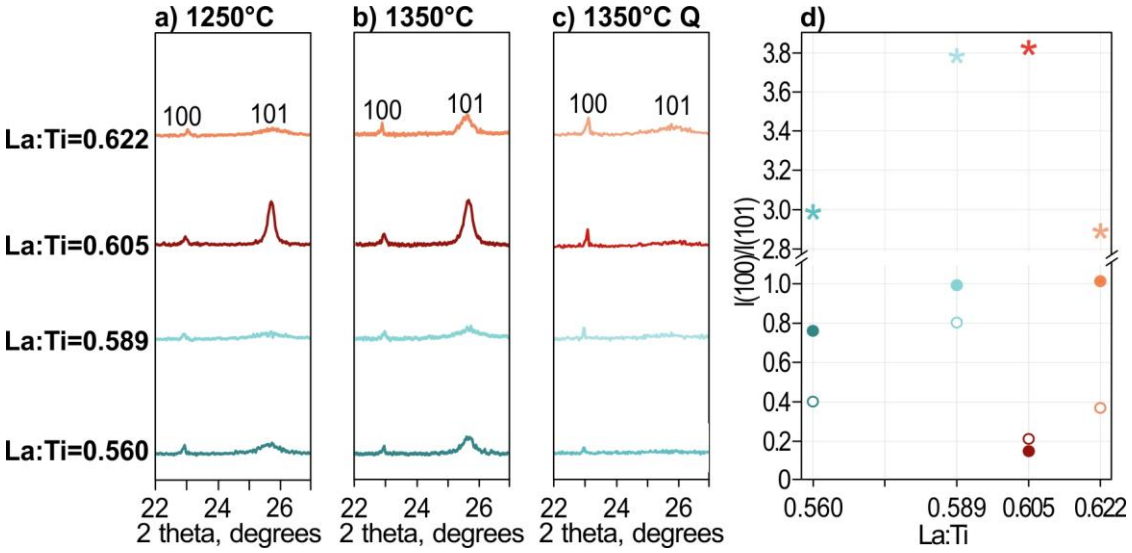

Figure 4.4: Cubic (100) and tetragonal (101) reflections for samples sintered at (a) 1250 °C, (b) 1350 °C, and (c) after quenching from 1350 °C. (d) Calculated intensity ratio between the cubic and tetragonal $I_{(100)}/I_{(101)}$ reflections in the samples with different La:Ti ratios after sintering at 1250 °C (full circles) and 1350 °C (open circles) and after quenching (asterisks).

4.1.3 Microstructural characteristics

According to XRD analysis, all LLTO samples, regardless of their La:Ti ratios, consist of predominantly pseudocubic and tetragonal LLTO modification, only the stoichiometric LLTO sample contains some Ti-rich secondary phases. In contrast, SEM analyses reveal a remarkable effect of the starting LLTO composition on the microstructure. The microstructural characteristics of the samples, after sintering at 1250 °C and 1350 °C were characterized on thermally etched cross-sections. Compositional analysis of the LLTO samples was performed using EDS on polished, unetched cross-sections. Since Li has an atomic number too low to be detected by SEM/EDS, La:Ti ratio was used to estimate the composition of LLTO grains (x-value in $Li_{3x}La_{2/3-x}\square_{1/3-2x}TiO_3$).

To ensure reliable determination of the La:Ti ratio, EDS was beforehand validated using a reference sample of $La_2Ti_2O_7$ with a La:Ti ratio of 1:1. This reference sample was prepared by a standard ceramic synthesis procedure, and its single-phase composition was determined by XRD (ICSD #04-005-9141) (Figure 4.5a). SEM/EDS analyses of a polished cross-section of the $La_2Ti_2O_7$ sample (Figure 4.5b) confirmed the single-phase composition and homogeneous microstructure with darker regions corresponding to porosity. It consistently showed a La:Ti ratio close to 1:1, demonstrating that SEM/EDS is suitable for determining the La:Ti ratio in the LLTO samples.

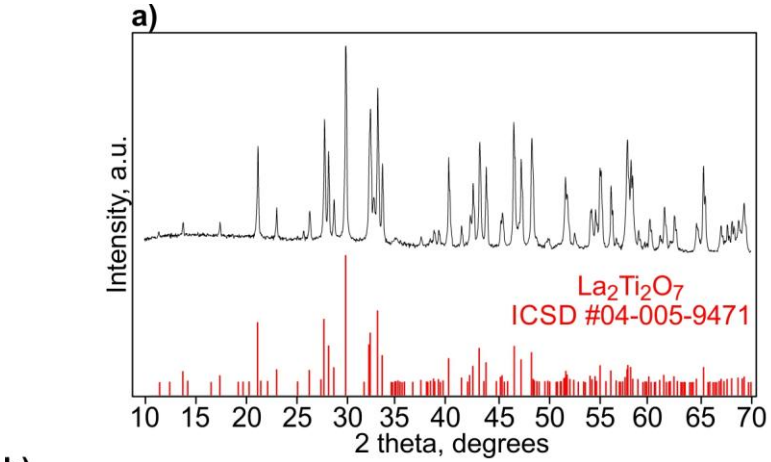

b)

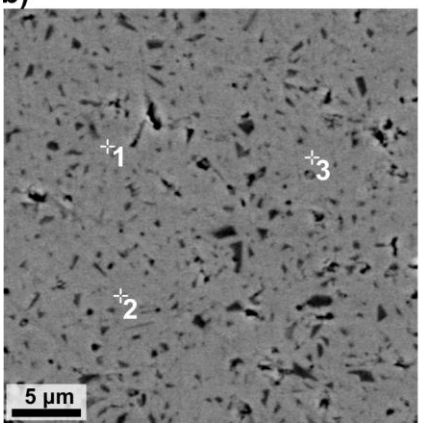

Spectrum	1	2	3
Ti (at%)	50.1	49.8	49.5
La (at%)	49.9	50.2	50.5
La:Ti	1.00	1.01	1.02
average La:Ti	**1.01 ± 0.01**		

Figure 4.5: (a) XRD pattern of the $La_2Ti_2O_7$ sample, matched with corresponding ICSD card. (b) SEM backscattered electron (BSE) image displaying homogeneous microstructure, along with a table presenting the results of EDS analysis.

4.1.3.1 Microstructural characteristics after sintering at 1250 °C

The sample with stoichiometric starting composition for the synthesis of $Li_{0.33}La_{0.56}\square_{0.11}TiO_3$ (La:Ti=0.560) after sintering at 1250 °C consists of uniformly distributed small LLTO grains with sizes up to ~5 µm (Figure 4.6a). Such microstructure is commonly reported in the literature for LLTO synthesized through conventional sintering methods [238], [239], [240]. Most of the LLTO grains develop cube-like morphology, with the grains enclosed by {100} facets.

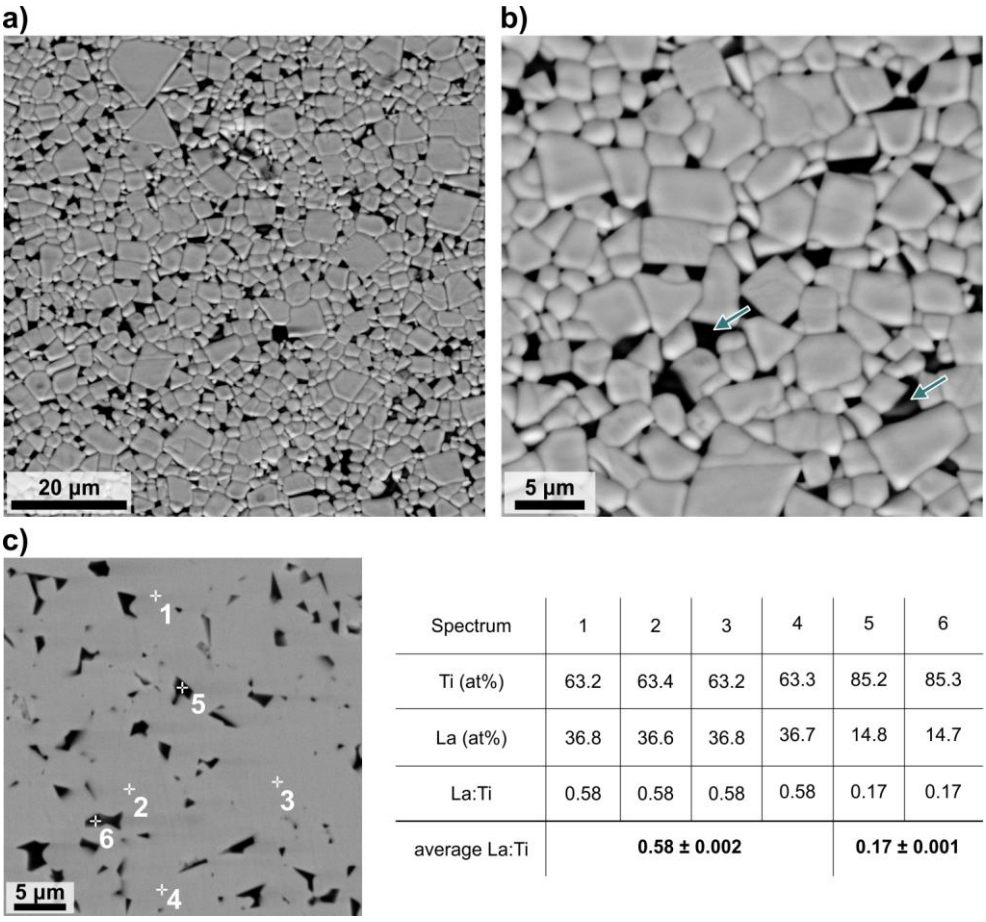

Spectrum	1	2	3	4	5	6
Ti (at%)	63.2	63.4	63.2	63.3	85.2	85.3
La (at%)	36.8	36.6	36.8	36.7	14.8	14.7
La:Ti	0.58	0.58	0.58	0.58	0.17	0.17
average La:Ti	**0.58 ± 0.002**				**0.17 ± 0.001**	

Figure 4.6: (a,b) Microstructure of stoichiometric LLTO (La:Ti=0.560) after sintering at 1250 °C. (c) SEM/EDS analysis of the unetched cross-section.

In backscattered SEM images, the grains exhibit brighter contrast, whereas the regions between the grains are dark, as indicated by blue arrows in Figure 4.6b. While some of these darker regions are porosity, SEM/EDS analysis on an unetched cross-section reveals an increased amount of Ti in most of these regions (Figure 4.6c). This is consistent with the XRD results, where Ti-rich secondary phases were detected. The LLTO grains show a slightly higher La:Ti ratio of around 0.58 in comparison to the nominal composition with La:Ti=0.56. This increase is attributed to the incorporation of TiO_2 into secondary phases, and consequently, less TiO_2 is left for the formation of LLTO, resulting in the formation of LLTO grains with a higher La:Ti ratio.

Faceted LLTO grains were also observed using transmission electron microscopy. The selected area diffraction (SAED) pattern confirms that the grains, oriented along [001] zone axis are enclosed by {100} facets (Figure 4.7).

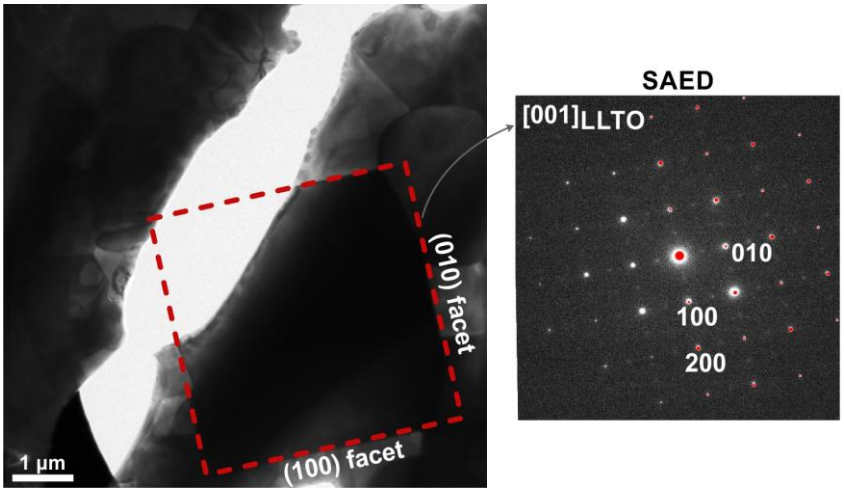

Figure 4.7: TEM image of LLTO grain in the sample with La:Ti=0.560 exhibiting square cross-section. The calculated diffraction pattern of LLTO is superimposed in the right half of the diffraction pattern with the main reflections indexed.

The sample with La:Ti=0.589 has a comparable grain size and morphology to the stoichiometric sample (La:Ti=0.560) (Figure 4.8a,b). The difference between these two samples is the tighter packing of LLTO grains in the sample with a higher La:Ti ratio, which can be attributed to the lower amount of secondary phases.

The presence of secondary phases was not detected by XRD but is visible on SEM/EDS images and maps, where small grains between matrix LLTO grains are enriched with Ti (Figure 4.8c). The lower amount of Ti-rich phases is expected to enhance the Li-ion transport properties. In this sample, the La:Ti ratio is close to the value in the starting powder, corresponding to LLTO with x=0.09.

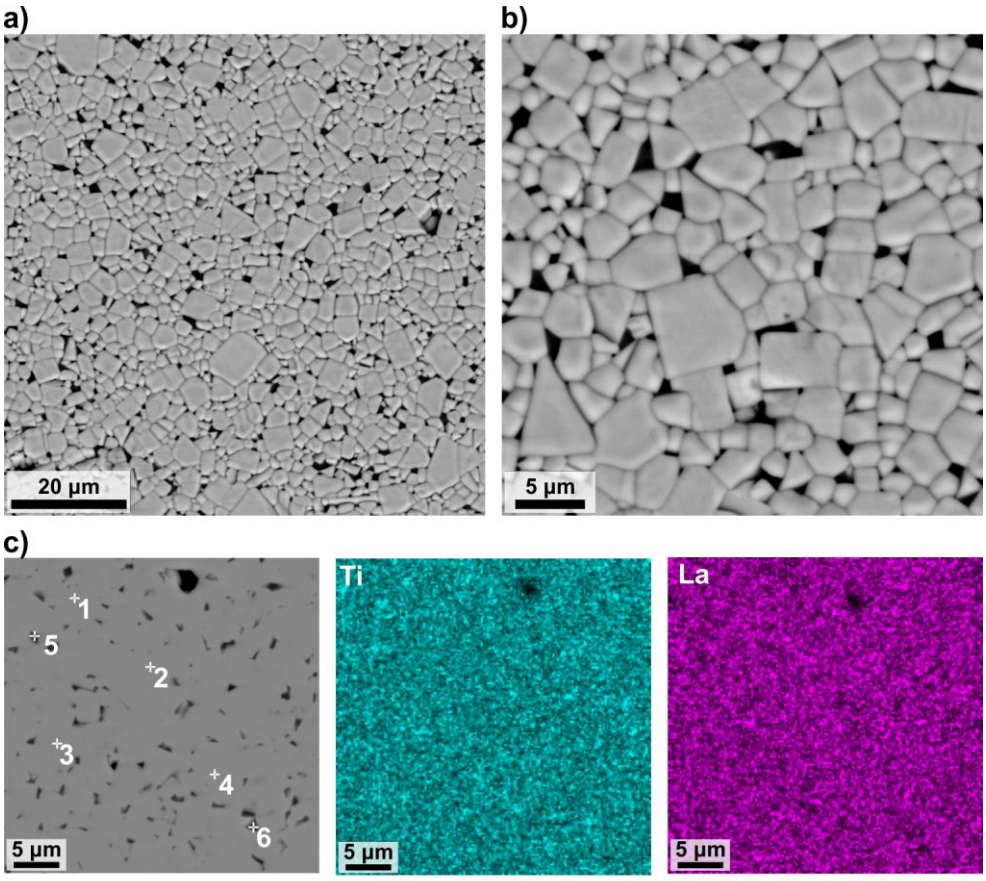

Spectrum	1	2	3	4	5	6
Ti (at%)	63.5	63.7	62.9	63.4	79.7	79.8
La (at%)	36.5	37.3	37.1	36.6	20.3	20.2
La:Ti	0.58	0.59	0.59	0.57	0.25	0.25
average La:Ti	**0.58 ± 0.008**				**0.25 ± 0.001**	

Figure 4.8: (a,b) Microstructure of LLTO sample with initial La:Ti ratio of 0.589 after sintering at 1250 °C. (c) SEM/EDS analysis shows a slightly lower La:Ti ratio compared to the nominal composition.

A further increase in the La:Ti ratio in the starting composition significantly affects the LLTO grain growth and microstructure development. The sample with La:Ti ratio 0.605 exhibits a bimodal microstructure which is composed of larger grains embedded in the matrix of smaller grains (Figure 4.9a). Most of the large grains exhibit anisotropic morphology with thicknesses up to around 10 µm and lengths exceeding 100 µm. Some of them are isometric, which implies their plate-like morphology (indicated by red arrows in Figure 4.9b). The fast-growing large plate-like grains show characteristics of preferential and exaggerated growth [165], [166] and sometimes intrude other large grains. The surrounding smaller grains have a more isometric morphology and measure below 10 µm. Both large and small grains are intersected by an internal boundary, which occurs as a thinner or thicker lamella with a slightly brighter contrast than the grains in the backscattered SEM images (marked with white arrows in Figure 4.9c). The lamellae inside LLTO grains can either intersect or run parallel to each other in sequence.

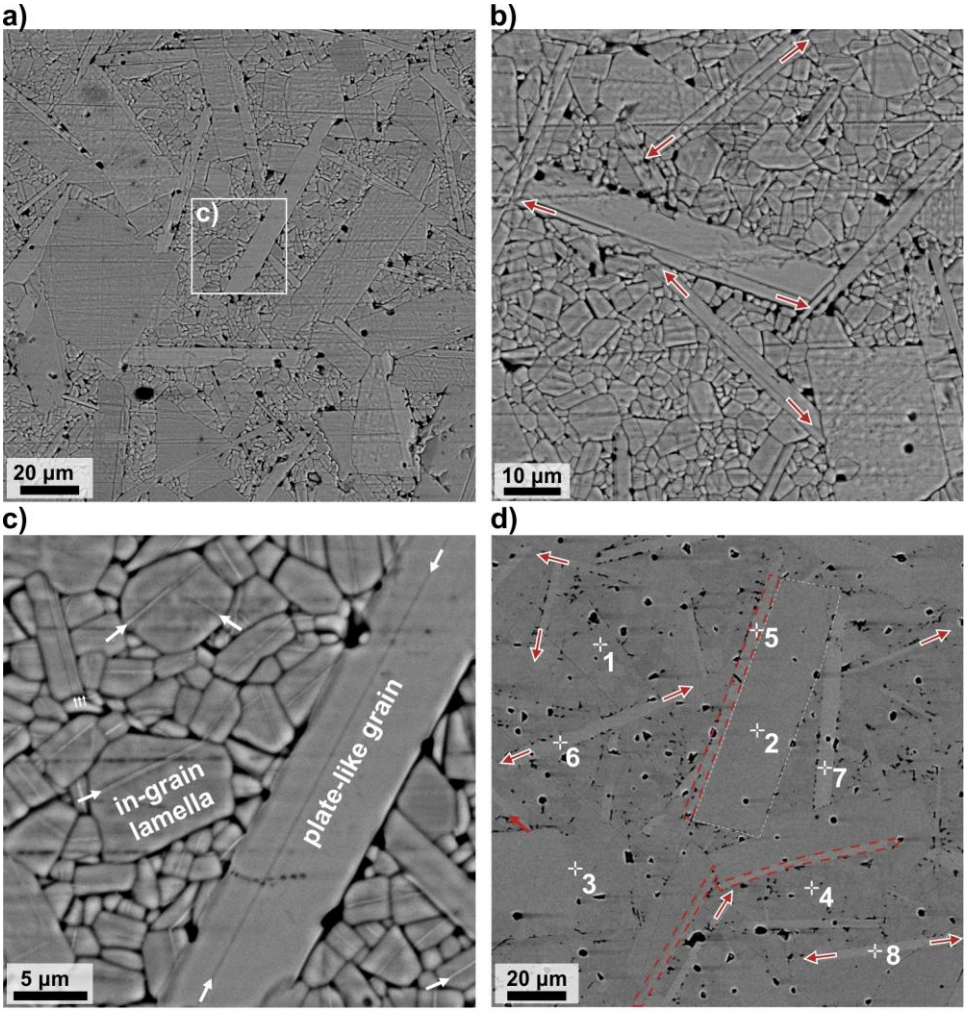

Spectrum	1	2	3	4	5	6	7	8
Ti (at%)	62.8	63.4	63.6	63.1	59.6	59.9	60.3	60.1
La (at%)	37.2	36.6	36.4	36.9	40.4	40.1	39.7	39.9
La:Ti	0.59	0.58	0.57	0.58	0.67	0.67	0.66	0.66
average La:Ti	**0.58 ± 0.008**				**0.67 ± 0.005**			

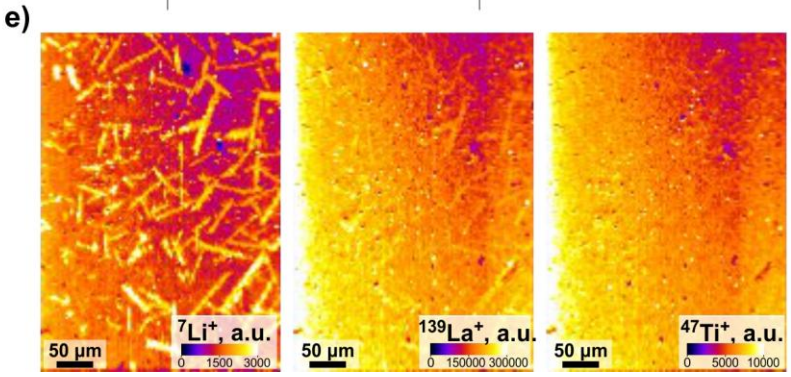

Figure 4.9: (a,b) Plate-like grains embedded in the matrix of smaller grains in sample La:Ti=0.605 after sintering at 1250 °C. (c) All grains are intersected by an internal boundary. (d) In an unetched cross-section, the plate-like grains and smaller LLTO grains have different contrasts due to different compositions, as determined by SEM/EDS. (e) LA-ICP-MS maps showing enrichment of Li and La in plate-like grains.

In backscattered images of the non-etched cross-section of the sample with La:Ti=0.605 after sintering at 1250 °C, some of the large plate-like grains show a brighter contrast than the surrounding grains. This implies that these grains have a composition with a higher average atomic weight. These brighter plate-like grains are occasionally in tight contact with larger grains having darker contrast (lower average atomic weight). Examples of such grains are indicated with a dashed red line in Figure 4.9d. The latter appear to be epitaxial, however, the use of diffraction techniques like EBSD would be required to confirm this. SEM/EDS analysis showed that the plate-like grains have a higher La:Ti ratio of around 0.67. In contrast, the smaller matrix LLTO grains have a La:Ti ratio of about 0.58, which corresponds to the LLTO perovskite with an x-value of around 0.09.

In order to check the elemental distribution in this sample, further analysis was performed with laser ablation inductively coupled plasma mass spectrometry (LA-ICP-MS) (Figure 4.9e). The results of this analysis showed a significantly higher concentration of Li and La within the plate-like grains compared to the surrounding LLTO grains. The higher Li and La concentrations in the plate-like grains suggest preferential incorporation of these elements in anisotropic grains. Their size, especially their length, implies that this process occurs in the early stage of the microstructure development and indicates the presence of another secondary phase with a slightly different composition in comparison to the LLTO.

The sample with the highest La:Ti ratio of 0.622 sintered at 1250 °C also exhibits a distinct bimodal microstructure (Figure 4.10a). It consists of around ~25 µm large LLTO grains with less elongated morphology surrounded by smaller LLTO grains; however, the presence of planar defects is not observed. In backscattered SEM images, the microstructure appears homogeneous without any secondary phases (Figure 4.10b). The La:Ti ratio determined by SEM/EDS is lower than expected as the nominal La:Ti value is 0.622, however, this was not investigated in detail.

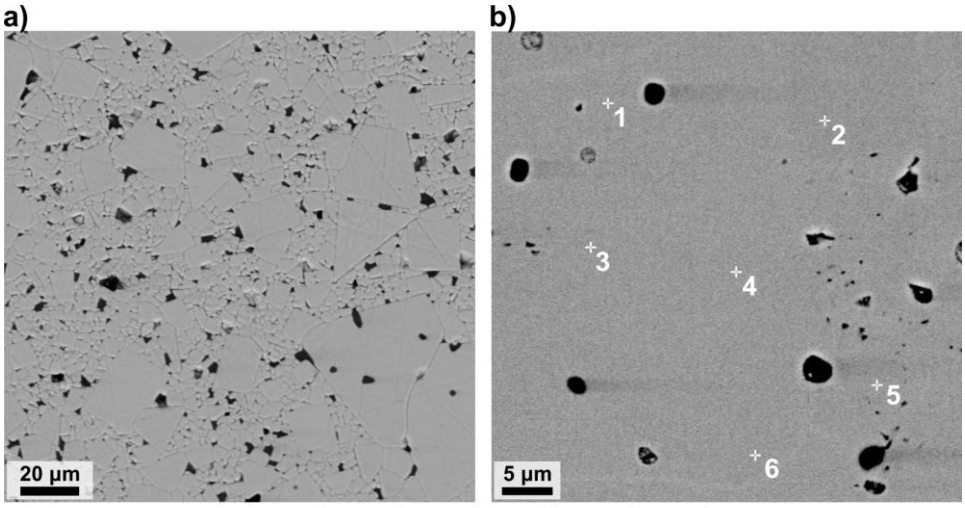

Spectrum	1	2	3	4	5	6
Ti (at%)	63.5	62.8	63.3	63.0	63.5	63.0
La (at%)	36.5	37.2	36.7	37.0	36.5	37.0
La:Ti	0.58	0.59	0.58	0.59	0.57	0.59
average La:Ti	**0.58 ± 0.007**					

Figure 4.10: (a) Bimodal microstructure of the sample with La:Ti=0.622. (b) Results of SEM/EDS analysis show a lower La:Ti ratio than expected.

4.1.3.2 Microstructures after sintering at 1350 °C

After sintering at 1350 °C, the microstructure of stoichiometric samples with La:Ti=0.560 and sample La:Ti=0.589 are comparable with those after sintering at 1250 °C, only with a slight increase in grain size to around 10-15 µm (Figure 4.11a, b). The sample with a higher addition of La_2O_3 (La:Ti=0.589) shows a denser packing of LLTO grains in comparison to the sample with stoichiometric starting composition. Both samples have a La:Ti ratio of 0.58 and still contain some Ti-rich secondary phases.

On the other hand, the microstructures of samples with La:Ti ratios of 0.605 and 0.622 transform from a distinctly bimodal distribution composed of large grains embedded in the matrix of smaller grains to a uniform and dense microstructure composed of large grains (Figure 4.12a, b). Elongated grains and planar defects in the sample with La:Ti=0.605 are no longer observed. LLTO grains exhibit irregular morphology and measure up to 100 µm in diameter. Large grains contain many intragranular pores, that form due to the fast grain growth and partially due to Li evaporation during a high-temperature sintering. A microstructure with such large grains has not been reported in LLTO ceramics prepared by solid-state sintering. In principle, coarse-grained LLTO ceramics with lower content of grain boundaries should exhibit higher total ionic conductivity, as the contribution of resistive grain boundaries is significantly reduced.

a) La:Ti=0.560

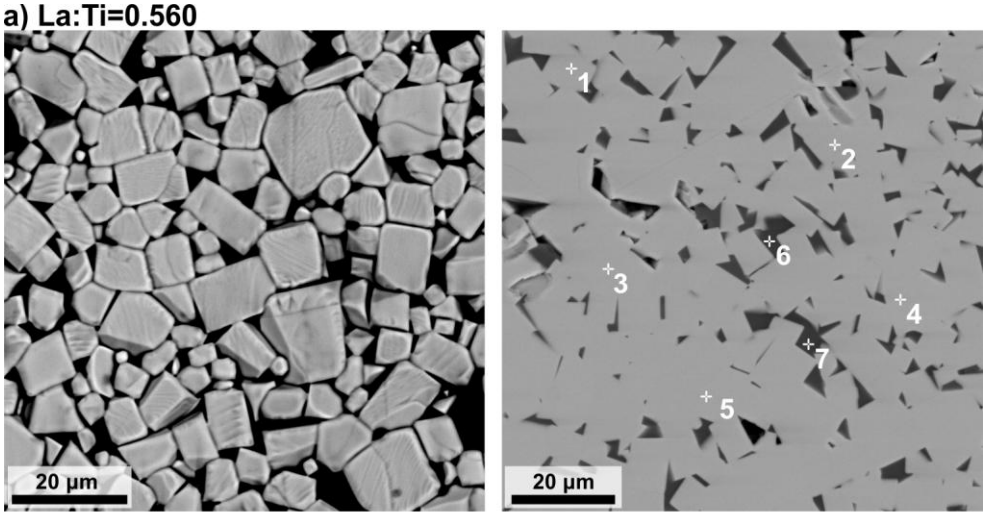

Spectrum	1	2	3	4	5	6	7
Ti (at%)	63.5	63.4	63.3	63.3	63.1	98.9	97.8
La (at%)	36.5	36.6	36.7	36.7	36.9	1.1	2.2
La:Ti	0.58	0.58	0.58	0.58	0.58	0.01	0.02
average La:Ti	**0.58 ± 0.007**					**0.02 ± 0.008**	

b) La:Ti=0.589

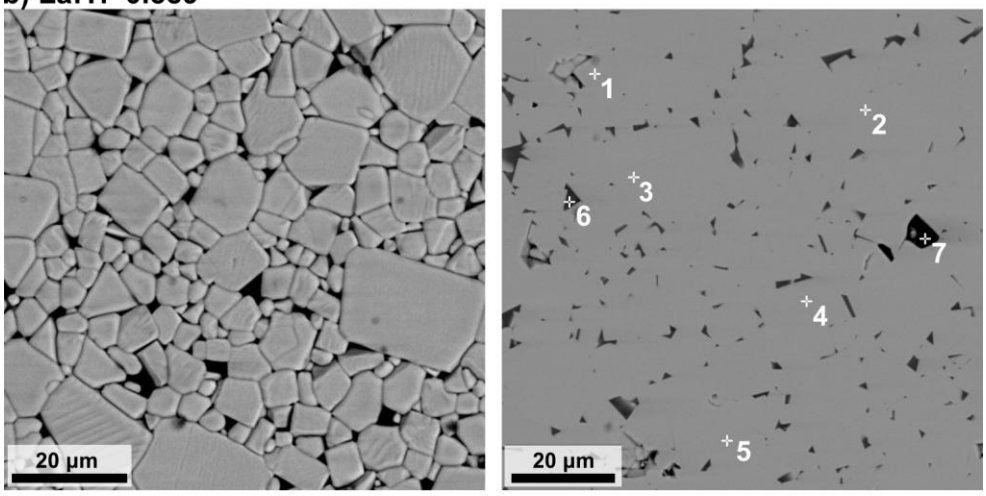

Spectrum	1	2	3	4	5	6	7
Ti (at%)	63.4	63.4	63.5	63.2	63.6	97.7	96.1
La (at%)	36.6	36.6	36.5	36.8	36.4	2.3	3.9
La:Ti	0.58	0.58	0.58	0.58	0.57	0.02	0.04
average La:Ti	**0.58 ± 0.004**					**0.03 ± 0.012**	

Figure 4.11: Etched (left) and unetched (right) cross-sections for SEM/EDS analysis of the samples with La:Ti ratio of (a) 0.560 and (b) 0.589 after sintering at 1350 °C.

a) La:Ti=0.605

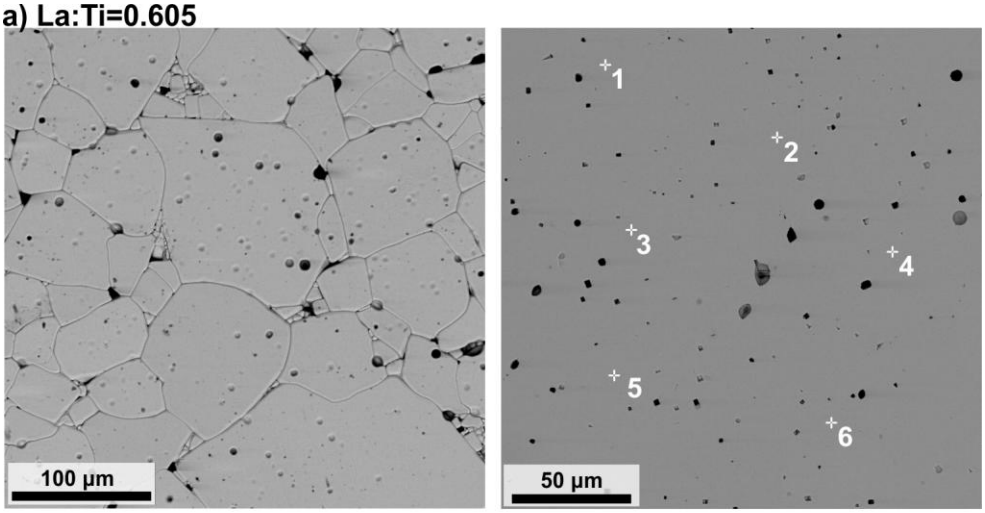

Spectrum	1	2	3	4	5	6
Ti (at%)	62.2	62.3	62.5	62.0	62.5	62.6
La (at%)	37.8	37.7	37.5	38.0	37.5	37.4
La:Ti	0.61	0.60	0.60	0.61	0.60	0.60
average La:Ti	**0.60 ± 0.005**					

b) La:Ti=0.622

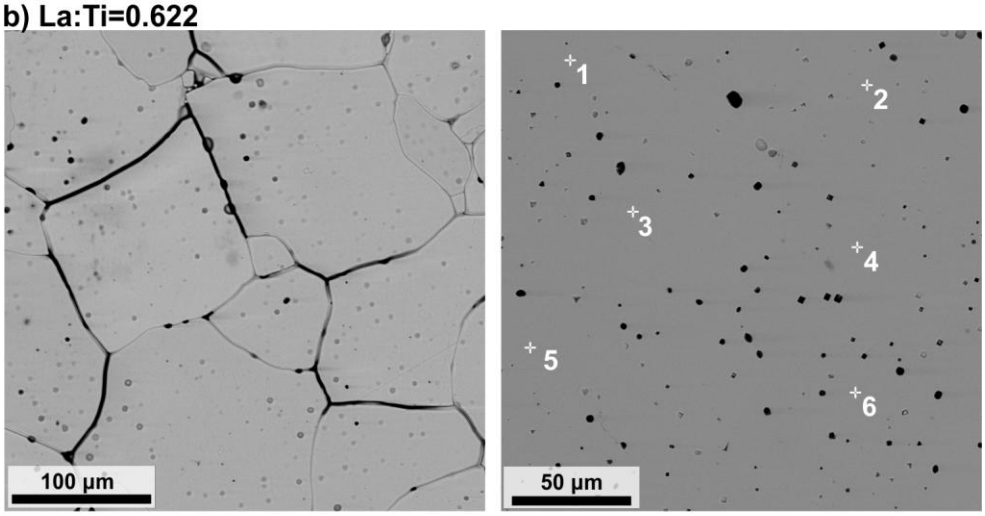

Spectrum	1	2	3	4	5	6
Ti (at%)	62.9	63.2	63.0	63.3	63.3	62.7
La (at%)	37.1	36.8	37.0	36.7	36.7	37.3
La:Ti	0.59	0.58	0.59	0.58	0.58	0.59
average La:Ti	**0.58 ± 0.006**					

Figure 4.12: Etched (left) and unetched (right) cross-sections for SEM/EDS analysis of the samples with La:Ti ratio of (a) 0.605 and (b) 0.622 after sintering at 1350 °C.

According to the LA-ICP-MS analysis that was performed on a polished cross-section of the sample with La:Ti=0.605 sintered at 1350 °C, the distribution of Li, La, and Ti is homogeneous with few indications of Li enrichment at the grain boundaries (Figure 4.13). The larger-scale color differences in the direction from left to right are present due to uneven sample height rather than compositional differences.

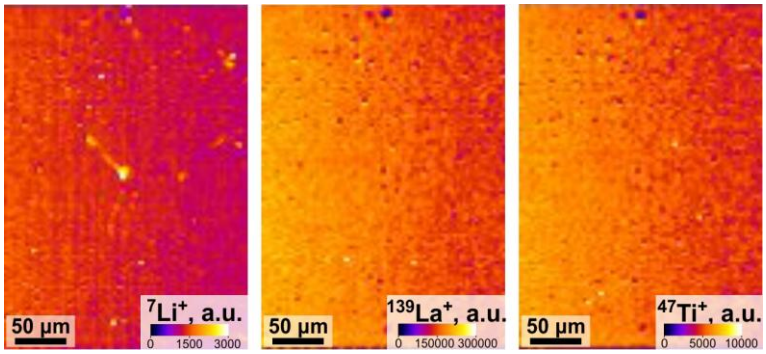

Figure 4.13: LA-ICP-MS maps of the sample with La:Ti=0.605 sintered at 1350 °C showing a homogeneous distribution of Li, La, and Ti.

The ratio between La and Ti in the samples after sintering at 1350 °C determined by EDS is presented in Figure 4.14. The La:Ti ratio ranges from 0.58 to 0.60, and is close to the theoretical values for the samples with La:Ti 0.589 and 0.605, while deviates from the expected ratios for the samples with La:Ti ratio of 0.560 and 0.622. The high ratio in the sample with initial La:Ti=0.560 could stem from the presence of Ti-rich secondary phases. In the sample with the highest La:Ti ratio (La:Ti=0.622), the calculated ratio is significantly lower than expected.

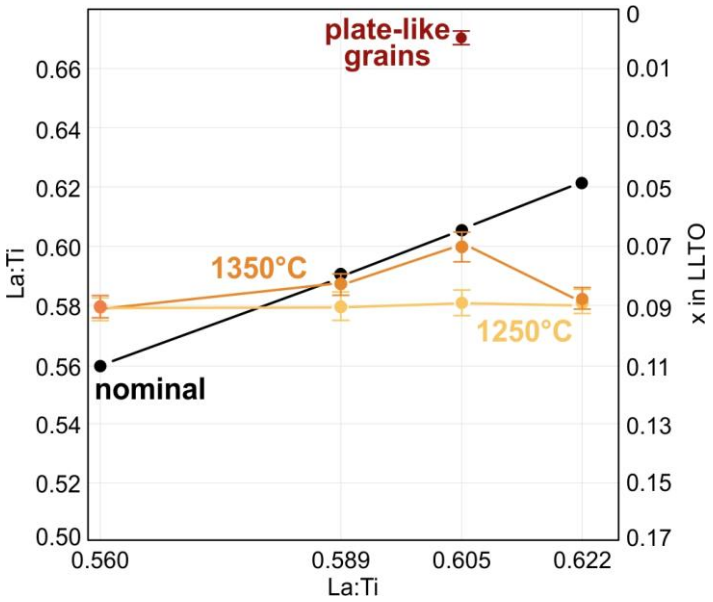

Figure 4.14: La:Ti ratio of LLTO grains in samples with different starting (nominal) La:Ti ratios (black) after sintering at 1250 °C (yellow) and 1350 °C (orange) as determined by SEM/EDS.

4.1.4 Density measurements

The microstructural characteristics of the samples after sintering at 1350 °C are reflected also in their absolute densities (Table 4.1). In general, the absolute densities of the samples increase with a higher La:Ti ratio.

Table 4.1: Absolute densities of the samples with different starting compositions after sintering at 1350 °C and densities relative to theoretical densities of α-LLTO (x=0.11) and β-LLTO (x=0.11).

Sample name	Absolute density (g/cm³)	Relative densities	
		α-LLTO; 4.840 g/cm³ (%)	β-LLTO; 5.004 g/cm³ (%)
La:Ti=0.560	4.516	93.3	90.2
La:Ti=0.589	4.690	96.9	93.7
La:Ti=0.605	4.809	99.4	96.1
La:Ti=0.622	4.812	99.4	96.2

In the samples La:Ti=0.560 and La:Ti=0.589, the smaller grains are loosely packed, which leads to a high fraction of intergranular porosity and thus lower density. A significant increase in density is observed in the samples that contain tightly packed large LLTO grains. The samples with La:Ti=0.605 and La:Ti=0.622 reach densities above 95% relative to the theoretical densities of α-LLTO (x=0.11) and β-LLTO (x=0.11). Since the samples contain different fractions of both modifications, the real values of the relative densities are probably between both values. Samples La:Ti=0.605 and La:Ti=0.622 with large exaggeratedly grown grains also contain intragranular pores. Such pores are indicators of the rapid coarsening of LLTO grains due to the exaggerated grain growth in the initial stages of microstructure development. During the fast growth, the larger grains consume not only the surrounding smaller grains but overgrow also the pores between them. Intragranular pores remain trapped inside the large grains [156], [241] and their elimination is difficult due to the slow oxygen lattice diffusion, which prevents the pores from being transferred to the grain boundaries.

4.1.5 Conclusions

The main findings of the first part of the study are:

- thermal treatment influences the LLTO structure; slow cooling stabilizes tetragonal LLTO while quenching from high temperatures stabilizes cubic LLTO,
- a higher La:Ti ratio in the initial LLTO composition shifts the densification to higher temperatures,
- microstructure of samples with La:Ti ratios of 0.560 and 0.589 are composed of LLTO grains with uniform grain size and contain Ti-rich secondary phases,
- sufficient La and Li excess in LLTO with La:Ti=0.605 triggers the exaggerated growth of plate-like grains in the early stages of sintering,
- plate-like grains with lengths up to 100 µm have a higher La:Ti ratio than surrounding matrix LLTO grains and are enriched with Li,
- in LLTO with La:Ti ratio of 0.605 all grains are intersected by a lamella(e),
- after sintering at 1350 °C, samples with La:Ti ratio higher than 0.6 consist of very large grains without defects and homogeneous distribution of Li, La, and Ti.

4.2 Atomic-Scale Analysis of LLTO with La:Ti Ratio of 0.605

This chapter is dedicated to the atomic-scale analysis of plate-like grains and lamellae that have been shown to have a significant effect on the microstructure development of LLTO ceramics with La:Ti ratio of 0.605. To understand the influence of planar defects on grain growth of LLTO-based solid electrolyte and obtain a detailed perspective into the reasons for their early formation and their transient nature at higher temperatures, the La:Ti=0.605 sample after sintering at 1250 °C was analyzed down to the atomic scale using STEM.

4.2.1 Low magnification STEM analysis

Figure 4.15 shows low-magnification BF-STEM images of thinned parts of two plate-like grains with an almost perfectly periodic layered structure that extends across the whole thickness of the grain. Occasionally, the periodicity of these grains is interrupted by up to 40 nm thick homogeneous segments. Plate-like grains are terminated by parallel facets and exhibit sharp contacts with neighboring grains. Some occur as individual grains, while others are in epitaxial contact with LLTO perovskite. Based on the FFT patterns, calculated from the areas of the layered phase, the grains in Figures 4.15a and 4.15b are oriented along two different zone axes, and measurements of the d-values were used to identify the crystal phase.

Figure 4.15a shows a situation, where, according to the diffraction analysis, a plate-like grain with a layered structure has an epitaxial orientation relationship with the upper neighboring LLTO grain, whereas no orientation relationship with the lower LLTO grain was observed. This situation can be linked to the observations with SEM, where long anisotropic grains with La:Ti ratio of 0.67 are in tight contact with LLTO with La:Ti ratio of 0.58 (Figure 4.9).

Figure 4.15b shows another plate-like grain with a periodic layered structure oriented along a different zone axis. It can be observed that in these grains, their almost perfect periodicity is occasionally interrupted. Nevertheless, the FFT pattern calculated from a high-resolution HAADF-STEM image yields distinct diffraction spots and the d-values are also included in Table 4.2.

The FFT pattern of LLTO grain in epitaxial contact with plate-like grain reveals that it is tetragonal β-LLTO oriented along [100] zone axis (upper FFT pattern in Figure 4.15a). Tetragonal LLTO modification is characterized by additional reflections in the [001] direction (the (001) reflection), indicative of the doubling of the unit cell in this direction. This is also evident from the HAADF image, where atomic layers with higher and lower intensity, that correspond to La-rich and La-poor layers, are interchanging. The FFT pattern of the plate-like grain with a layered structure (lower FFT pattern in Figure 4.15a) shows structural coherency with LLTO, which enables the formation of epitaxial contact.

D-values of diffraction spots in the FFT pattern calculated from the lamellae with the layered structure were measured and the results are given in Table 4.2. The analysis of d-values of diffraction spots has shown that they correspond to the $Li_2La_2Ti_3O_{10}$ phase (CIF #082907), oriented along [100] and [110] directions, respectively.

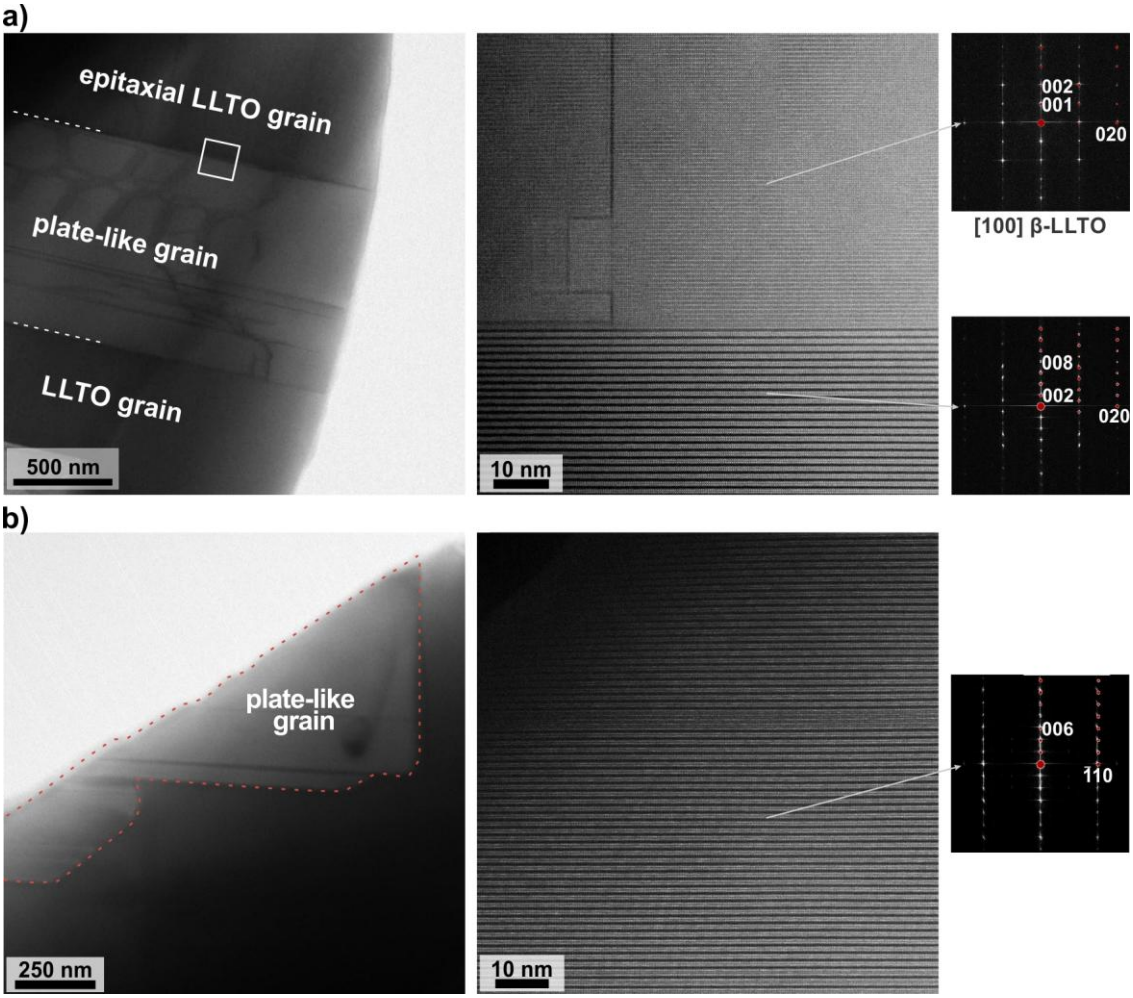

Figure 4.15: (a) Plate-like grain with layered structure showing sharp contacts with the neighboring grains. Magnified image of the epitaxial contact between the plate-like grain with layered structure and neighboring LLTO with FFT patterns from both phases. (b) BF-STEM image of a larger plate-like grain with layered structure ordered in thicker periodic sequences. The measured d-values are given in Table 4.2.

Table 4.2: Measured d-values of diffraction spots observed in FFT patterns calculated from grains with layered structure shown in Figure 4.15. A comparison to theoretical values for different (hkl) planes of the $Li_2La_2Ti_3O_{10}$ phase is given.

Figure	Measured d-value (Å)	Theoretical value (Å)	(hkl) of $Li_2La_2Ti_3O_{10}$	Zone axis
4.15a	13.108	13.280	002	[100]
	6.552	6.640	004	
	3.333	3.320	008	
	1.900	1.921	020	
4.15b	4.419	4.427	006	[110]
	2.714	2.716	$\bar{1}10$	

In contrast to the plate-like grains with nearly perfectly periodic layered structures, the smaller LLTO grains contain sequences of parallel defects in the form of thinner in-grain lamellae (Figure 4.16a). The lamellae inside the LLTO grains also exhibit characteristics of exaggerated grain growth and sometimes penetrate deeply into the neighboring grains, indicating faster growth in comparison to their matrix LLTO grain (inset in Figure 4.16a). They are typically composed of non-periodically arranged parallel defects (Figure 4.16b). The LLTO matrix next to the sequences of planar defects occasionally contains single defects along the equivalent {100} directions, often forming closed loops. These defects have the highest density right next to the in-grain lamellae.

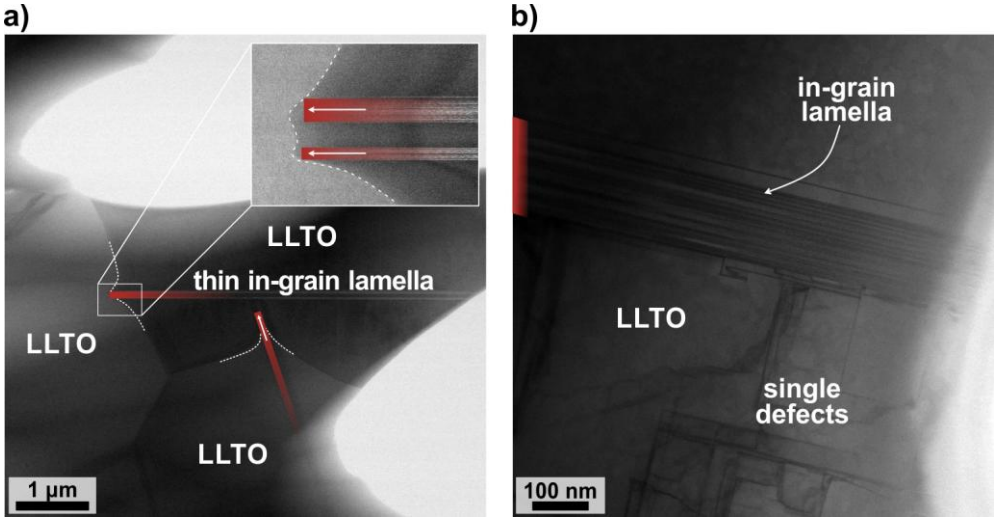

Figure 4.16: (a) Thin lamellae in LLTO grain sometimes penetrate the adjacent LLTO grains. (b) In-grain lamellae with non-periodic structure.

Quantitative analysis of periodic and non-periodic sequences of planar defects will be presented in the following sections. The analyses will provide a deeper understanding of their structural characteristics and will help to understand the influence of these defects on specific microstructure development of the LLTO ceramics with an initial La:Ti ratio of 0.605 and excess Li addition.

4.2.2 Periodic sequences of the $Li_2La_2Ti_3O_{10}$ phase

Typical HAADF-STEM images of the $Li_2La_2Ti_3O_{10}$ phase oriented along [100] and [110] are shown in Figure 4.17a, b. $Li_2La_2Ti_3O_{10}$ is composed of two subsequent La-rich layers with bright contrast (denoted as n=2) separated by Li-rich layers with dark contrast. In $Li_2La_2Ti_3O_{10}$, all available 12-fold coordinated interstices inside the La-O layers are occupied with La atoms (100% occupancy), whereas in LLTO perovskites, the occupancy of these sites with La is up to 67% (theoretically in $La_{0.67}TiO_3$) and depends on the composition (the Li content) and symmetry of the phase. Along the [001] direction, La-rich layers interchange with octahedral Ti-O_2 layers that have lower intensity, forming pseudo-perovskite blocks. Occasionally, the periodic sequences of $Li_2La_2Ti_3O_{10}$ are interrupted by a pseudo-perovskite block with a higher number of La-rich layers with n>2.

The main structural features of $Li_2La_2Ti_3O_{10}$ along the [100] and [110] zone axes are presented in higher-magnification HAADF-STEM images with superimposed structural models (Figure 4.17c, d). The (100) layers of the pseudo-perovskite blocks are shifted for one-half of the unit cell in the [010] direction across the Li-rich layer. In the [110] direction, no shift of the edge-on oriented $(1\bar{1}0)$ lattice planes is observed (marked by red lines on

the superimposed structural models in Figure 4.17c, d). The shifts are characteristic of Ruddlesden-Popper (RP) phases [242], [243].

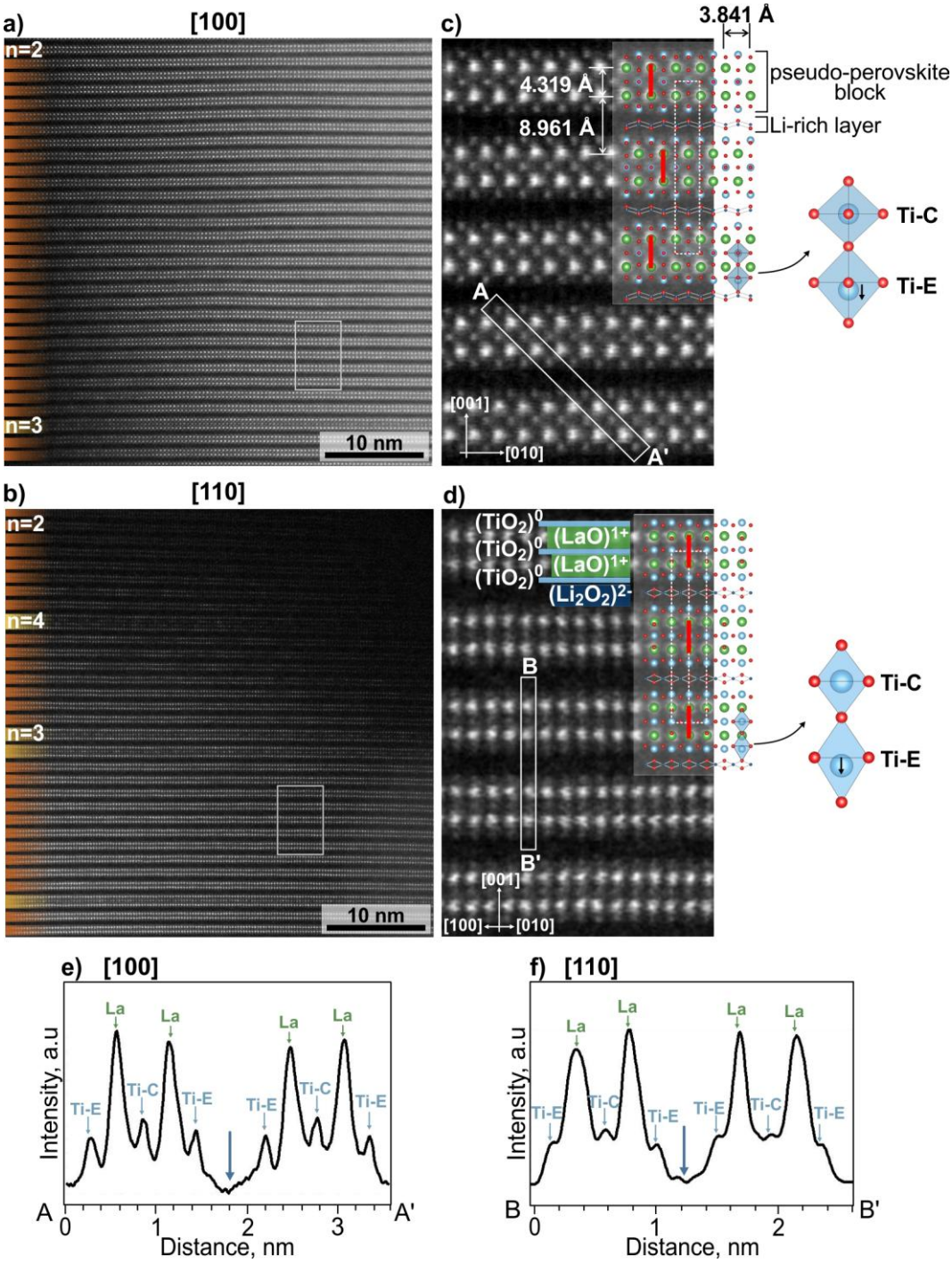

Figure 4.17: HAADF-STEM images of the periodic $Li_2La_2Ti_3O_{10}$ phase (n=2) with the corresponding FFT patterns along (a) [100] and (b) [110] zone axes. (c,d) High-resolution HAADF-STEM images with superimposed $Li_2La_2Ti_3O_{10}$ structural model. (e,f) A-A' and B-B' intensity profiles marked on (c) and (d) show different intensities of Ti-C and Ti-E columns.

The average charge of the La-O layers is 1+ (La^{3+}–O^{2-}), while the Ti-O_2 layers are electroneutral (Ti^{4+}–$2{\cdot}O^{2-}$), yielding overall electropositive $(La_2Ti_3O_8)^{2+}$ pseudo-perovskite blocks. The subsequent blocks are separated by electronegative $(Li_2$–$O_2)^{2-}$ layers ($2{\cdot}Li^{+}$–$2{\cdot}O^{2-}$), which compensate for the positive charge of the pseudo-perovskite blocks.

The described characteristics of the $Li_2La_2Ti_3O_{10}$ phase in terms of the average charge of the atomic layers along the c-direction (out-of-plane) are reflected in the average spacings between the atomic layers in different directions. Overall, the periodic $Li_2La_2Ti_3O_{10}$ sequences have tetragonal symmetry with out-of-plane spacings between the La-O layers within the pseudo-perovskite blocks of 4.319 Å, whereas the spacings between the La-O layers across the Li_2-O_2 layer are more than twice the value, *i.e.* 8.961 Å. The distances between the (010) layers (in-plane) are 3.841 Å.

Due to the interchanging of atomic layers with different compositions and average charges, the Ti-O_2 octahedral layers are of two types; in the central Ti-O_2 layers (marked as Ti-C) positioned symmetrically between two La-O layers of the pseudo-perovskite block, the Ti atoms are centered in the Ti-O_6 octahedra, whereas in the edge Ti-O_2 layers (Ti-E), next to the Li_2-O_2 layers, the Ti cations are slightly displaced towards the Li-rich layer (Figure 4.17c,d). In experimental HAADF-STEM images, the Ti-E columns have slightly lower intensity in comparison to the Ti-C columns, as shown on the A-A' and B-B' intensity profiles in [100] and [110] zone axes (Figure 4.17e, f). In the [100] zone axis, the Ti-columns in the Ti-E layers do not coincide with the O-positions like in the Ti-C layer, which could be the reason for the lower intensity of the Ti-E columns in Z-contrast images. However, in the [110] projection, where the Ti-column positions are separated from the O-column positions, the projected composition of Ti-C and Ti-E is identical, but the intensity of the Ti-E columns in HAADF-STEM images is still lower in comparison to the Ti-C columns.

To confirm that the lower intensity of the Ti-E atomic columns originates from the structural features and not from the lower occupancy, experimental images were compared to image simulations with different thicknesses since the atomic column intensities are a function of sample thickness [201], [244]. The simulations are based on a structural model of $Li_2La_2Ti_3O_{10}$ (ICSD #82907) [92]. The average intensities of different layers were determined for experimental and simulation images and for comparison, the intensity ratios between Ti-E and Ti-C layers with La layers ($I_{Ti\text{-}E}$:I_{La} and $I_{Ti\text{-}C}$:I_{La}) were calculated. The La layers were taken as a reference in the intensity ratio since the two La layers in the $Li_2La_2Ti_3O_{10}$ pseudo-perovskite block are fully occupied with La atoms and have equivalent (but mirrored) local surroundings within the periodic structure.

The results graphically presented in Figure 4.18a and b show that for both projections, the lower intensity of the Ti-E columns relative to the Ti-C columns is well reproduced in simulations, which confirms that the absolute intensity of an atomic column in HAADF-STEM depends not only on the average Z of the atomic column but also on its local neighborhood. This phenomenon was also observed by Baladés et al. (2019), who showed that the intensity of an atomic column with identical composition changes in dependence on the distance and composition of the neighboring atomic columns. For example, an atomic column surrounded by columns with higher average Z (as Ti-C) will have higher intensity due to the transfer of probe intensity from neighboring columns, also referred to as crosstalk [205], [245].

The intensity profiles of simulations (for comparison with the experimental profiles) across two pseudo-perovskite blocks are shown in Figure 4.18c and d. In addition to the different intensities of the Ti-C and Ti-E columns, it is also important to highlight that no significant increase in intensity inside the Li_2-O_2 layers was detected (marked with blue arrows in the profiles). This is expected since in $Li_2La_2Ti_3O_{10}$, only Li and O atoms reside in this layer and are too light to yield contrast in HAADF-STEM.

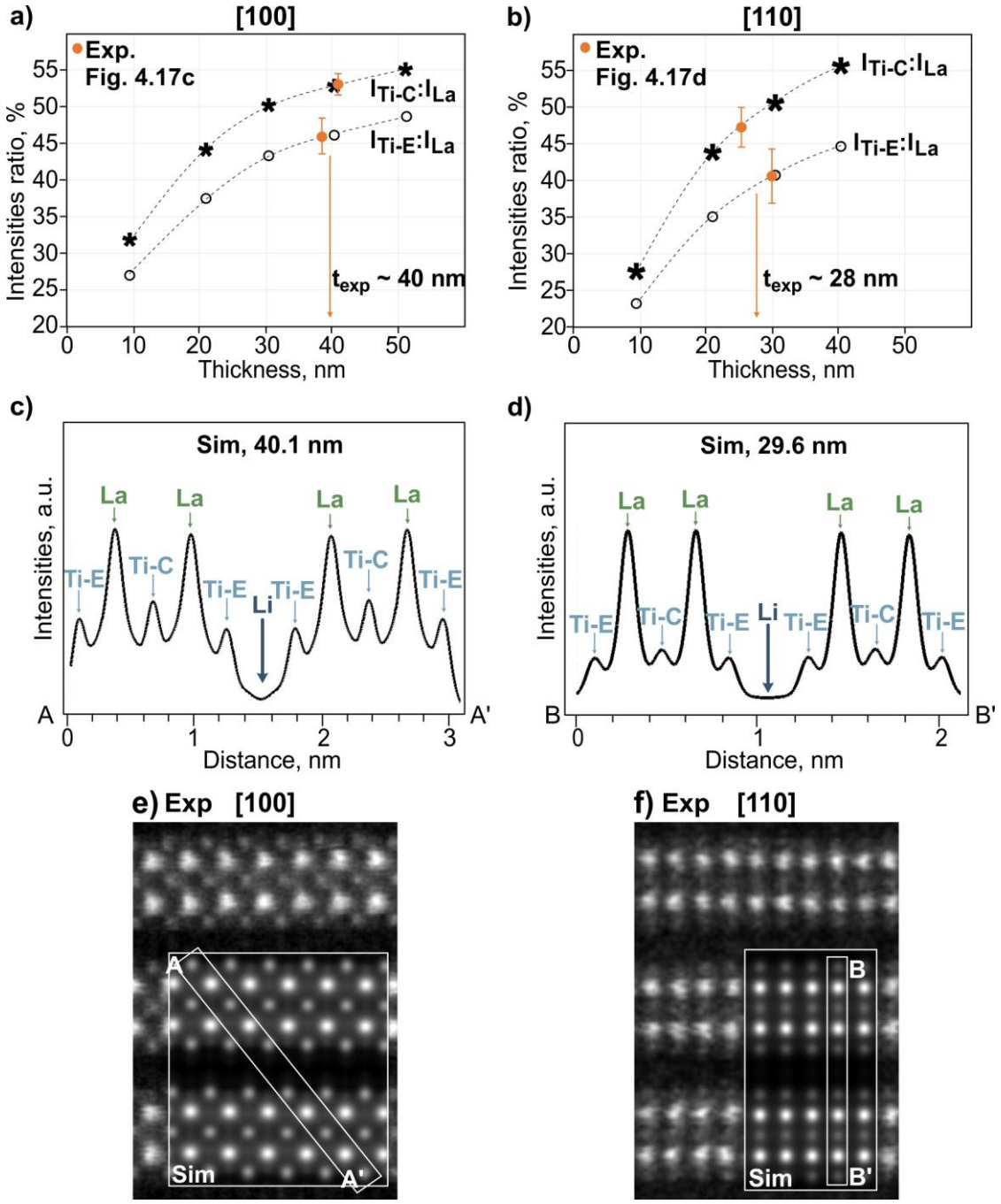

Figure 4.18: (a,b) Intensity ratios in dependence on the sample thickness calculated from $Li_2La_2Ti_3O_{10}$ simulations in [100] and [110] zone axes. The values determined from experimental images are marked with orange. (c,d) Intensity profiles across two pseudo-perovskite blocks in a simulation of $Li_2La_2Ti_3O_{10}$ in [100] and [110] zone axes for thickness 40 nm and 30 nm, respectively. (e,f) HAADF-STEM images with overlaid image simulations (Sim) for the calculated sample thicknesses.

The intensity ratio values at different thicknesses obtained from simulations were used also for the determination of the thicknesses of the sample area. The thickness in experimental situations (Figure 4.17c, d) was extrapolated from the thickness-dependent intensity ratio for simulations and estimated to be 40 nm and 28 nm for [100] and [110]

zone axes, respectively. Simulations for both orientations for the determined sample thicknesses are overlaid on the experimental images (Figure 4.18e, f).

Plate-like grains predominantly consist of periodic sequences of the $Li_2La_2Ti_3O_{10}$ with La:Ti ratio of 0.67. This perfectly matches with the La:Ti ratio determined with SEM/EDS analysis on exaggeratedly grown plate-like grains. This correlation suggests that the anisotropic grains in the sample with initial La:Ti=0.605 are composed of thicker sequences of $Li_2La_2Ti_3O_{10}$.

4.2.3 Non-periodic sequences of parallel planar defects

In contrast to periodic sequences of the $Li_2La_2Ti_3O_{10}$ phase, which were not that frequently observed in the sample, sequences of non-periodic RP-type planar defects were more common. These were observed to form individual plate-like grains and, in addition, all lamellae inside the smaller matrix LLTO grains contain sequences of non-periodic RP-type defects. Figure 4.19a shows a thin plate-like grain with a non-periodic layered structure, which is visible in the high-resolution image (Figure 4.19b). This is as well reflected in the FFT pattern, which displays streaks, rather than distinct peaks (Figure 4.19c).

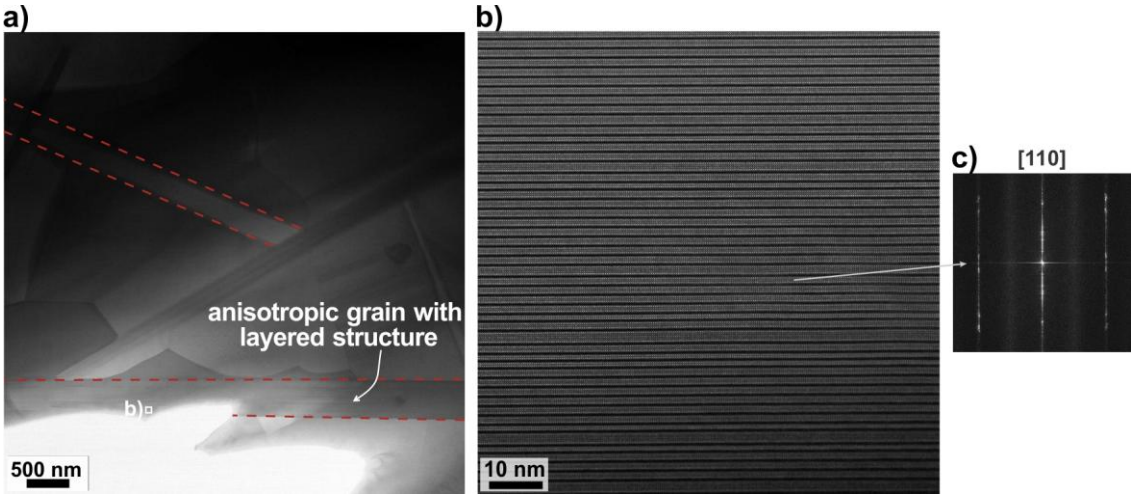

Figure 4.19: (a,b) Highly anisotropic plate-like grains with non-periodic structure as shown on (b) high-resolution HAADF-STEM image and (c) the corresponding FFT pattern with streaks in the out-of-plane direction.

Figure 4.20a shows a sequence of parallel RP-type defects inside a LLTO matrix grain. The in-grain lamellae commonly contain sequences of planar defects with a non-periodic or modulated structure and thickness up to 200 nm. Defects can be partially recrystallized to matrix LLTO, as marked in with frames in Figure 4.20a.

Modulated sequences inside the matrix LLTO grains are composed of non-periodically arranged Li-rich layers that separate perovskite blocks of varying thicknesses, defined by a different number of La-rich layers (n) (Figure 4.20b). In [100] zone axis, two subsequent blocks always exhibit the RP shift regardless of the number of La-rich layers in the perovskite block. While blocks with two La layers (n=2) correspond to segments of the $Li_2La_2Ti_3O_{10}$ phase, thicker LLTO blocks (n>2) have additional LLTO perovskite layers sandwiched between the Li-rich layers. Atomic columns in Li-rich layers of the modulated sequence exhibit weak contrast.

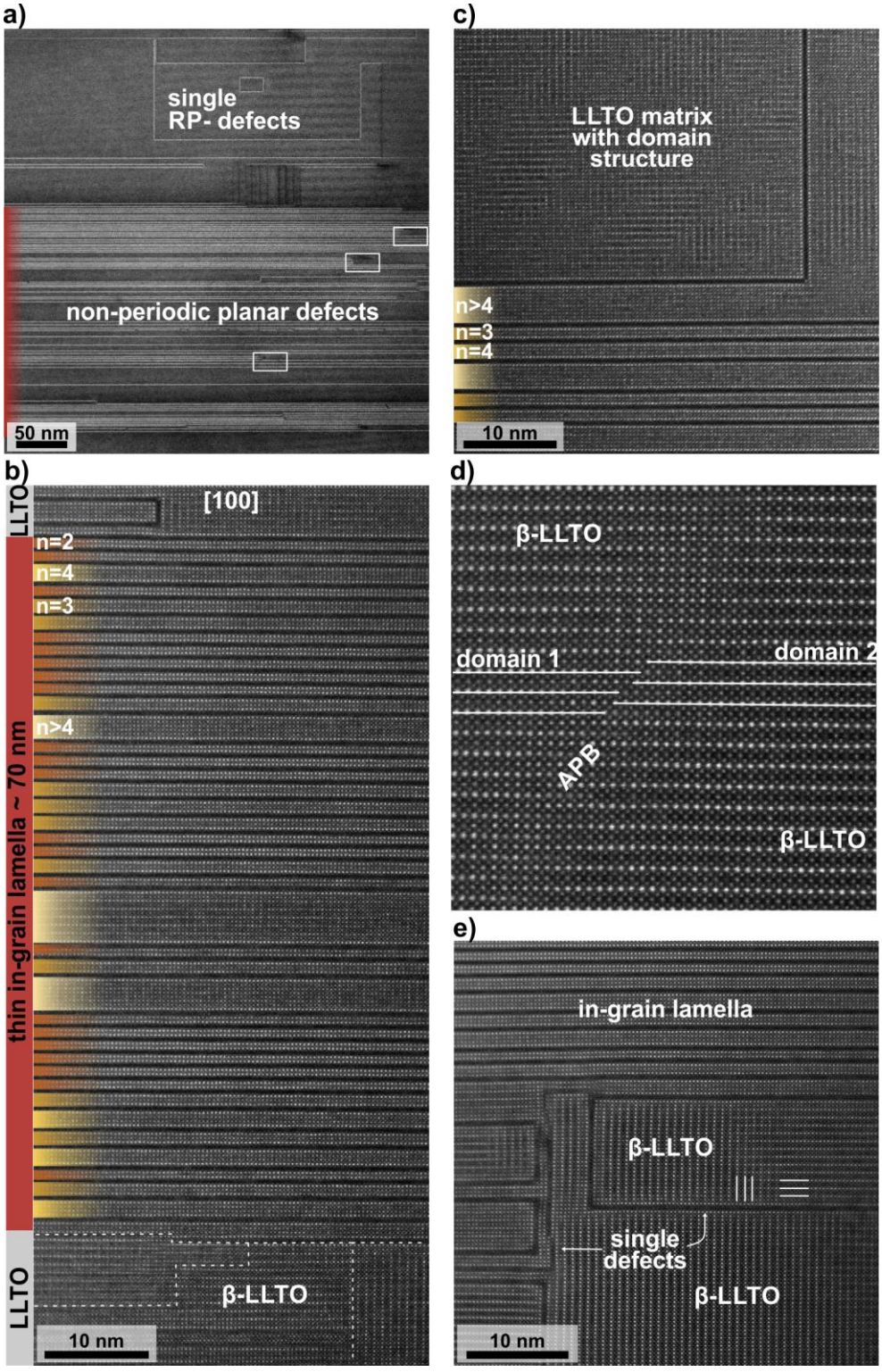

Figure 4.20: (a) In-grain lamella with a non-periodic sequence of RP-type defects. Some defects are recrystallized (framed areas). (b) Non-periodic structure along the [100] zone axes, where Li-rich layers separate pseudo-perovskite blocks with variable thicknesses (n). (c) Domain structure of matrix β-LLTO next to the in-grain lamellae with non-periodic structure. (d) Contact between two domains oriented along [100] zone axis, forming an anti-phase boundary parallel to (110). (e) Single planar defects of $Li_2La_2Ti_3O_{10}$ phase in LLTO matrix, extending along all three [100] directions. A 90 ° domain boundary is common in the β-LLTO.

The LLTO inside the perovskite blocks with n>4 resembles α-LLTO with a disordered arrangement of the A-site ions, whereas the matrix LLTO has a domain structure, which is composed of interchanging La-rich and La-poor atomic layers, typical for β-LLTO (Figure 4.20c). In principle, the exact composition of LLTO next to the lamellae could be determined using simulations. However, in practice, the absence of a clear reference point, such as fully occupied La layers in the $Li_2La_2Ti_3O_{10}$ sequences, and other parameters like thickness and degree of ordering prevent accurate estimation of the LLTO composition (x-value).

LLTO domains are a few tens of nanometers large and are oriented in all three pseudocubic [100] directions. When the LLTO domain is oriented in [100] or [010] zone axes, the La-rich layers of LLTO are parallel or perpendicular to the Li-rich layers in the modulated sequence oriented along the [100] zone axis, respectively. When the LLTO domain is oriented along [001], its structure appears disordered. Neighboring domains can meet at an anti-phase boundary (APB) (Figure 4.20d) or can be oriented to form a 90 ° domain boundary (marked in Figure 4.20e). Matrix LLTO often contains single RP-type defects that extend along the equivalent {100} planes of the perovskite lattice, usually forming loops (Figure 4.20e). The RP-type shift for half of the unit cell across the Li-layer is observed also in single defects. These defects in LLTO ceramics were previously described as single-atom-layer traps (SALT) [136] or intrinsic layer defects [246], however, their local atomic structure and composition were related to $(Li_{0.37}Ti_{0.33}O)^{0.31-}$ phase and not to the $Li_2La_2Ti_3O_{10}$ phase.

EELS analysis was performed to confirm the presence of Li inside the RP-type defects and to determine the valence state of Ti. The analyses were conducted inside the lamella (RP-type defect) and in matrix LLTO (Figure 4.21). EELS confirmed the presence of Li inside the layers with a dark contrast in the modulated sequence. The Li peak obtained in the defect has a slightly higher intensity than in LLTO, which is expected, as the $Li_2La_2Ti_3O_{10}$ phase contains about 2.3 at% of Li, whereas the $Li_{0.33}La_{0.56}\square_{0.11}TiO_3$ phase only around 1.3 at%.

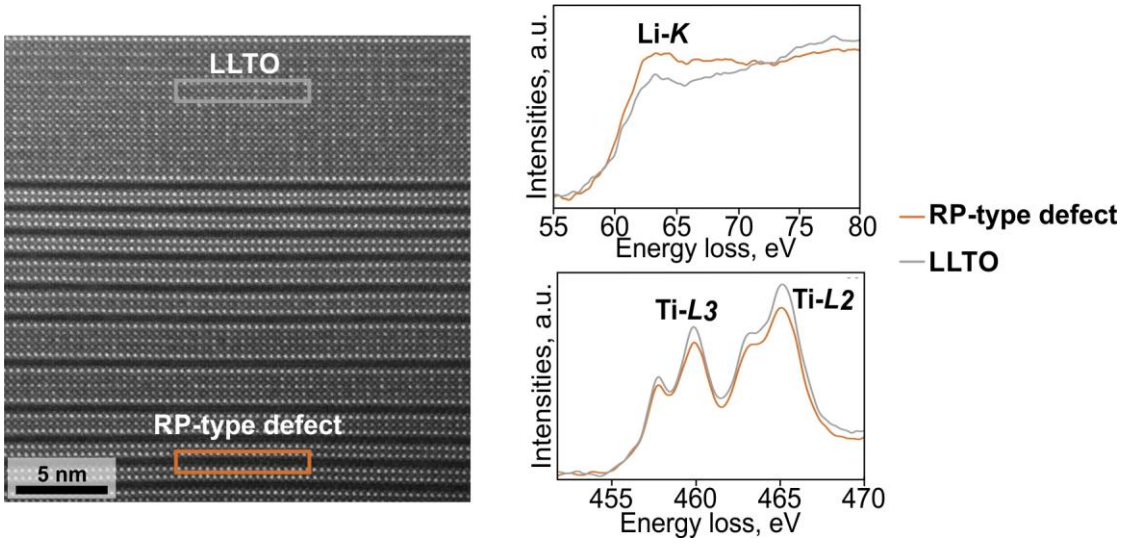

Figure 4.21: HAADF-STEM image of non-periodic RP-type defects (below) in contact with LLTO (above), where EELS analyses were performed to confirm the presence of Li (Li *K* edge) and valence state of Ti (Ti $L_{2,3}$ edge). The Ti-$L_{2,3}$ white lines in both spectra are positioned at the same energy indicating the presence of Ti in 4+ oxidation state in both areas.

Additionally, the nonstoichiometry in the initial LLTO composition with a La:Ti ratio of 0.605 could introduce a change in a valence state and cause electrical conductivity of the material, which is detrimental for applications of the material as a solid electrolyte in a battery. The edge structure of Ti is similar in both areas and the Ti-L_2 and Ti-L_3 peak splitting confirms that Ti is in a tetravalent state in LLTO and inside the RP-type defect. The small difference in the edge structure could be ascribed to the distortion of Ti-octahedra inside the defect layer [136].

Structural characteristics of the RP-type non-periodic sequences in terms of atomic column positions and their intensities were studied in more detail in the high-resolution HAADF-STEM image, acquired in an area with an overall thickness around 30 nm as determined by EELS (Figure 4.22a). At the edge of the sample, a thin part of the amorphous region (blue) with a thickness from 10 to 15 nm is present.

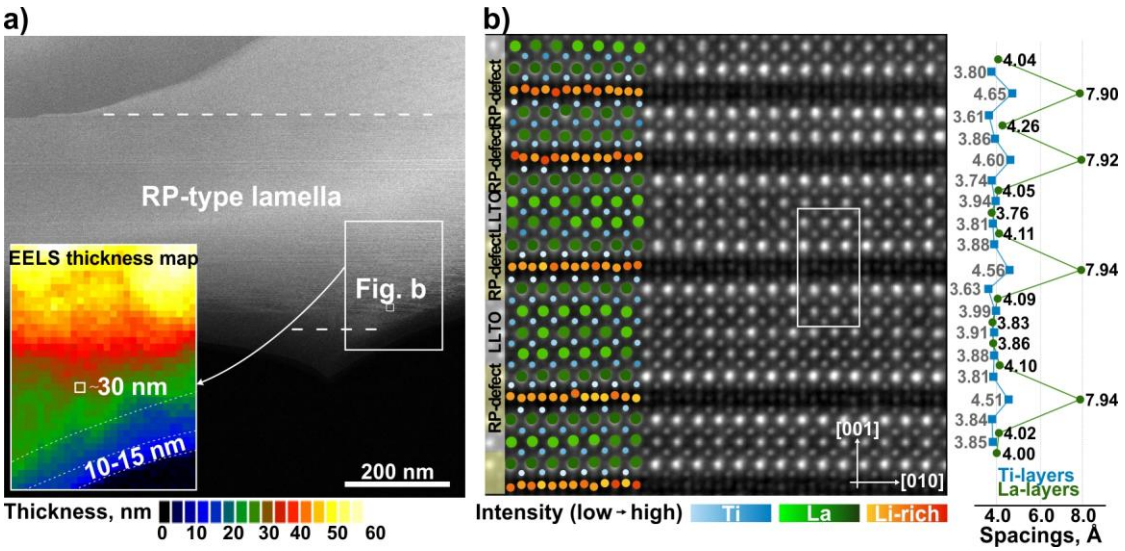

Figure 4.22: (a) A non-periodic RP-type lamella with EELS thickness map. (b) Higher magnification image of the non-periodic sequence with overlaid intensities of the La, Ti, and Li-rich atomic columns (left). The measured distances between the subsequent La layers (green) and Ti-layers (blue) in the [001] direction are shown on the right.

La layers in a non-periodic lamella have different average intensities (Figure 4.22b). La layers of the RP-type defect layers, which are also edge layers of the perovskite blocks (La-E layers), have the highest intensity ($I_{La\text{-}E}$ = 4769±6%). These La-E layers correspond to the La layers in $Li_2La_2Ti_3O_{10}$, however, they exhibit a higher deviation of intensities in comparison to the periodic sequences, indicating that their occupancy is lower than 100%. The La columns inside the perovskite blocks with n>2 (La-C layers) have about 72% intensity relative to the La-E columns and an even higher standard deviation of intensities ($I_{La\text{-}C}$ = 3448±10%). This indicates lower and random occupancy of La-C columns with La as expected for pseudocubic $Li_{3x}La_{2/3-x}\square_{1/3-2x}TiO_3$. Another significant difference between the periodic and non-periodic sequences is higher intensity inside the Li-rich layers of the RP-type defects (the $(Li_2O_2)^{2-}$ layers in $Li_2La_2Ti_3O_{10}$), suggesting the presence of heavier atoms. The average intensity of the atomic columns in the Li-rich layer is about 25% relative to the intensity of the La-E layers ($I_{Li\text{-}rich}$ = 1200±12%). Atomic columns in the octahedral Ti-O_2 layers show a similar trend as in the periodic $Li_2La_2Ti_3O_{10}$ sequences; the intensity of the Ti-E columns is lower ($I_{Ti\text{-}E}$ = 1945±6%) than the intensity of the Ti-C columns ($I_{Ti\text{-}C}$ =2298±5%).

Distances measured between the atomic layers of the RP-type defects in non-periodic sequences in the [001] direction, i.e. parallel to the RP-type defects, exhibit significant differences compared to the $Li_2La_2Ti_3O_{10}$ phase. The La-E layers of the RP-type defects are contracted for about 11% (~7.9 Å) in comparison to the equivalent spacing in the $Li_2La_2Ti_3O_{10}$ (8.961 Å). Furthermore, the spacings between the La-E layers and the first La-C layer of the perovskite block are always slightly larger (~4.0-4.1 Å) than the spacings in inside the perovskite blocks with n>3 (~3.9 Å). On the other hand, the Ti-E layers inside the RP-type defects are shifted slightly towards the La-E layers.

The observed relaxations of the La-E layers across the RP-type defects, their higher standard deviations of intensities, and the presence of brighter contrast inside the Li-rich layers indicate a certain degree of ion exchange between the Li-layers and the neighboring La layers within the RP-type defect.

4.2.4 Evaluation of the exchange rate

The degree of ion exchange between the Li-rich layers and the neighboring La-layers was estimated using multislice frozen-phonon simulations. The models used for simulations were based on the theoretical $Li_2La_2Ti_3O_{10}$ structural model. To ensure the model closely resembled the experimental material, the atomic positions $Li_2La_2Ti_3O_{10}$ model were first adjusted based on the average positions determined from experimental HAADF-STEM observations (Figure 4.23). The thickness of the structural models was 50 nm in [100] direction.

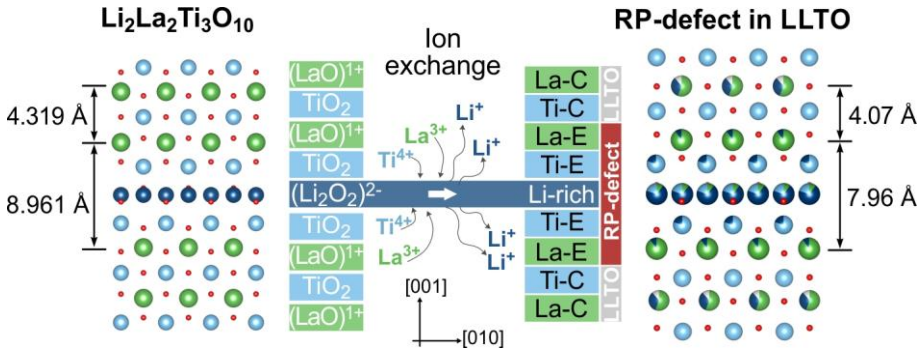

Figure 4.23: The starting model of a RP-type defect for evaluation of the ion exchange rate between the Li-rich layer and La-E and Ti-E layers is based on the $Li_2La_2Ti_3O_{10}$ structure. In the model, the distances between layers are modified according to the experimental image (Figure 4.22). The occupancy of Li-, La-E, and Ti-E columns was modified as described in the main text.

Models were prepared with different occupancies of the atomic layers inside the RP-type defect, consisting of layer sequence La-E – Ti-E – Li – Ti-E – La-E. Since thicker blocks of non-periodic sequence (n>2) also include LLTO perovskite layer(s) with lower intensity of La-C layers in comparison to La-E layers, the composition of La-C layers (that are further away from the Li-rich layer) in all models was adjusted accordingly. Assuming the composition of these LLTO layers is $Li_{0.33}La_{0.56}\square_{0.11}TiO_3$ (LLTO with x=0.11), the La-C layers in simulations were occupied by 56% of La atoms, 33% of Li atoms and contained 11% of vacancies, while Ti-C layers were fully occupied by Ti atoms.

The La-E, Ti-E, and Li-layers in the "Only Shift" model contain no ion exchange and are fully occupied with La, Ti, and Li, respectively. However, image simulations of this model consistently yielded too high an intensity of the Ti-E columns compared to the

intensity of the Ti-C columns ($I_{Ti\text{-}E}$:$I_{Ti\text{-}C}$). This indicates that the ion exchange in the RP-type defects of non-periodic sequences includes not only La layers (based on the variable intensity of these columns) but also Ti atoms from the Ti-E layer. Models were thus prepared with various fractions of La atoms from La-E layers and Ti atoms from Ti-E layers repositioned to the Li-rich layer. In the prepared models, up to 20% Li atoms in the Li-rich layer were randomly replaced with La and Ti from the two neighboring La-E and two Ti-E layers.

At the same time, the vacant positions in the La-E and Ti-E layers of the structural models were filled with Li atoms as their contribution to the HAADF-STEM contrast is negligible. Nevertheless, Li atoms can occupy different interstitial sites [171] or diffuse to the surrounding LLTO during the ion exchange. Since the number of interstitial sites available in the Li-rich layer in comparison to the neighboring layers is doubled, all vacancies in the La-E and Ti-E layers were replaced with Li atoms from the Li-rich layers, to obtain the overall charge-neutrality. Average compositions of the La-E, Ti-E, and Li-rich layers in the structural models used for image simulations are given in Table 4.3.

Table 4.3: Occupancy of La-E, Ti-E, and Li-rich layers in simulation models with varying degrees of ion exchange. Occupancies of La^{3+}, Ti^{4+}, and Li^{+} given as fractions, the Li-rich layer has twice the number of interstices compared to the La-E and Ti-E layers. The average charge of the La-E and Li-rich layers is calculated as described in the text, and the Li-rich layer composition is provided based on the ion exchange degree.

Layer		**La-E**	**Ti-E**	**Li-rich**	**Charge (La-E)**	**Charge (Li-rich)**	**Composition (Li-rich)**
Only Shift	La^{3+}	1	0	0	1+	2–	$[Li_2O_2]^{2-}$
	Ti^{4+}	0	1	0			
	Li^{+}	0	0	2			
10La-10Ti	La^{3+}	0.9	0	0.2	0.8+	1–	$[La_{0.2}Ti_{0.2}Li_{1.6}O_2]^{1-}$
	Ti^{4+}	0	0.9	0.2			
	Li^{+}	0.1	0.1	1.6			
20La-10Ti	La^{3+}	0.8	0	0.4	0.6+	0.6–	$[La_{0.4}Ti_{0.2}Li_{1.4}O_2]^{0.6-}$
	Ti^{4+}	0	0.9	0.2			
	Li^{+}	0.2	0.1	1.4			
15La-15Ti	La^{3+}	0.85	0	0.3	0.7+	0.5–	$[La_{0.3}Ti_{0.3}Li_{1.4}O_2]^{0.5-}$
	Ti^{4+}	0	0.85	0.3			
	Li^{+}	0.15	0.15	1.4			
10La-20Ti	La^{3+}	0.9	0	0.2	0.8+	0.4–	$[La_{0.2}Ti_{0.4}Li_{1.4}O_2]^{0.4-}$
	Ti^{4+}	0	0.8	0.4			
	Li^{+}	0.1	0.2	1.4			
20La-20Ti	La^{3+}	0.8	0	0.4	0.6+	0	$[La_{0.4}Ti_{0.4}Li_{1.2}O_2]^{0}$
	Ti^{4+}	0	0.8	0.4			
	Li^{+}	0.2	0.2	1.2			

Intensities of the atomic columns in image simulations of the models with different exchange rates and for different thicknesses were analyzed similarly as in the experimental images. For comparison with experimental values obtained from Figure 4.22, the intensity ratios between different layers with the La-E layers were calculated (Figure 4.24a).

The best match of the simulations and the experimental image was determined based on the average absolute differences between the experimental and simulations' intensity ratios (detailed numerical results from the simulations, including all absolute values and intensity ratios, are presented in the Appendix). The closest average absolute difference with the experimental image was obtained for the 15 nm thick "10La-10Ti" model, and also simulations of the 20 nm and 15 nm thick "10La-20Ti" model. The section of the experimental image (from Figure 4.22b) and simulated images with different ion exchange and 15 nm thick crystalline slabs are given in Figure 4.24b.

The average charge of the Li-rich layer after the exchange of a certain fraction of Li atoms with Ti and La can be calculated as $(x\cdot(3+) + y\cdot(4+) + (2-x-y) \cdot (1+) + 2\cdot(2-)$, where x and y are the fractions of La^{3+} and Ti^{4+} in the Li-rich layer, respectively. While the Li_2-O_2 layers in $Li_2La_2Ti_3O_{10}$ are negatively charged (2–), they become less negatively charged with an increasing exchange of Li^+ with La^{3+} and Ti^{4+} and, theoretically, after an exchange with 20 at% of La and 20 at% of Ti (the "20La-20Ti" model), the layer would become electroneutral. At the same time, the average charge of the La-E layer decreases from 1+ up to 0.6+. The reduced number of Ti atoms in the octahedral layer is most likely accompanied by the formation of oxygen vacancies and the formation of distorted octahedra, which is supported by the results of EELS analyses.

The thickness of the area in experimental Figure 4.22 determined with simulations is lower than the thickness measured with EELS. This indicates that the sample contains amorphous material on the surface, that forms during the TEM preparation, like polishing and ion milling, despite efforts to minimize it with low voltage treatment. The presence of an amorphous layer reduces the contrast in HAADF images and should also be considered in simulations [209], [247].

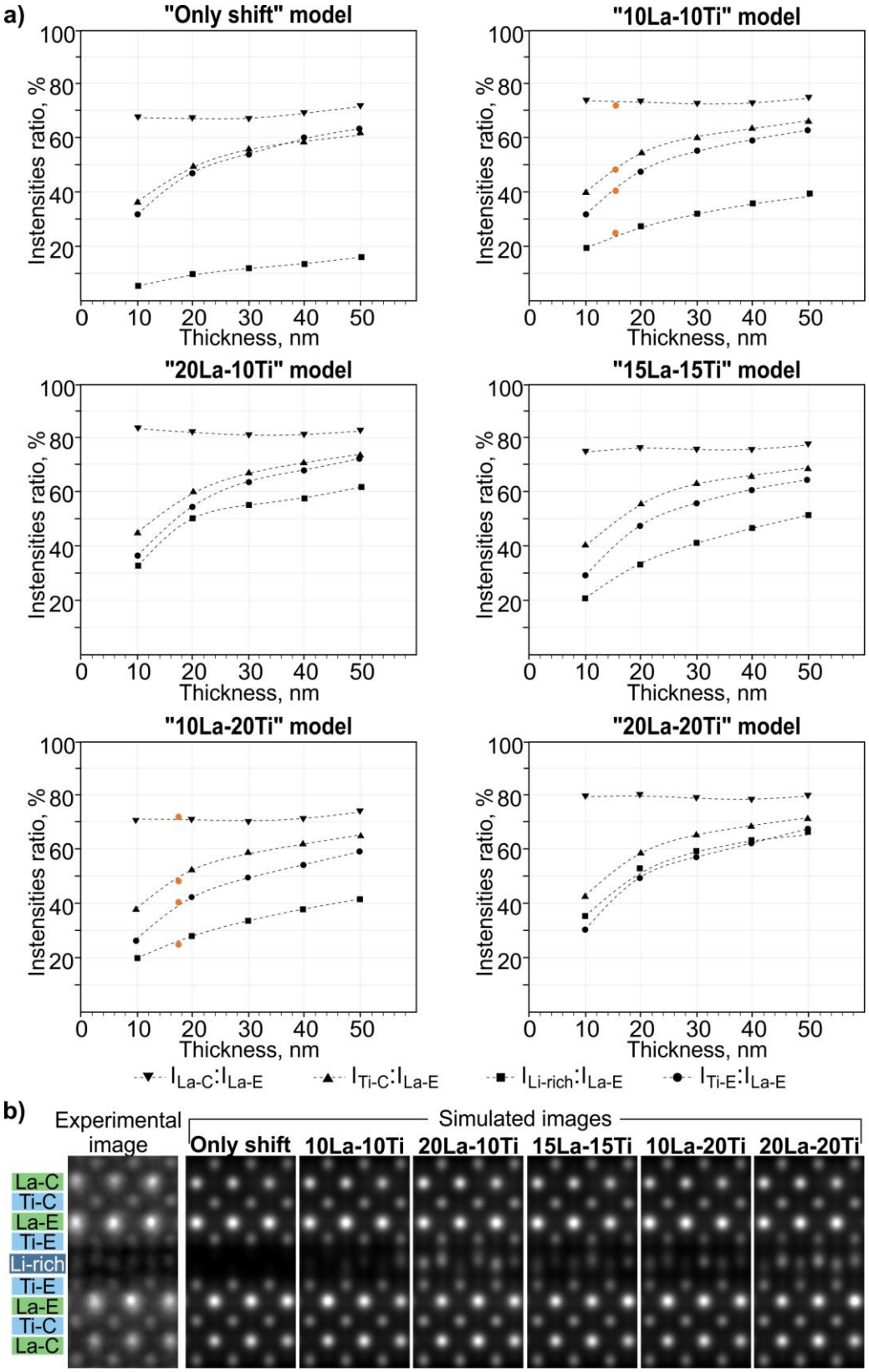

Figure 4.24: (a) Intensity ratios of the atomic columns calculated from image simulations for the models with different exchange rates and thicknesses from 10 to 50 nm. The intensity ratios from the experimental image are marked with orange circles. (b) Comparison of the experimental image with image simulations of different structural models for the thickness of 15.2 nm.

To evaluate the effect of the amorphous layer on the intensity ratios, we simulated the three models with the best fit with the addition of amorphous layers to obtain the overall thickness of 30 nm (Figure 4.25).

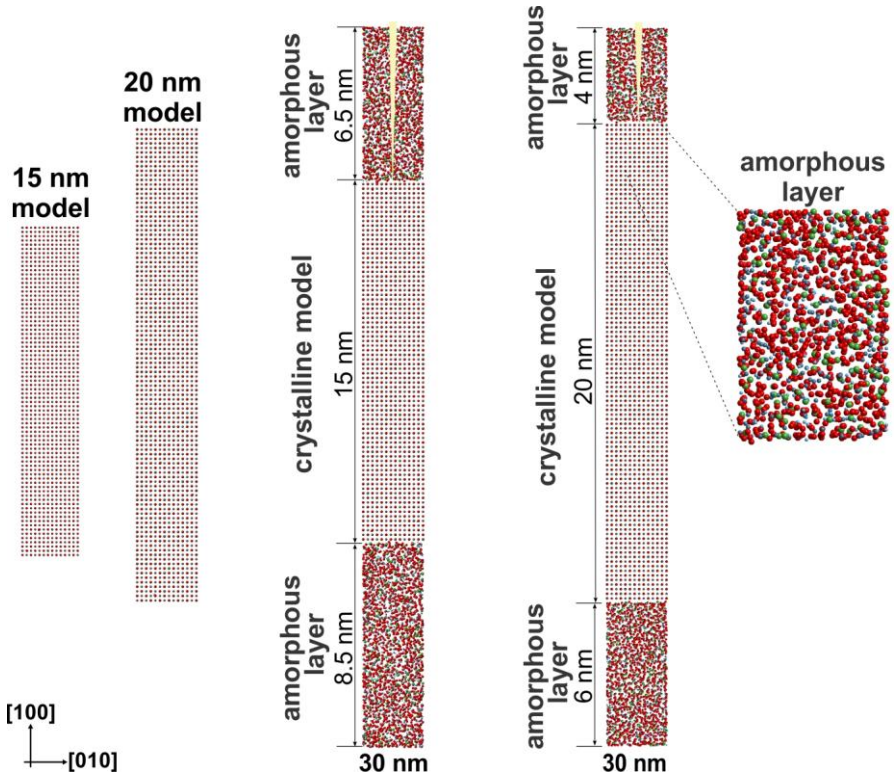

Figure 4.25: Structural models with thicknesses of 15 and 20 nm and models with the addition of an amorphous layer to obtain a total thickness of 30 nm. The focus in simulations was always set on the crystalline part of the model.

The amorphous layers were prepared from crystalline models by removing half of the atoms (random) to reduce the density as expected for the amorphous layer and then, the remaining atoms were randomly displaced from their regular positions by keeping a minimum critical distance of around 2 Å between the neighboring atoms. The total thickness of the amorphous layer for the 15 nm thick model of "10La-10Ti" and "10La-20Ti" was 15 nm and for the 20 nm thick "10La-20Ti" model was 10 nm. The amorphous slab was divided above and below the crystalline model. The lower amorphous layer was 2 nm thicker than the upper layer to simulate also the amorphous carbon that was sputtered on the sample surface before the STEM analysis. To match the experimental conditions, where the beam is always focused on the crystalline part, the simulation of the models with the amorphous layers was calculated with defocus on the crystalline part (defocus of −6.5 nm and −4 nm, respectively).

While the simulations of 15 nm thick "10La-10Ti" and 20 nm thick "10La-20Ti" with the addition of an amorphous layer exhibit larger differences to the experimental values, the 15 nm thick "10La-20Ti" model shows an improved fit to the experimental intensity ratios (Table 4.4).

Table 4.4: Comparison of image intensity ratios in image simulations having the closest match with the experimental values from the HAADF-STEM image, and identical models with additional amorphous layers.

		$I_{La\text{-}C}/I_{La\text{-}E}$	$I_{Li}/I_{La\text{-}E}$	$I_{Ti\text{-}E}/I_{La\text{-}E}$	$I_{Ti\text{-}C}/I_{La\text{-}E}$	Average absolute difference
		Absolute differences to the reference				
"10La-10Ti" model	15 nm (crystalline)	**75.3**	**22.3**	**40.4**	**48.3**	
		3.0	2.9	0.4	0.1	1.6
	30 nm (15 nm crystalline + 15 nm amorphous)	**73.8**	**27.2**	**46.1**	**52.3**	
		1.5	2.0	5.3	4.1	3.2
"10La-20Ti" model	20 nm (crystalline)	**71.5**	**28.3**	**42.5**	**52.4**	
		0.8	3.2	1.7	4.2	2.5
	30 nm (20 nm crystalline + 10 nm amorphous)	**73.5**	**29.9**	**44.7**	**53.7**	
		1.2	4.8	3.9	5.5	3.8
	15 nm crystalline	**72.4**	**23.9**	**35.4**	**46.6**	
		0.1	1.3	5.4	1.6	2.1
	30 nm (15 nm crystalline + 15 nm amorphous)	**71.7**	**28.7**	**40.7**	**49.9**	
		0.6	3.5	0.1	1.7	1.5
Exp. image		**72.3**	**25.2**	**40.8**	**48.2**	**reference**

Comparison of image simulations of models with different compositions with the experimental image suggests that up to 10% of La and up to 20% of Ti from the La-E and Ti-E layers exchange with Li in the RP layer. The actual composition of different RP-type defects may vary slightly, however, all models with a higher La exchange rate show a worse fit indicating that the exchange of Ti is faster than that of La. With progressive ion exchange and out-diffusion of Li, the layers of RP-type defect become structurally unstable and progressively recrystallize to LLTO perovskite.

4.2.5 Conclusions

The main findings of the second part of the study are:

- layered periodic structure in plate-like grains corresponds to the $Li_2La_2Ti_3O_{10}$ phase,
- Ti-C and Ti-E layers in $Li_2La_2Ti_3O_{10}$ exhibit different intensities, depending on the distance and composition of their neighboring atomic columns,
- plate-like grains and in-grain lamellae usually contain non-periodic structures with structural elements of the $Li_2La_2Ti_3O_{10}$ phase,
- non-periodic sequences consist of RP-type defects and LLTO perovskite layers of varying thicknesses,
- in non-periodic sequences, 10% La^{3+} and 20% Ti^{4+} exchange Li^{+} in the Li-rich layers,
- simulations can provide quantitative information on experimental HAADF-STEM column compositions and sample thicknesses.

4.3 Oriented Topotaxial Recrystallization of Ruddlesden-Popper-Type Defects to LLTO

The results of SEM and XRD analyses have shown that $Li_2La_2Ti_3O_{10}$ lamellae and structurally related RP-type sequences with non-periodic modulated structure in LLTO grains start to form in the early stage of microstructure development, even before significant densification of the sample (below 1250 °C). It was reported that the $Li_2La_2Ti_3O_{10}$ phase can be synthesized by a solid-state reaction from stoichiometric starting powders at 1200 °C [92], [109], [248]. At around 1250 °C, when the sample is densified to the level suitable for the preparation of TEM samples, the RP-type defects in the non-periodic sequences undergo significant internal ion exchange. At the same time, some lamellae begin to recrystallize to LLTO perovskite (Figure 4.26). The process may be described as the topotaxial recrystallization of layered 2D perovskite to 3D perovskite [249] along the [100] direction of $Li_2La_2Ti_3O_{10}$.

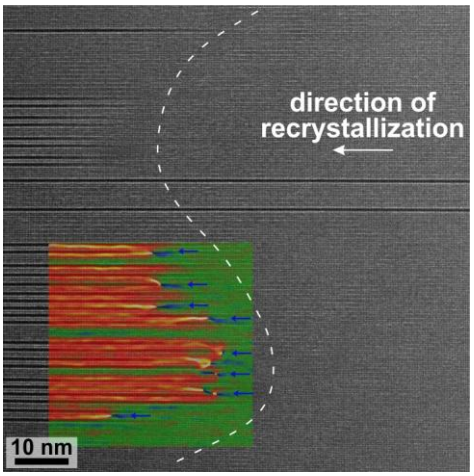

Figure 4.26: Recrystallization of a non-periodic lamella to LLTO perovskite. Geometric phase analysis was used to identify the additional lattice planes in the newly formed LLTO (marked by blue arrows).

4.3.1 Structural characterization of the recrystallization zones

Recrystallization kinetics of the non-periodic sequence varies, as some RP-type defects in in-grain lamella recrystallize faster than others, leading to the formation of a curved recrystallization front (Figure 4.27a). Due to the mismatch between the non-periodic sequences with RP-type defects and the newly forming LLTO, the transformation is accompanied by the formation of an additional lattice plane every few nanometers (blue arrows in the inset in Figure 4.26). In non-periodic lamellae, the formation of additional lattice planes occurs at different distances. The additional lattice planes were identified by geometric phase analysis (GPA) [250], which quantifies small changes in the periodicity of the lattice and provides spatial information about lattice distortions and local strain.

Additionally, BF-STEM images revealed the occurrence of dark areas at the recrystallization front, which could be related to the diffusion of lithium from the RP-type defects to LLTO (Figure 4.27b). Darker contrast could also stem from strain at the interface between the RP-type defects and LLTO, however, GPA does not show any increase in in-plane strain and remains around zero in the whole area (Figure 4.27c). The

out-of-plane strain map shows higher strains around the dislocation cores (Figure 4.27d), whereas there is no special increase in strain in the areas that exhibit darker contrast in the BF-STEM image (encircled). Determination of Li concentration in these areas with EELS is challenging as the differences in Li content in the RP-type defects and LLTO are small and within the EELS measurement error.

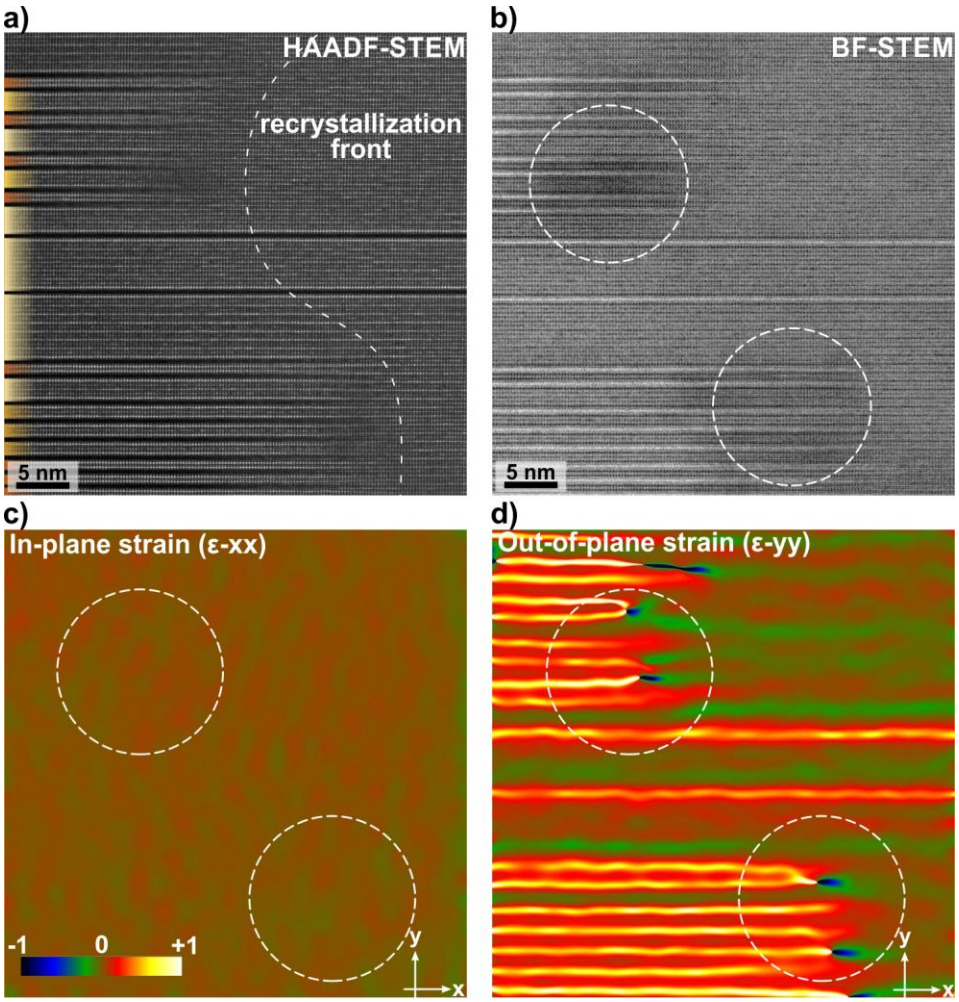

Figure 4.27: (a) Higher magnification HAADF-STEM image of recrystallization zone showing progressive recrystallization of an in-grain lamella. (b) BF-STEM image discloses dark regions (encircled) possibly indicating the diffusion of Li from the Li-rich defects to LLTO during recrystallization. (c,d) In-plane and out-of-plane strain maps at the recrystallization front.

According to the high-resolution image of the recrystallization region along [100] zone axis of LLTO (Figure 4.28a), RP-type lamellae can recrystallize directly to LLTO (upper situation) or by formation of an additional lattice plane (lower situation, the additional lattice plane in LLTO is marked by yellow color).

In the recrystallization process, the La atoms from (almost) fully occupied La-columns of the RP-type defects (the La-E layers) rearrange to the A-sites of the La-poor layers of the newly formed LLTO perovskite, along with Li and vacancies (Figure 4.28b). Excess Li can easily diffuse into the surrounding LLTO matrix due to its high mobility. In the areas

where additional lattice planes are formed, the amount of Ti is slightly deficient, which is likely compensated by oxygen vacancies.

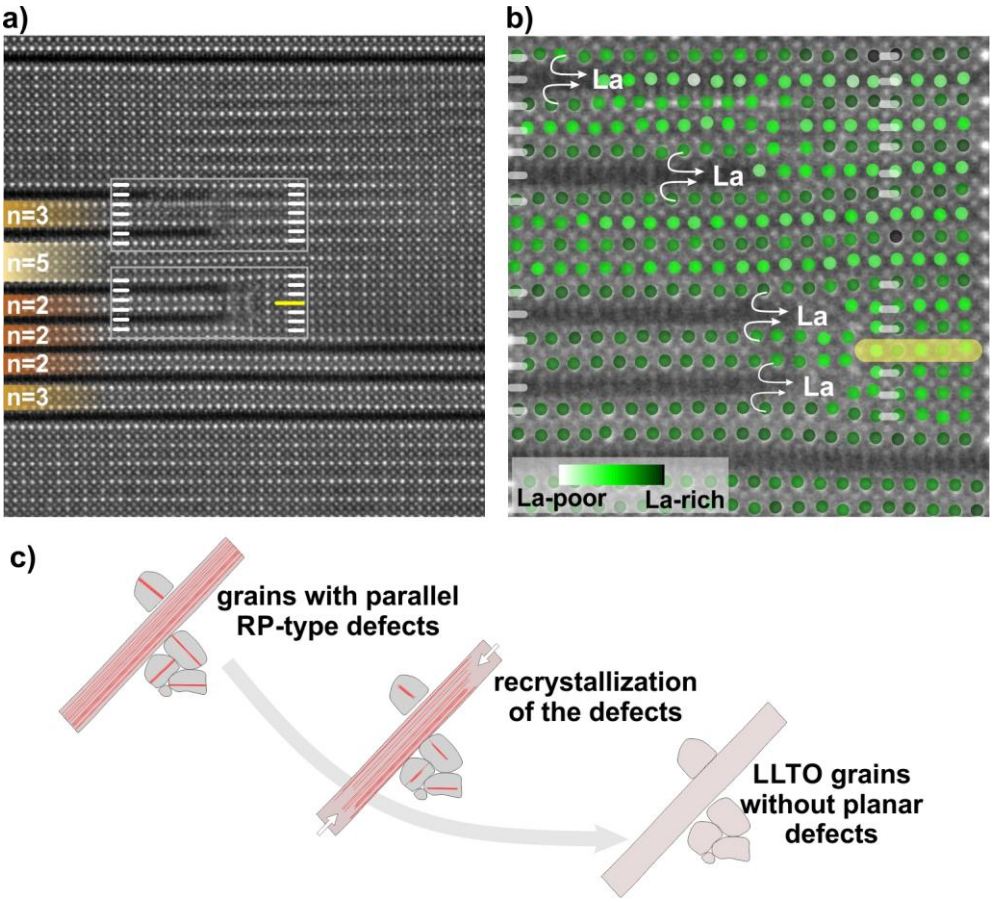

Figure 4.28: (a) Recrystallization of non-periodic parallel RP-type defects to LLTO without and with the formation of an additional lattice plane in the newly formed LLTO (marked by a yellow line). (b) La atoms rearrange to the A-sites of the La-poor layers of the LLTO. Simultaneous recrystallization of two RP-type defects is required to cancel out the RP shift. (c) Grains with RP-type lamellae are transformed into LLTO perovskite grains without planar defects.

During the recrystallization, the RP shift of two subsequent RP-type defects is canceled out and the recrystallization of an even number of parallel defects is energetically not demanding. However, in case of an odd number of RP-type defects, removal of the one remaining defect would require recrystallization of a large LLTO domain, which would be energetically more demanding. For this reason, single planar defects occasionally remain inside the LLTO matrix and form isolated 2D defects. Zhu et al. (2020) [135] described such defects as single-atom-layer traps (SALTs) and showed that these defects limit Li ionic transport and degrade the total conductivity. Therefore, recrystallization of as many defects as possible is beneficial for the bulk ionic conductivity of LLTO.

Recrystallization of RP-type lamellae starts at the grain boundaries and progresses towards the interior of the grains. In this process, the grains are converted from LLTO grains with RP-type defects to normal LLTO perovskite grains (Figure 4.28c). Assuming a comparable recrystallization rate, it is likely that the recrystallization of smaller LLTO

grains with shorter and thinner in-grain lamellae is completed sooner than the recrystallization of the large plate-like grains with thicker and longer RP-type lamellae.

4.3.2 Thermodynamic stability of LLTO-based perovskites

4.3.2.1 Calculation

To understand the early formation of the $Li_2La_2Ti_3O_{10}$ phase and its further recrystallization to LLTO perovskite, first-principles calculations based on density functional theory (DFT) were performed to evaluate the thermodynamic phase stability. To simulate the experimental conditions, the experimental precursor stoichiometry (Li:La:Ti = 11:15:25) was used for phase stability evaluation. Since the amount of O in the system could not be simply determined from the experimental precursors in an open system, the stoichiometry of O in the system was decided by finding the most stable combination of stable compounds with Li:La:Ti = 11:15:25 at the ground state, *i.e.*, at 0 K. With the calculated formation energies of all the known stable compounds in the Li-La-Ti-O quaternary system, the most stable combination of compounds was determined to be 2.5 Li_2TiO_3 + 1.5 $Li_4Ti_5O_{12}$ + 7.5 $La_2Ti_2O_7$. Therefore, the system was presumed to be with the Li:La:Ti:O = 11:15:25:78 stoichiometry for thermodynamic phase stability evaluations.

First, assuming that the main reaction product is $Li_{0.167}La_{0.61}TiO_3$ perovskite with La:Ti ratio as in the starting powder, a $Li_3La_{11}Ti_{18}O_{54}$ model was built to simulate the LLTO phase. The reaction of the most stable combination of compounds reacting into $Li_{0.167}La_{0.61}TiO_3$ LLTO perovskite could be shown as following Equation 11:

$$\begin{aligned} &2.5Li_2TiO_3 + 1.5Li_4Ti_5O_{12} + 7.5La_2Ti_2O_7 \\ &\rightarrow 1.364Li_3La_{11}Ti_{18}O_{54} + 2.545Li_2O + 0.455Li_4TiO_4 \end{aligned} \quad \text{(Eq. 11)}.$$

Further, a $Li_6La_{10}Ti_{18}O_{54}$ model was built to simulate $Li_{0.33}La_{0.56}TiO_3$ with a lower La:Ti ratio as the main reaction product. In this case, the reaction of the most stable combination of compounds reacting into $Li_{0.33}La_{0.56}TiO_3$ could be shown as following Equation 12:

$$\begin{aligned} &2.5Li_2TiO_3 + 1.5Li_4Ti_5O_{12} + 7.5La_2Ti_2O_7 \\ &\rightarrow 1.39Li_6La_{10}Ti_{18}O_{54} + 1.33Li_2O + 0.556La_2O_3 \end{aligned} \quad \text{(Eq. 12)}.$$

As presented in the previous experimental chapters, a Ti-deficient LLTO perovskite would form via the precursor RP-type phase, given the stoichiometry of La:Ti for the $Li_{0.33}La_{0.56}TiO_3$ perovskite and the RP-type phase are 5:9 and 3:5, respectively. Tanaka et al. (2003) reported that charge-compensating vacancies could form in perovskite material more easily compared to only cation vacancies in a reducing environment [251]. Therefore, with the Ti deficiency and the excess Li in the precursor RP-type phase, the vacancies created in the Ti-deficient LLTO model should follow Ti:O = 1:2 ratio. To mimic the Ti-deficient LLTO perovskite, a LLTO perovskite supercell model with La:Ti = 10:17 stoichiometry was created, in which a Ti vacancy and two corresponding O vacancies to maintain the charge neutrality were created based on the pristine $Li_6La_{10}Ti_{18}O_{54}$ model. The formation energy of the Ti- and O-deficient $Li_{0.33}La_{0.56}TiO_3$ perovskite was calculated with the $Li_6La_{10}Ti_{17}O_{52}$ model, which was one of the main reaction products. For such a case, according to mass conservation, the most stable reaction products would be 1.47 $Li_6La_{10}Ti_{17}O_{52}$ + 1.088Li_2O + 0.147La_2O_3, as shown in Equation 13:

$$\begin{aligned} &2.5Li_2TiO_3 + 1.5Li_4Ti_5O_{12} + 7.5La_2Ti_2O_7 \\ &\rightarrow 1.47Li_6La_{10}Ti_{17}O_{52} + 1.088Li_2O + 0.147La_2O_3 \end{aligned} \quad \text{(Eq. 13)}.$$

On the other hand, the other main reaction product is the $Li_2La_2Ti_3O_{10}$ RP-type phase. For such a case, the most stable reaction products would be 5.5 $Li_2La_2Ti_3O_{10}$ + 4.5TiO_2 + 2 $La_2Ti_2O_7$, as shown in Equation 14:

$$2.5Li_2TiO_3 + 1.5Li_4Ti_5O_{12} + 7.5La_2Ti_2O_7 \rightarrow 5.5Li_2La_2Ti_3O_{10} + 4.5TiO_2 + 2La_2Ti_2O_7 \quad \text{(Eq. 14)}.$$

Combining Equations 11, 12, and 13 with the reaction 14, reaction energies of the $Li_2La_2Ti_3O_{10}$ to different LLTO perovskite phases can be determined, including $Li_{0.167}La_{0.61}TiO_3$ ($Li_3La_{11}Ti_{18}O_{54}$), $Li_{0.33}La_{0.56}TiO_3$ ($Li_6La_{10}Ti_{18}O_{54}$), and Ti- and O-deficient $Li_{0.33}La_{0.56}TiO_3$ ($Li_6La_{10}Ti_{17}O_{52}$):

$$5.5Li_2La_2Ti_3O_{10} + 4.5TiO_2 + 2La_2Ti_2O_7 \rightarrow 1.364Li_3La_{11}Ti_{18}O_{54} + 2.545Li_2O + 0.455Li_4TiO_4 \quad \text{(Eq. 15)}$$

Reaction energy = 3.86 eV

$$5.5Li_2La_2Ti_3O_{10} + 4.5TiO_2 + 2La_2Ti_2O_7 \rightarrow 1.39Li_6La_{10}Ti_{18}O_{54} + 1.33Li_2O + 0.56La_2O_3 \quad \text{(Eq. 16)}$$

Reaction energy = 3.52 eV

$$5.5Li_2La_2Ti_3O_{10} + 4.5TiO_2 + 2La_2Ti_2O_7 \rightarrow 1.47Li_6La_{10}Ti_{17}O_{52} + 1.088Li_2O + 0.147La_2O_3 \quad \text{(Eq. 17)}$$

Reaction energy = 6.53 eV

The positive energies of reactions 15, 16, and 17 indicate that $Li_2La_2Ti_3O_{10}$ is the most stable phase at 0 K (low temperatures). The formation of $Li_{0.33}La_{0.56}TiO_3$ perovskite becomes more favorable during high-temperature heat treatment considering the Li and O loss according to the Le Chatelier principle, which matches well with the other experimental results. Furthermore, the lower reaction energy of the $Li_{0.33}La_{0.56}TiO_3$ perovskite (3.52 eV) as compared to the $Li_{0.167}La_{0.61}TiO_3$ (3.86 eV) and Ti- and O-deficient $Li_{0.33}La_{0.56}TiO_3$ (6.53 eV) indicates that direct crystallization of $Li_{0.33}La_{0.56}TiO_3$ is preferential compared to LLTO perovskites with other La:Ti ratios. The stoichiometric LLTO therefore forms prior to the Ti- and O- deficient LLTO, which starts to form when there is insufficient neighboring Ti in the recrystallization front.

All phases should exhibit similar electronic conductivity, as the Ti and O vacancies in the Ti- and O-deficient LLTO resemble a Schottky defect in TiO_2 [252], where these vacancies do not introduce an extra electron. A band gap for $Li_{0.33}La_{0.56}TiO_3$, $Li_{0.167}La_{0.61}TiO_3$, and Ti- and O-deficient $Li_{0.33}La_{0.56}TiO_3$, calculated from the density of states (DOS), were 1.67 eV, 1.92 eV, and 1.96 eV, respectively (Figure 4.29).

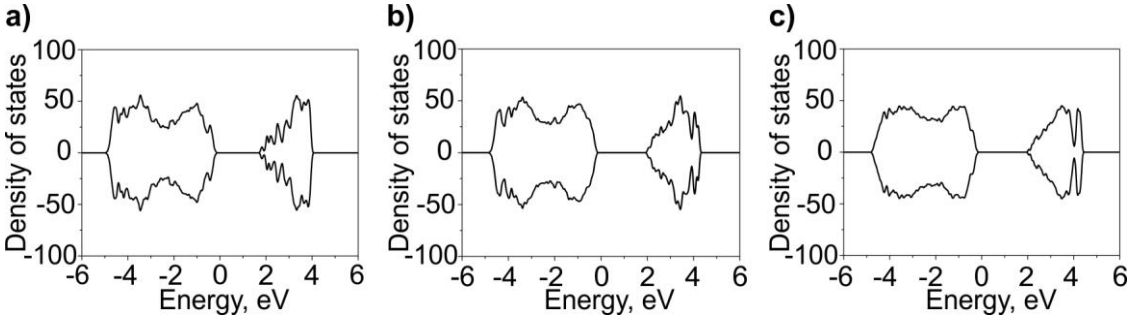

Figure 4.29: The density of states for (a) $Li_{0.33}La_{0.56}TiO_3$, (b) $Li_{0.167}La_{0.61}TiO_3$, and (c) Ti- and O-deficient $Li_{0.33}La_{0.56}TiO_3$.

Band gap values below 3 eV are typical for semiconductor materials. This suggests that under certain conditions, such as elevated temperatures or high applied voltages, LLTO could exhibit some degree of electronic conductivity, which may result in leakage current.

4.3.2.2 Experimental verification

Additional experiments were performed to support the DFT calculation results and verify the early formation of $Li_2La_2Ti_3O_{10}$ during the microstructure development of the LLTO samples with a higher La:Ti ratio. These experiments also aimed to understand the transient behavior of planar defects at elevated temperatures.

The abundant formation of plate-like grains during the initial stages of grain growth was confirmed after sintering of calcined LLTO powder with initial La:Ti=0.605 at 1100 °C (Figure 4.30a). These plate-like grains with lengths up to 50 µm and thickness up to 10 µm are disorderly arranged and intersect with one another. Small and spherical grains that are almost impossible to distinguish partially fill the space between the thin anisotropic grains (marked with arrows in Figure 4.30b). The presence of periodic or non-periodic $Li_2La_2Ti_3O_{10}$ sequences would require further validation with STEM analysis. However, due to the small grain size and porous microstructure, the sample is unsuitable for TEM preparation.

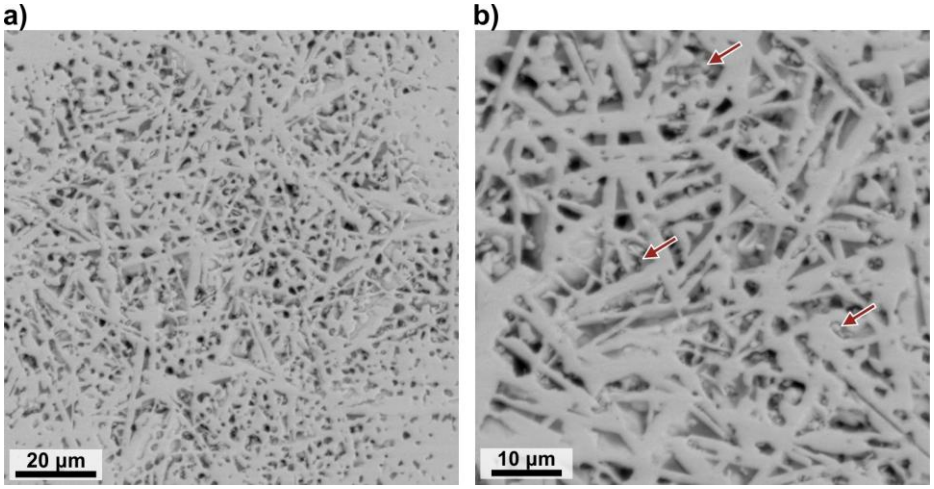

Figure 4.30: (a,b) Etched microstructure of sample with La:Ti=0.605 after sintering at 1100 °C.

After sintering at 1200 °C, the microstructure consists of thicker plate-like grains surrounded by smaller matrix LLTO grains with sizes up to 5 µm (Figure 4.31). The lamellae are present in almost every grain. This structure is similar to that of the sample sintered at 1250 °C, with the primary difference being that the plate-like grains formed at the lower temperature are thinner, while the lamellae in the anisotropic and smaller isotropic LLTO grains appear more pronounced. The reduced presence of lamellae in the sample sintered at 1250 °C suggests that recrystallization of these structures begins at this temperature.

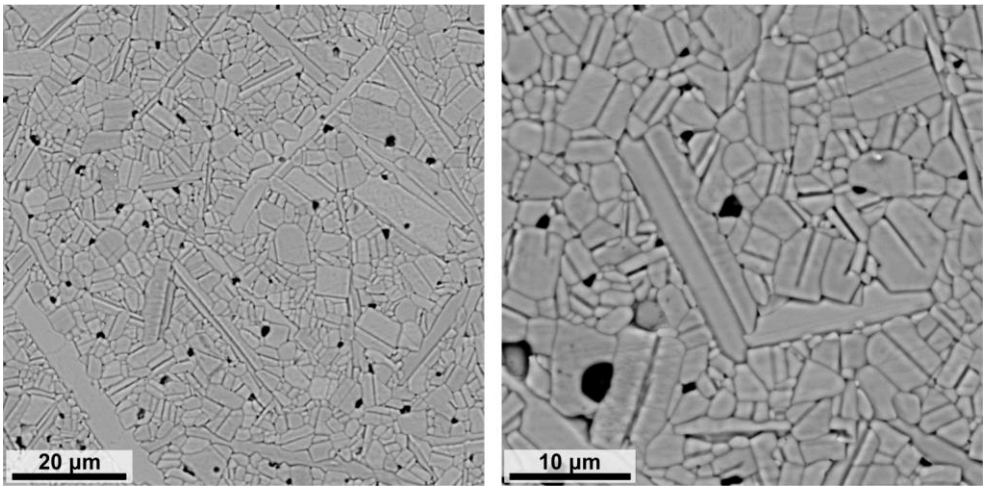

Figure 4.31: Etched microstructure of sample with La:Ti=0.605 after sintering at 1200 °C.

Thermal instability and recrystallization of the lamellae were further observed after subsequent etching of the sample with La:Ti=0.605 sintered at 1250 °C for 15 min (Figure 4.32a). The microstructure of the sample shows significant changes in comparison to the original characteristics. The previously sharp edges of the anisotropic grains become wavy, indicating the onset of the recrystallization process. The lamellae, which were initially prominent, become less visible and would probably slowly disappear after a longer etching procedure.

After sintering at temperatures above 1250 °C, the lamellae within smaller LLTO grains completely recrystallize and disappear (Figure 4.32b). The exaggeratedly grown plate-like grains transform into isometric grains with sizes of around 50 µm, while the surrounding matrix grains show minimal growth. This suggests that the presence of lamellae and also their recrystallization are very sensitive to thermal conditions and are limited to a very narrow temperature range.

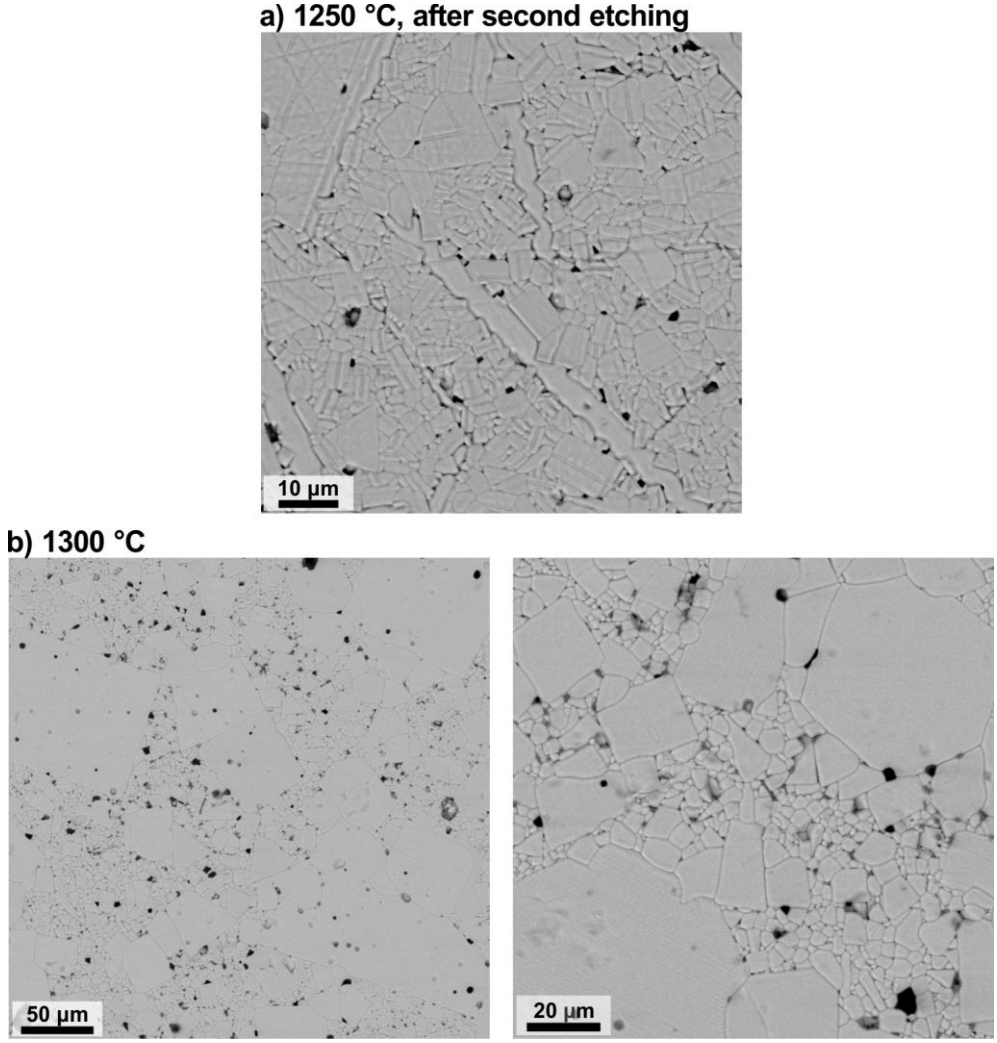

Figure 4.32: (a) BSE SEM image of the sample with La:Ti=0.605 sintered at 1250 °C after two subsequent thermal etching treatments. (b) Etched microstructure after sintering at 1300 °C.

Furthermore, the sample with the highest initial La:Ti ratio of 0.622 was prepared at a lower temperature to investigate whether the coarse-grained microstructure after sintering at 1350 °C is related to the formation of lamellae during the early stages of the grain growth.

The microstructure of the sample with La:Ti=0.622 sintered at 1100 °C is poorly developed and porous. However, very thin anisotropic grains (marked with arrows in Figure 4.33a), are present within the fine-grained microstructure. After sintering at 1200 °C, the microstructure consists of small grains with sizes up to 10 µm, each intersected with a lamella (Figure 4.33b). This indicates that the formation of lamellae is shifted to lower temperatures with increasing starting La:Ti ratio. Since lamellae are absent already after sintering at 1250 °C, the recrystallization also occurs at lower temperatures.

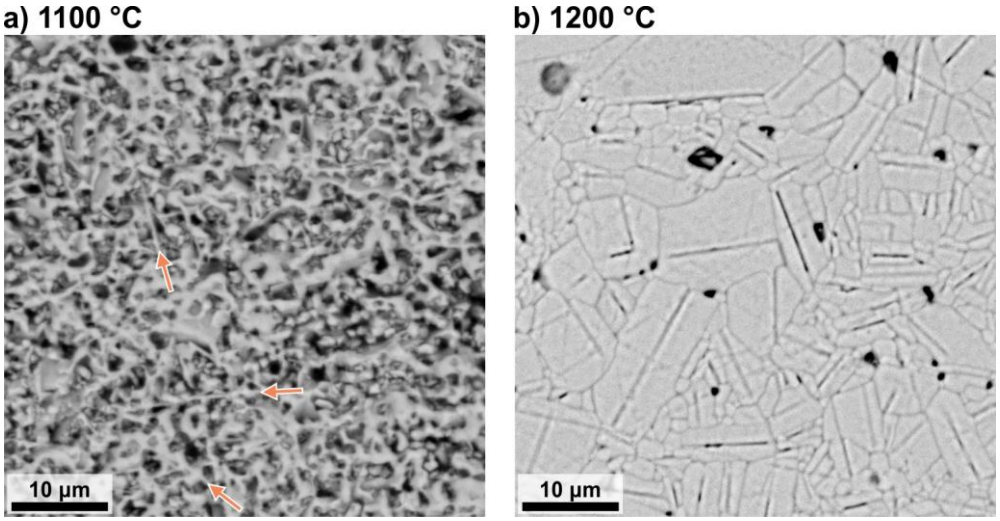

Figure 4.33: Thermally etched microstructure of sample La:Ti=0.622 after sintering at (a) 1100 °C and (b) 1200 °C.

The results show that the RP-type defects form at lower temperatures than the LLTO grains, which is consistent with the DFT calculations. The formation and later decomposition of lamellae occur at lower temperatures in compositions with a higher La:Ti ratio. It is likely that the sample with La:Ti=0.589 contains single RP-type defects with structural elements of the $Li_2La_2Ti_3O_{10}$ phase, as those reported by Zhu et al. (2020) [136] and Peng et al. (2022) [141].

4.3.3 Conclusions

The main findings of the third part of the study are:

- in compositions with sufficient excess of La and Li, the $Li_2La_2Ti_3O_{10}$ phase forms at lower temperatures, before the LLTO phase,
- the amount of $Li_2La_2Ti_3O_{10}$ phase depends on the initial La- and Li-excess,
- higher La:Ti ratio lowers the temperature for formation and recrystallization of RP-type defects,
- the $Li_2La_2Ti_3O_{10}$ phase is thermally unstable and recrystallizes to LLTO, which limits its presence to a very narrow temperature range,
- progressive and topotaxial recrystallization begins with ion exchange within the non-periodic RP-type lamellae,
- RP-type lamellae can recrystallize directly into LLTO or by forming an additional lattice plane.

4.4 Microstructure Development Under the Influence of RP-Type Defects

The microstructure development in LLTO is a complex process, mainly dominated by three processes; exaggerated grain growth, oriented or topotaxial recrystallization, and coarsening. Exaggerated growth occurs in the initial stages of the grain growth and is related to the crystallization of grains of the $Li_2La_2Ti_3O_{10}$ phase or grains that contain non-periodic sequences of the RP-type defects which are structurally related to the $Li_2La_2Ti_3O_{10}$ phase. Due to the thermal instability of the $Li_2La_2Ti_3O_{10}$ phase, these sequences recrystallize to LLTO and in the final stage, the microstructure coarsens according to the Ostwald ripening. The main stages of the microstructure development are described in detail in continuation.

4.4.1 Stage 1: Development of plate-like seed grains

Preparation of coarse-grained LLTO starts with calcination of LLTO with Li:La:Ti ratio 11:15:25 at 800 °C for 8 hours. The calcined powder is fine-grained and with homogeneous distribution of La and Ti (Figure 4.34a). After sintering at 1100 °C, the microstructure development starts with the formation of thin plate-like grains in the matrix of fine-grained LLTO grains (Figure 4.34b).

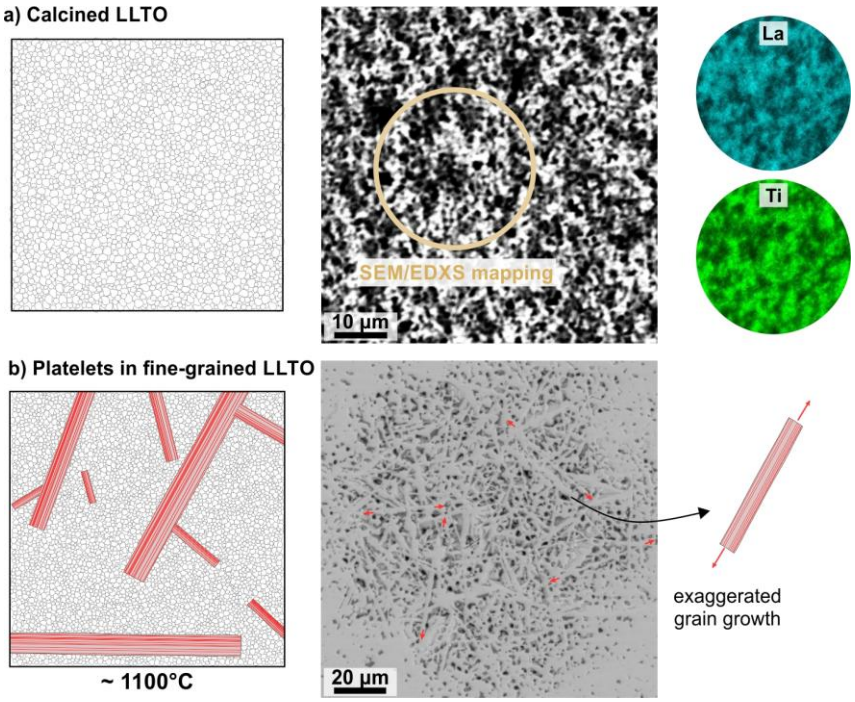

Figure 4.34: (a) Calcined LLTO powder. (b) Grain growth starts with the development of large anisotropically developed plate-like grains.

According to the results of DFT calculations and STEM analyses after sintering at 1250 °C, these anisotropically developed grains consist predominantly of $Li_2La_2Ti_3O_{10}$ phase (n=2) and non-periodic sequences of RP-type defects separated by perovskite blocks with variable thicknesses (n~2-5). Such anisotropic grain growth is typical for unconstrained growth of phases with a layered structure like the $Bi_4Ti_3O_{12}$ Aurivillius phase [253], which

has a similar crystal structure as $Li_2La_2Ti_3O_{10}$. First-principles calculations have shown that the formation of the $Li_2La_2Ti_3O_{10}$ phase is also energetically more favorable at lower temperatures compared to the LLTO perovskite. Therefore, microstructure development starts with the crystallization of $Li_2La_2Ti_3O_{10}$ due to excess La and Li that shifts the phase equilibrium towards the $Li_2La_2Ti_3O_{10}$ phase.

In further microstructure development, these large anisotropic plate-like grains act as seed grains for the growth of large LLTO grains. The formation of plate-like grains with modulated structure depends on the excess amounts of Li and La and the heating regime. The applied conditions seem to be optimal for the development of large seed grains in the sample with La:Ti ratio of 0.605 and 20 mol% of Li excess. Similar microstructure development was also observed at slightly lower temperatures for the sample with the highest La:Ti ratio of 0.622. This indicates that the formation of the RP-type sequences in LLTO is a delicate balance between the composition, i.e. the starting La:Ti ratio, Li_2CO_3 excess, and sintering temperature.

4.4.2 Stage 2: Crystallization of LLTO

With increasing sintering temperature and depletion of excess Li and La, that incorporate into the exaggeratedly grown plate-like grains with a crystal structure of $Li_2La_2Ti_3O_{10}$ phase in the first stage, microstructure development continues with preferential crystallization of LLTO perovskite (Figure 4.35). It is likely that the first and second stages of microstructure development partially overlap.

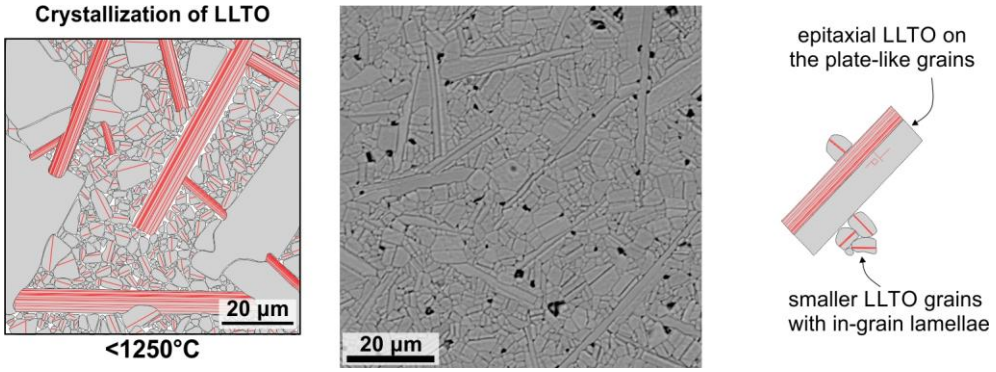

Figure 4.35: Crystallization of large LLTO grains epitaxially on the seed grains and as smaller grains with in-grain lamellae between the large grains.

For LLTO, it is energetically most favorable to grow epitaxially on the large plate-like grains (seeds) due to the close structural relationship between the phases. Due to the length of the seed grains, large LLTO areas are formed. This leads to the development of large anisotropic plate-like grains with lengths that sometimes exceed 100 µm. The LLTO grains have La:Ti ratio of 0.58 (LLTO with x=0.09) and, according to STEM analyses, contain single RP-type defects in all equivalent pseudocubic directions, especially in proximity to the contact with the seed grains with modulated structure. The seed grains with crystal structure close to the $Li_2La_2Ti_3O_{10}$ phase (La:Ti ratio of 0.67) exhibit slightly brighter contrast in the BSE SEM images than the epitaxial LLTO and the surrounding smaller grains. The enrichment with Li and La in the large plate-like seed grains was confirmed by LA-ICP-MS.

In addition to the large LLTO grains that grow epitaxially on the seed grains, the crystallization of smaller LLTO grains is observed. The characteristic of these grains is

that almost all contain an internal lamella composed of non-periodic RP-type defects. These defects form as a result of smaller La and Li excess after most of excess La and Li was used for the crystallization of the large seed grains. Characteristics of exaggerated grain growth were observed also in these grains, for example, the internal lamellae grow faster than the matrix LLTO and penetrate into the surrounding grains (Figure 4.16).

This type of microstructure development was described as polytype-induced grain growth in other perovskites and oxides, where the formation of planar defects with locally different atomic structure and chemical composition is observed, *e.g.* BaO-doped $CaTiO_3$ [169], $BaTiO_3$ sintered in reducing atmosphere [159], SrO-doped $SrTiO_3$ [166], and ZnO doped with SnO_2, TiO_2 or Sb_2O_3 [160]. The characteristic of exaggerated growth of grains with inherent planar defects is that these grains grow until they collide with other equivalent grains, then their growth is stopped. This effect is observed in the large plate-like grains as well as in the small LLTO grains with thin in-grain lamellae.

If the grains with the RP-type defects did not form, all grains in the microstructure would develop into grains with uniform grain size and isometric morphology, as observed in samples with stoichiometric compositions for $Li_{0.33}La_{0.56}TiO_3$ perovskite.

4.4.3 Stage 3: Recrystallization of RP-type defects

The microstructure after sintering at 1250 °C exhibits bimodal grain size distribution, consisting of large plate-like grains with many RP-type defects, some with epitaxially overgrown LLTO perovskite, and many small LLTO grains with thinner RP-type lamellae. Around this temperature, the RP-type defects in all grains, the large and the small ones, become unstable and start to recrystallize to LLTO perovskite as described in Chapter 4.3.

The formation of plate-like grains and lamellae with RP-type defects is limited to temperatures below 1250 °C and represents the intermediate stage between the fine-grained starting powder and the final coarse-grained LLTO. The recrystallization of the defects occurs in a very narrow temperature range and after sintering at temperatures above 1250 °C, the RP-type defects are not present anymore (Figure 4.36).

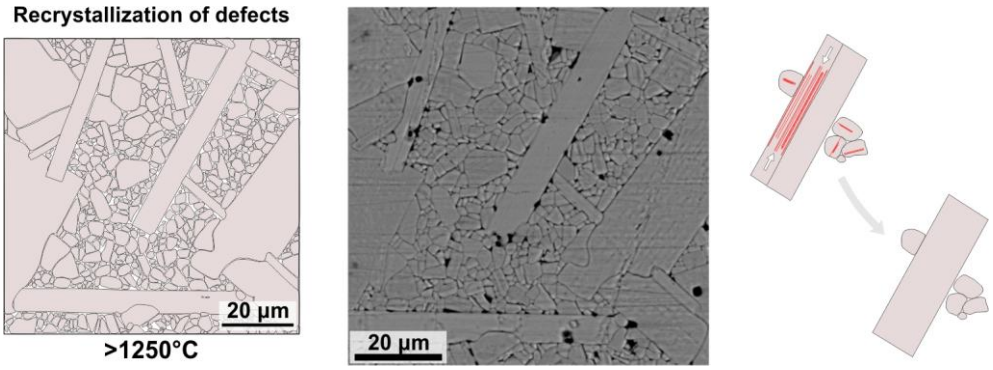

Figure 4.36: Recrystallization of RP-type sequences to LLTO. When this process is completed, all grains, the large and the small ones, are LLTO perovskite.

The recrystallization of the RP-type defects in LLTO is unlike other Ruddlesden-Popper phases (for example in $SrTiO_3$ [166], [254]) that are thermally stable and do not recrystallize at the applied sintering temperatures. If the defects in LLTO remained intact, the bimodal microstructure observed after sintering at 1250 °C would not recrystallize further. The process of oriented recrystallization of RP-type defects to LLTO via ion exchange inside the RP layers (Li-rich layers) results in the disappearance of the RP-type

sequences and crystallization of all grains to LLTO perovskite. The main consequence of this process is that the grains lose their reinforcement and become normal LLTO grains without planar defects. When this process is finished, the microstructure consists only of grains of the same type (LLTO), which have two significantly different sizes and morphologies (bimodal grain size distribution). This stage of microstructure development is crucial for further recrystallization to coarse-grained ceramics.

4.4.4 Stage 4: Coarsening via Ostwald ripening

After recrystallization of the RP-type sequences, the microstructure is composed of very large faceted plate-like LLTO grains, which are surrounded by smaller LLTO grains. The large grains have an incomparably larger radius of curvature than the smaller grains. The existence of the same type of grains with very different curvature triggers further recrystallization via the Ostwald ripening mechanism (Figure 4.37). This process leads to the development of a final microstructure comprised of large LLTO grains, some measuring up to 250 µm in diameter.

Since recrystallization of the larger seed grains may take longer than the recrystallization of the smaller grains, the processes of recrystallization of the RP-type defects and recrystallization of the smaller grains onto the seed grains may overlap.

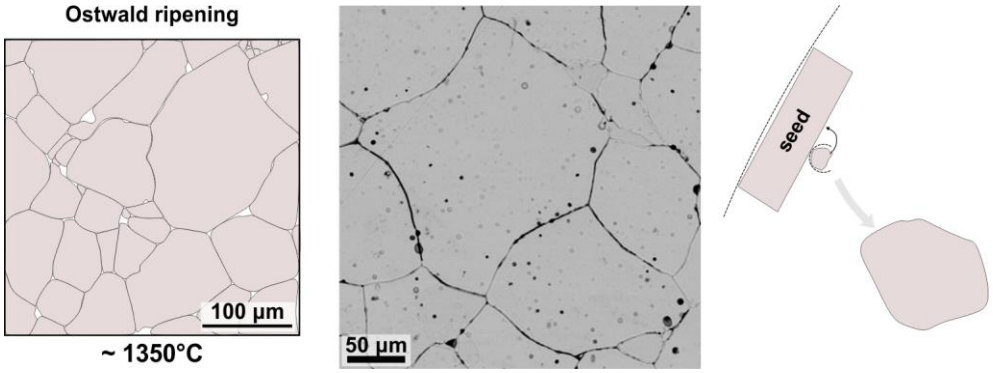

Figure 4.37: Stage 4 of the LLTO grain growth and formation of coarse-grained LLTO ceramics.

According to SEM/EDS analyses, the grains have a homogeneous La:Ti ratio of around 0.6, which is close to the ratio in the starting powder. This implies a complete recrystallization of regions with different La:Ti ratios, also the Ti-deficient regions that form during the recrystallization of the RP-type lamellae, to LLTO during prolonged sintering at 1350 °C.

The coarse-grained microstructure that develops after sintering at 1350 °C due to the presence of RP-type defects at lower temperatures contains a much lower fraction of grain boundaries. This so-called self-seeded microstructure development represents an alternative approach to the formation of coarse-grained LLTO ceramics.

4.4.5 Conclusions

The main findings of the fourth part of the study are:

- in LLTO ceramics with La:Ti ratio of 0.60 and excess Li, plate-like grains composed of the $Li_2La_2Ti_3O_{10}$ phase and structurally related modulated non-periodic sequences preferentially form in the initial grain growth stage,
- plate-like grains exhibit exaggerated growth along the RP-type layers,
- at higher sintering temperatures, LLTO perovskite forms epitaxially on the plate-like grains and as smaller grains with thinner non-periodic in-grain lamellae,
- at around 1250 °C, the RP-type sequences become thermally unstable and gradually recrystallize to LLTO perovskite,
- large LLTO grains act as seeds for further recrystallization by Ostwald ripening,
- the final microstructure consists of very large LLTO grains and contains a lower fraction of grain boundaries.

The process of the microstructure development in LLTO with an initial La:Ti ratio of 0.605 and excess of Li is schematically presented in Figure 4.38.

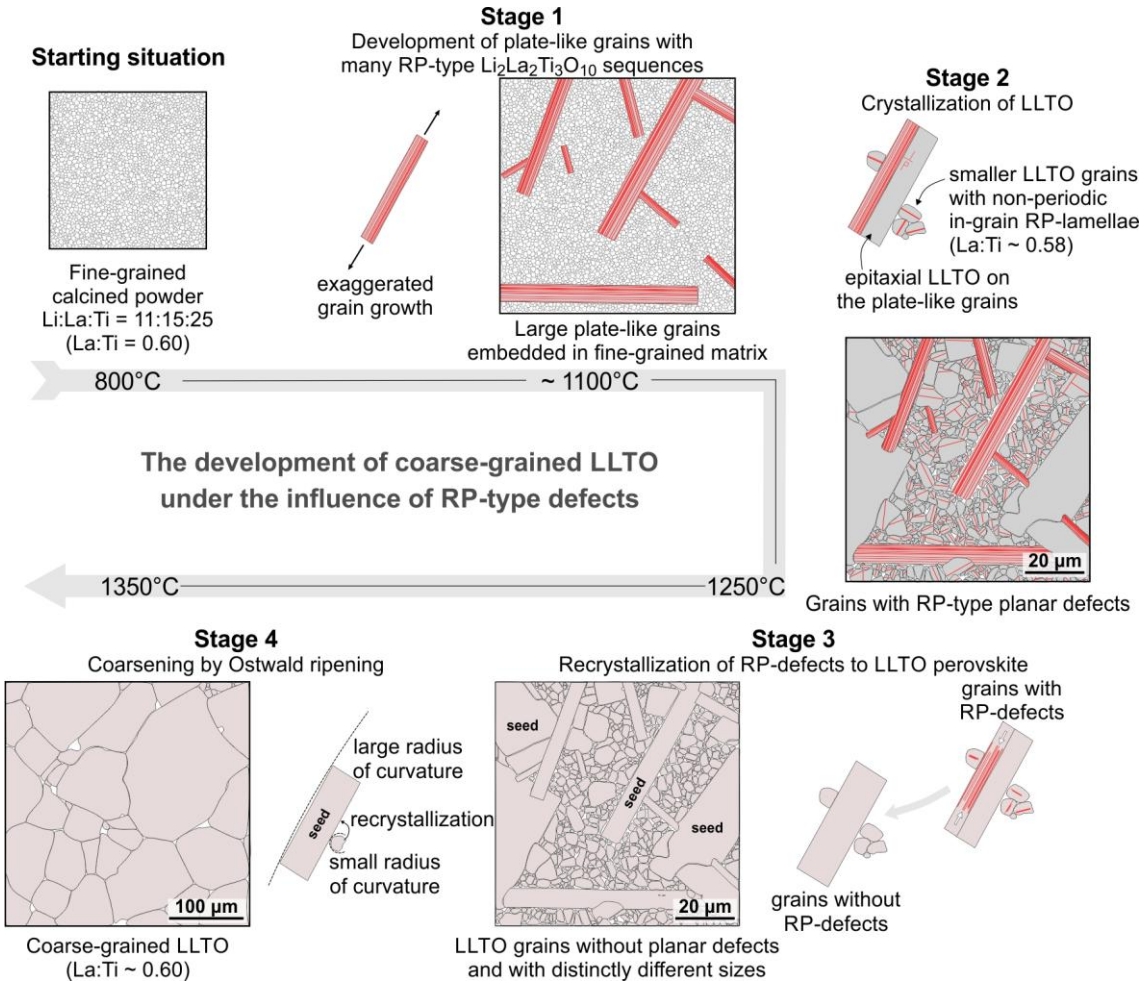

Figure 4.38: Schematic presentation of stages during microstructure development of coarse-grained LLTO ceramics under the influence of RP-type defects.

4.5 Ionic Conductivity of LLTO Ceramics

While ceramic samples of LLTO sintered at 1250 °C are suitable for studying the microstructure development and its specifics, these samples are not applicable as an electrolyte since the microstructure is not completely developed and/or the ceramics is porous and not sufficiently dense. For these reasons, ionic conductivity at room temperature determined by impedance spectroscopy was measured in the samples with fully developed microstructures composed of LLTO grains after sintering at 1350 °C. Samples after slow cooling and quenching were compared.

4.5.1 Impedance measurements

Generally, Nyquist plots of the LLTO impedance spectra consist of two depressed semicircles and a straight line at lower frequencies, which represents the behavior of the electrodes. The semicircle at high frequencies with a frequency range of 32 MHz to 100 kHz corresponds to the contribution of the bulk (grains) and the second semicircle extending to as low as 1 Hz corresponds to the contribution of grain boundaries. Such spectra are frequently modeled with an equivalent circuit consisting of a series of parallel combinations of a resistor (R) and a constant phase element (CPE), where these R-CPE combinations describe the depressed semicircles in the Nyquist plot. One of the more commonly used models consists of two R-CPE circuits and a CPE (precise notation ($R_{bulk}CPE_{bulk}$)($R_{grain\ boundary}CPE_{grain\ boundary}$)($CPE_{electrode}$)) (Figure 4.39).

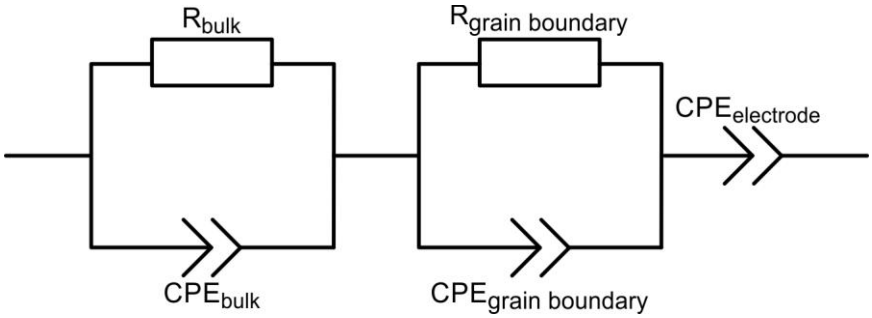

Figure 4.39: Schematics of ($R_{bulk}CPE_{bulk}$)($R_{grain\ boundary}CPE_{grain\ boundary}$)($CPE_{electrode}$) equivalent circuit used as a fitting model for LLTO impedance spectra.

CPE elements describe the non-ideal capacitive contributions for the experimental data. CPE_{bulk} represents the grain interior contribution, $CPE_{grain\ boundary}$ (CPE_{gb}) is the contribution of grain boundaries, and $CPE_{electrode}$ (CPE_{el}) describes the blocking behavior of the Au-sputtered electrodes. This model was used as a baseline fitting model for the impedance spectra and determination of ionic conductivity values for LLTO samples. The fitting parameters used for LLTO samples are given in Table 4.5.

Table 4.5: Fitting parameters for the LLTO samples using the ($R_{bulk}CPE_{bulk}$)($R_{gb}CPE_{gb}$)(CPE_{el}) equivalent circuit model.

	R bulk	**CPE bulk -T**	**CPE bulk -P**	**R gb**	**CPE gb -T**	**CPE gb -P**	**CPE el -T**	**CPE el -P**
La:Ti=0.560	1074	$9.695 \cdot 10^{-10}$	0.78225	15995	$3.5795 \cdot 10^{-8}$	0.88701	$4.149 \cdot 10^{-6}$	0.57705
La:Ti=0.560 Q	974.9	$4.2858 \cdot 10^{-8}$	0.56434	8552	$5.5108 \cdot 10^{-8}$	0.90318	$4.103 \cdot 10^{-6}$	0.61742
La:Ti=0.589	1203	$1.039 \cdot 10^{-9}$	0.79964	10504	$3.8248 \cdot 10^{-8}$	0.94506	$2.3205 \cdot 10^{-7}$	0.77841
La:Ti=0.589 Q	678.7	$4.1967 \cdot 10^{-8}$	0.59839	939	$4.8819 \cdot 10^{-7}$	0.8586	$3.7531 \cdot 10^{-6}$	0.74289
La:Ti=0.605	3001	$4.096 \cdot 10^{-10}$	0.86024	1866	$1.1546 \cdot 10^{-6}$	0.72941	$1.1852 \cdot 10^{-6}$	0.72045
La:Ti=0.605 Q	1907	$2.885 \cdot 10^{-10}$	0.87568	10855	$2.9218 \cdot 10^{-7}$	0.78061	$1.6456 \cdot 10^{-6}$	0.76837
La:Ti=0.622	3665	$2.595 \cdot 10^{-9}$	0.72999	2059	$5.936 \cdot 10^{-7}$	0.7222	$2.7038 \cdot 10^{-7}$	0.82699
La:Ti=0.622 Q	2713	$2.930 \cdot 10^{-10}$	0.86474	3808	$6.2913 \cdot 10^{-7}$	0.74217	$1.1537 \cdot 10^{-6}$	0.6411

Although ($R_{bulk}CPE_{bulk}$)($R_{gb}CPE_{gb}$)(CPE_{el}) equivalent circuit model describes the experimental results sufficiently well, the fitted data provided a better match in the mid-frequency part of the spectra than in the high-frequency part, especially for the slowly cooled and quenched samples with La:Ti=0.560 and La:Ti=0.589 (Figure 4.40). In these samples, a 45 ° slope is present at high frequencies, which transitions into a depressed bulk grain semi-circular contribution.

Such features are not typically observed in the impedance spectra of LLTO solid electrolytes, however, they are commonly found in impedance spectra of bulk lithium-ion systems with liquid electrolytes [255], [256], [257]. It is unclear whether this feature that manifests only for samples with La:Ti ratio of 0.560 and 0.589, and to a lesser extent for sample La:Ti=0.622, is an inherent characteristic of the studied system or a measurement artifact. This behavior could also be influenced by the geometry of the measured pellet, which may not be perfectly planar. As reported by Braun et al. (2017) [258], the bulk grain contribution in some cases separates into two different sub-contributions, for instance, due to minor stoichiometric differences between larger and smaller grains, which could also be the case in LLTO samples that have a complex and non-uniform structure and differ in the presence of secondary phases and especially in the average grain size. Improved goodness of fit might be achieved by using an equivalent circuit model with three R-CPE circuits and a CPE (the additional R-CPE being the result of another bulk grain contribution), however, as the literature on impedance analysis of similar materials using such a model is rather limited, the goodness of fit could not be verified and therefore the latter model is not necessary an appropriate choice for modeling the behavior of LLTO samples. More accurate determination of the electrical response of grains and grain boundaries would be possible by using microelectrodes [259].

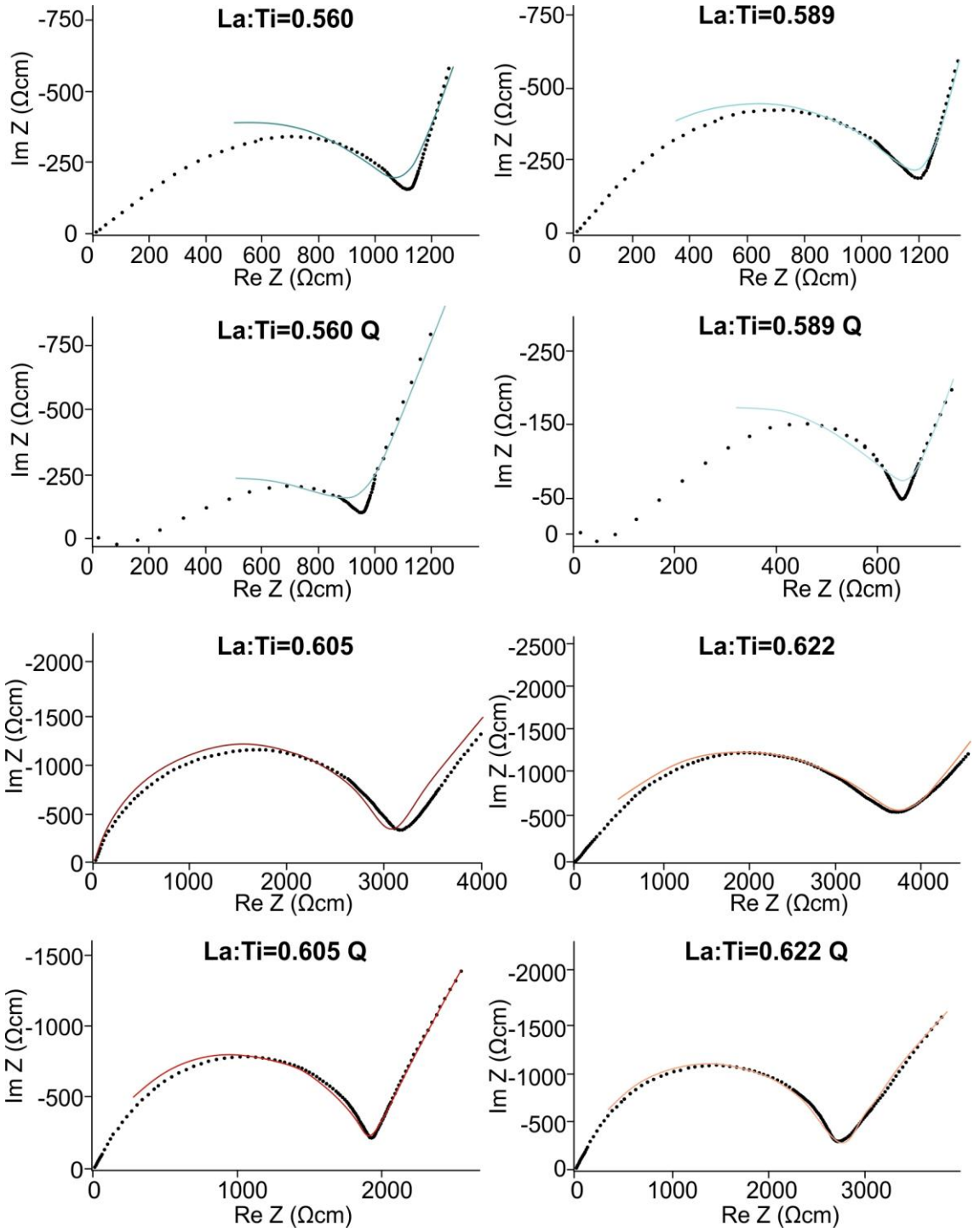

Figure 4.40: Comparison of experimental data (black dots) with 2 R-CPE – CPE model fitting results for the high-frequency portion of impedance spectra.

4.5.2 Ionic conductivity of LLTO samples

For all measured samples, the first semicircle, used for the determination of the bulk (grain) conductivity σ_{bulk}, was clearly defined (inset in Figure 4.41). The grain ionic conductivities of all prepared samples are similar and in the range from 10^{-3} to 10^{-4} S/cm. The highest grain conductivity was measured for samples La:Ti=0.560 and La:Ti=0.589 with the smallest grain size and predominately pseudocubic LLTO modification. Samples with a

higher fraction of the tetragonal phase (La:Ti=0.605 and La:Ti=0.622 after slow cooling) exhibit lower grain conductivity, which is in agreement with previous reports [45], [96], [260], [261], [262].

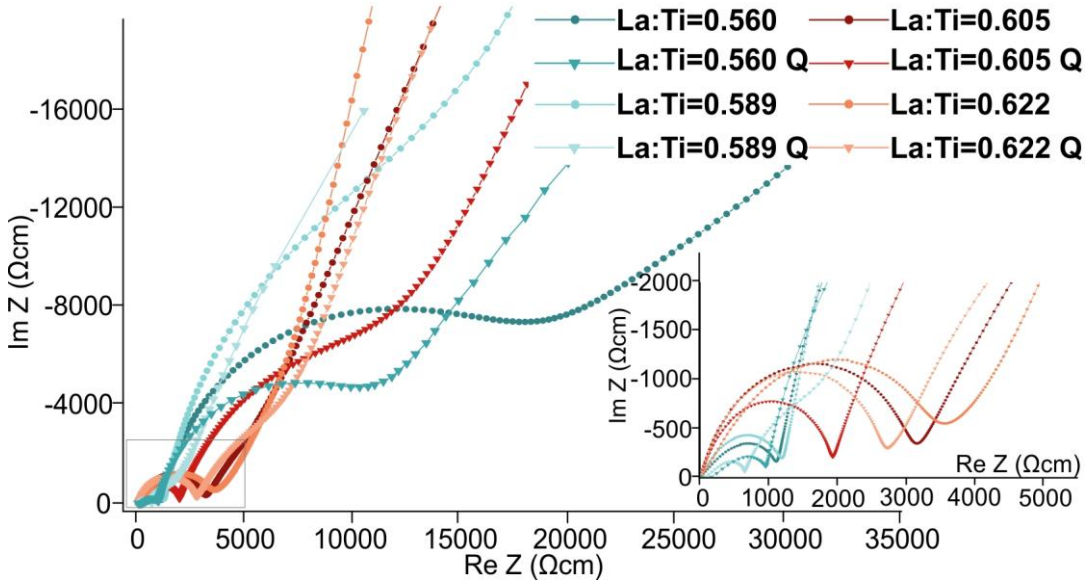

Figure 4.41: The impedance spectra for the samples sintered at 1350 °C and quenched samples. The insert shows the high-frequency semicircle.

In all compositions, quenching of the samples resulted in a slight improvement of grain conductivity due to the stabilization of the pseudocubic LLTO modification. The results agree with the previous finding that Li^+ mobility is enhanced in pseudocubic LLTO with x around 0.11 and disordered arrangement of A-site cations and vacancies [108], [262].

The second semicircle used for the determination of grain boundary conductivity σ_{gb} was well defined for the samples La:Ti=0.560, La:Ti=0.560 Q, La:Ti=0.589, La:Ti=0.605 Q, and La:Ti=0.622 Q, while it was much smaller and overlapped with the blocking contribution of the electrodes for the samples La:Ti=0.589 Q, La:Ti=0.605 and La:Ti=0.622 (Figure 4.41). The grain boundary conductivity σ_{gb} was determined from the R 3 fitting parameters. The sample with the smallest grain size, La:Ti=0.560, exhibits the lowest grain boundary conductivity (Table 4.6), and hence, this sample also has the lowest total ionic conductivity due to the highest contribution of the grain boundaries. The obtained values for grain boundary conductivity for the samples La:Ti=0.605 and La:Ti=0.622 were 5 to 10 times higher than those of the other samples. As these two samples also exhibit the largest grain size, these findings corroborate with the literature, which suggests an inversely proportional trend of decreasing grain boundary resistance with an increase in grain size [47], [263], [264]. Interestingly, the quenched sample with La:Ti=0.589 exhibits even higher values of grain boundary conductivity, despite its fine-grained microstructure and the presence of a small amount of secondary Ti-rich phases. This enhancement may be attributed to the rapid cooling from high sintering temperatures, which can lead to the formation of amorphous Ti-rich phases at the grain boundaries. As demonstrated by Madrid et al. (2024) [265], the presence of amorphous TiO_2 at triple junctions between LLTO grains can significantly enhance grain boundary conductivity, because the disordered interface facilitates fast diffusion of Li^+ ions, improving ionic transport across grain boundaries. STEM analysis of these samples should be performed to

confirm this. Samples with higher grain boundary conductivity σ_{gb} also exhibit the highest total conductivity σ_{total} in the range of 10^{-4} S/cm.

Table 4.6: Conductivities of grains (σ_{bulk}), grain boundaries (σ_{gb}), and total ionic conductivities (σ_{total}) of the samples with different starting compositions after sintering at 1350 °C (slowly cooled and quenched, Q) as determined from impedance measurements at 25 °C.

Sample	σ_{bulk} (S/cm)	σ_{gb} (S/cm)	σ_{total} (S/cm)
La:Ti=0.560	$9.31 \cdot 10^{-4}$	$6.25 \cdot 10^{-5}$	$5.86 \cdot 10^{-5}$
La:Ti=0.560 Q	$1.03 \cdot 10^{-3}$	$1.17 \cdot 10^{-4}$	$1.05 \cdot 10^{-4}$
La:Ti=0.589	$8.33 \cdot 10^{-4}$	$9.18 \cdot 10^{-5}$	$8.27 \cdot 10^{-5}$
La:Ti=0.589 Q	$1.47 \cdot 10^{-3}$	$1.06 \cdot 10^{-3}$	$6.18 \cdot 10^{-4}$
La:Ti=0.605	$3.33 \cdot 10^{-4}$	$5.36 \cdot 10^{-4}$	$2.05 \cdot 10^{-4}$
La:Ti=0.605 Q	$5.24 \cdot 10^{-4}$	$9.21 \cdot 10^{-5}$	$7.84 \cdot 10^{-5}$
La:Ti=0.622	$2.73 \cdot 10^{-4}$	$4.86 \cdot 10^{-4}$	$1.75 \cdot 10^{-4}$
La:Ti=0.622 Q	$3.69 \cdot 10^{-4}$	$2.63 \cdot 10^{-4}$	$1.53 \cdot 10^{-4}$

While this represents a modest enhancement, the observed increase in ionic conductivity brings the performance of these solid electrolytes closer to that of liquid electrolytes and highlights the potential of LLTO as a viable candidate for solid electrolytes in next-generation batteries.

4.5.3 Conclusions

The main findings of the final part of the study are:

- total ionic conductivity of LLTO ceramics is mainly influenced by composition, structural characteristics, and microstructural properties,
- bulk (grain) conductivity in LLTO strongly depends on the degree of ordering between La-rich and La-poor layers; disordered pseudocubic modification exhibits higher conductivities compared to the tetragonal LLTO,
- the grain conductivity of LLTO is in the range of 10^{-3} to 10^{-4} S/cm, regardless of the initial La:Ti ratio,
- grain boundary conductivity varies significantly depending on the LLTO microstructure; in LLTO ceramics with larger average grain sizes, the contribution of resistive grain boundaries is reduced.

Chapter 5

Conclusions

The research of solid electrolytes plays a crucial role in the development of next-generation energy storage devices. It is primarily focused on the improvement of key functional properties such as ionic conductivity, stability, and compatibility with other battery components. However, alongside improving the functional properties of the materials, understanding the underlying mechanisms and processes is equally important. Several challenges and knowledge gaps still persist in this field, hindering the large-scale practical application of solid electrolytes in batteries. This thesis investigates the structural and microstructural properties of lithium lanthanum titanate (LLTO), aiming to unveil the mechanisms of grain growth and explore the relationship between the synthesis parameters, (micro)structure, and final functional properties.

In this dissertation, an innovative approach for the preparation of coarse-grained LLTO ceramics, based on the initial La:Ti ratio, is described. While the stoichiometric LLTO sample exhibits normal grain growth and is composed of LLTO grains with uniform grain size in the range of 5 µm and Ti-rich secondary phases, increasing La:Ti ratio drastically affects the microstructure development. In LLTO ceramics with La:Ti ratio of 0.605 and excess Li, the microstructure development is primarily influenced by the formation of plate-like grains, composed of the RP-type $Li_2La_2Ti_3O_{10}$ phase and structurally related modulated sequences in the initial stage of the grain growth. Enrichment with Li and La in the plate-like grains was observed by LA-ICP-MS, while their early formation was confirmed by theoretical calculations. These grains exhibit exaggerated growth along the RP-type layers and develop into large anisotropic plate-like grains. The microstructure development continues with the crystallization of LLTO perovskite, epitaxially on the plate-like grains and in the form of smaller grains with La:Ti ratio of 0.58. Due to the small La and Li excess that is left after most was used for the crystallization of the large plate-like grains, smaller grains contain thin in-grain lamellae with non-periodic sequences of RP-type defects. These sequences are composed of RP-type defects and pseudo-perovskite blocks of LLTO with varying thicknesses.

At around 1250 °C, pronounced ion exchange occurs between the RP-type layers of the modulated sequences. Using quantitative multislice frozen-phonon simulations, it was estimated that at 1250 °C, up to 10% of La^{3+} and 20% of Ti^{4+} exchange Li^+ in the Li-rich RP layers. This leads to structural instability of defects and progressive transformation of RP-type defects to LLTO perovskite with a composition of $Li_{0.33}La_{0.56}TiO_3$, as confirmed by calculations based on the density functional theory.

Recrystallization is a complex process that includes the rearrangement of the La atoms from RP-type defects to the A-sites of the newly formed LLTO perovskite and diffusion of Li to the surrounding LLTO matrix. The large LLTO grains without defects act as seed grains for further recrystallization by Ostwald ripening, where the small grains recrystallize onto the large grains. The result of this process is coarse-grained ceramics with grains exceeding 100 µm in diameter.

Preparation of coarse-grained LLTO through self-seeded grain growth by using a higher La:Ti ratio in the initial LLTO composition is a novel finding that has not been previously reported in the literature. As the contribution of grain boundaries to the total conductivity is lower in the samples with larger average grain size, the coarse-grained LLTO ceramics exhibit total ionic conductivity in the range of 10^{-4} S/cm.

In this thesis, analysis of atomic-scale images using multi-slice frozen-phonon simulations provided deeper insights into the atomic-scale processes that influence the microstructure development of LLTO ceramics. While this approach is not commonly used, it offers valuable quantitative information on experimental HAADF-STEM images and can help elucidate the atomic-scale mechanisms that influence the material's structure and final functional properties. This expands the possibility for the development of solid electrolytes in next-generation energy storage applications.

Appendix

Table A.1: Average absolute intensities with relative deviations (in %) of the atomic layers comprising a RP-type defect in the predicted structural models with thickness (a) 30 nm, (b) 20 nm, and (c) 15 nm along [100] zone axis and experimental HAADF-STEM image of the non-periodic sequence. Intensity ratios $I_{La\text{-}C}$:$I_{La\text{-}E}$, I_{Li}:$I_{La\text{-}E}$, $I_{Ti\text{-}E}$:$I_{La\text{-}E}$, and $I_{Ti\text{-}C}$:$I_{La\text{-}E}$ are calculated for comparison of the experimental values with simulations.

a) 30 nm

Model	Absolute intensities ± relative std. deviation in %					Intensity ratios in %				Average absolute difference
	$I_{La\text{-}E}$	$I_{La\text{-}C}$	$I_{Li\text{-}La}$	$I_{Ti\text{-}E}$	$I_{Ti\text{-}C}$	$I_{La\text{-}C}$:$I_{La\text{-}E}$ Absolute difference to reference (experimental)	I_{Li}:$I_{La\text{-}E}$	$I_{Ti\text{-}E}$:$I_{La\text{-}E}$	$I_{Ti\text{-}C}$:$I_{La\text{-}E}$	
Only shift	21.9 ± 0.7	14.8 ± 6.2	2.6 ± 8.1	12.0 ± 0.7	12.2 ± 0.7	67.6	11.7	54.9	55.6	
						4.7	13.5	14.1	7.5	9.9
10La-10Ti	21.4 ± 4.6	15.6 ± 6.6	6.8 ± 15.9	11.8 ± 4.3	12.9 ± 1.0	73.2	31.7	55.4	60.4	
						0.9	6.5	14.6	12.2	8.6
20La-10Ti	19.2 ± 5.2	15.6 ± 6.2	10.6 ± 14.2	12.3 ± 3.8	12.9 ± 1.0	81.3	55.0	63.8	67.2	
						9.0	29.8	23.0	19.0	20.2
15La-15Ti	20.7 ± 6.5	15.6 ± 6.6	8.4 ± 11.9	11.5 ± 5.9	13.0 ± 1.1	75.5	41.0	55.3	62.5	
						3.2	15.9	14.6	14.3	12.0
10La-20Ti	20.9 ± 2.7	14.8 ± 6.4	7.1 ± 21.0	10.4 ± 4.7	12.2 ± 1.0	70.8	34.0	49.8	58.6	
						1.5	8.9	9.0	10.4	7.4
20La-20Ti	19.7 ± 8.3	15.6 ± 6.6	11.6 ± 14.5	11.3 ± 4.5	12.9 ± 1.2	79.4	59.0	57.3	65.6	
						7.1	33.9	16.6	17.4	18.7
Experimental	**4769 ± 6**	**3448 ± 10**	**1200 ± 12**	**1945 ± 6**	**2298 ± 5**	**72.3**	**25.2**	**40.8**	**48.2**	**Reference**

b) 20 nm

Model	Absolute intensities ± relative std. deviation in %					Intensity ratios in %				Average absolute difference
	$I_{La\text{-}E}$	$I_{La\text{-}C}$	$I_{Li\text{-}La}$	$I_{Ti\text{-}E}$	$I_{Ti\text{-}C}$	$I_{La\text{-}C}$:$I_{La\text{-}E}$	I_{Li}:$I_{La\text{-}E}$	$I_{Ti\text{-}E}$:$I_{La\text{-}E}$	$I_{Ti\text{-}C}$:$I_{La\text{-}E}$	
						Absolute difference to reference (experimental)				
Only shift	18.7 ± 0.8	12.7 ± 7.2	1.8 ± 8.0	8.9 ± 0.8	9.3 ± 0.8	68.0	9.4	47.6	49.6	
						4.3	15.8	6.8	1.5	7.1
10La-10Ti	18.1 ± 5.5	13.4 ±7.7	4.9 ± 26.3	8.6 ± 4.4	9.8 ± 1.0	74.3	27.1	47.7	54.1	
						2.0	1.9	7.0	5.9	4.2
20La-10Ti	16.3 ± 6.1	13.4 ± 7.2	8.2 ± 20.0	9.0 ± 4.5	9.8 ± 1.0	82.2	50.4	55.0	59.9	
						9.9	25.2	14.2	11.7	15.3
15La-15Ti	17.6 ± 6.2	13.4 ± 7.7	5.8 ± 19.9	8.3 ± 6.7	9.8 ± 1.6	76.0	32.7	47.0	55.8	
						3.7	7.5	6.2	7.6	6.3
10La-20Ti	**17.8 ± 4.1**	**12.7 ± 7.4**	**5.0 ± 25.4**	**7.6 ± 6.0**	**9.3 ± 0.9**	71.5	28.3	42.5	52.4	
						0.8	3.2	1.7	4.2	**2.5**
20La-20Ti	16.6 ± 9.1	13.4 ± 7.7	8.8 ± 18.3	8.2 ± 7.0	9.8 ± 1.2	80.8	53.2	49.4	59.1	
						8.5	28.1	8.6	10.9	14.0
Experimental	**4769 ± 6**	**3448 ± 10**	**1200 ± 12**	**1945 ± 6**	**2298 ± 5**	**72.3**	**25.2**	**40.8**	**48.2**	**Reference**

c) 15 nm		Absolute intensities ± relative std. deviation in %					Intensity ratios in %				
		$I_{La\text{-}E}$	$I_{La\text{-}C}$	$I_{Li\text{-}La}$	$I_{Ti\text{-}E}$	$I_{Ti\text{-}C}$	$I_{La\text{-}C}$:$I_{La\text{-}E}$	I_{Li}:$I_{La\text{-}E}$	$I_{Ti\text{-}E}$:$I_{La\text{-}E}$	$I_{Ti\text{-}C}$:$I_{La\text{-}E}$	
							Absolute difference to reference (experimental)				Average absolute difference
Model	Only shift	16.6 ± 0.8	11.5 ±9.0	1.3 ± 5.8	6.8 ± 0.8	7.4 ± 0.7	69.2	7.6	40.9	44.5	
							3.1	17.6	0.1	3.7	6.1
	10La-10Ti	15.3 ± 6.8	11.5 ± 9.5	3.4 ± 39.2	6.2 ± 5.1	7.4 ± 1.1	75.3	22.3	40.4	48.3	
							3.0	2.9	0.4	0.1	**1.6**
	20La-10Ti	13.7 ± 6.8	11.5± 9.0	6.1 ± 26.8	6.4 ± 5.9	7.4 ± 0.9	83.8	44.2	46.5	53.8	
							11.5	19.1	5.7	5.6	10.5
	15La-15Ti	14.9 ± 6.8	11.5± 9.6	4.0 ± 22.5	5.8 ± 7.1	7.4 ± 1.4	77.1	27.0	38.7	49.6	
							4.8	1.8	2.1	1.4	2.5
	10La-20Ti	15.9 ± 4.8	11.5± 9.3	3.8 ± 32.7	5.6 ± 6.7	7.4 ± 1.0	72.4	23.9	35.4	46.6	
							0.1	1.3	5.4	1.6	**2.1**
	20La-20Ti	14.0 ± 9.9	11.5± 9.5	6.6 ± 27.8	5.9 ± 8.5	7.4 ± 1.2	82.1	47.3	42.0	52.8	
							9.8	22.1	1.2	4.6	9.4
Experimental		**4769 ± 6**	**3448 ± 10**	**1200 ± 12**	**1945 ± 6**	**2298 ± 5**	**72.3**	**25.2**	**40.8**	**48.2**	Reference

References

[1] M. Armand and J.-M. Tarascon, "Building better batteries," *Nature*, vol. 451, pp. 652–657, 2008.

[2] J. B. Goodenough and K. S. Park, "The Li-ion rechargeable battery: A perspective," *J Am Chem Soc*, vol. 135, no. 4, pp. 1167–1176, 2013, doi: 10.1021/ja3091438.

[3] M. H. Braga, N. S. Grundish, A. J. Murchison, and J. B. Goodenough, "Alternative strategy for a safe rechargeable battery," *Energy Environ Sci*, vol. 10, no. 1, pp. 331–336, 2017, doi: 10.1039/c6ee02888h.

[4] M. Ma, M. Zhang, B. Jiang, Y. Du, B. Hu, and C. Sun, "A review of all-solid-state electrolytes for lithium batteries: high-voltage cathode materials, solid-state electrolytes and electrode-electrolyte interfaces," *Mater Chem Front*, vol. 7, pp. 1268–1297, 2023, doi: 10.1039/d2qm01071b.

[5] T. Kim, W. Song, D. Y. Son, L. K. Ono, and Y. Qi, "Lithium-ion batteries: outlook on present, future, and hybridized technologies," *J Mater Chem A Mater*, vol. 7, no. 7, pp. 2942–2964, 2019, doi: 10.1039/C8TA10513H.

[6] J. Janek and W. G. Zeier, "A solid future for battery development," *Nat Energy*, vol. 1, no. 9, 2016, doi: 10.1038/nenergy.2016.141.

[7] R. Van Noorden, "The rechargeable revolution: A better battery," *Nature*, vol. 507, pp. 26–28, 2014, doi: https://doi.org/10.1038/507026a.

[8] D. H. S. Tan, A. Banerjee, Z. Chen, and Y. S. Meng, "From nanoscale interface characterization to sustainable energy storage using all-solid-state batteries," *Nat Nanotechnol*, vol. 15, no. 3, pp. 170–180, 2020, doi: 10.1038/s41565-020-0657-x.

[9] V. Etacheri, R. Marom, R. Elazari, G. Salitra, and D. Aurbach, "Challenges in the development of advanced Li-ion batteries: A review," *Energy Environ Sci*, vol. 4, no. 9, pp. 3243–3262, 2011, doi: 10.1039/c1ee01598b.

[10] N. Nitta, F. Wu, J. T. Lee, and G. Yushin, "Li-ion battery materials: Present and future," *Materials Today*, vol. 18, no. 5, pp. 252–264, 2015, doi: 10.1016/j.mattod.2014.10.040.

[11] M. V. Reddy, C. M. Julien, A. Mauger, and K. Zaghib, "Sulfide and oxide inorganic solid electrolytes for all-solid-state Li batteries: A review," *Nanomaterials*, vol. 10, no. 8, pp. 1–80, 2020, doi: 10.3390/nano10081606.

[12] V. Thangadurai and W. Weppner, "Recent progress in solid oxide and lithium ion conducting electrolytes research," *Ionics (Kiel)*, vol. 12, no. 1, pp. 81–92, 2006, doi: 10.1007/s11581-006-0013-7.

[13] S. Dong *et al.*, "Challenges and Prospects of All-Solid-State Electrodes for Solid-State Lithium Batteries," *Adv Funct Mater*, 2023, doi: 10.1002/adfm.202304371.

[14] Z. Zhang *et al.*, "New horizons for inorganic solid state ion conductors," *Energy Environ Sci*, vol. 11, no. 8, pp. 1945–1976, 2018, doi: 10.1039/c8ee01053f.

[15] J.-M. Tarascon and M. Armand, "Issues and challenges facing rechargeable lithium batteries," *Nature*, vol. 414, pp. 359–367, 2001, doi: https://doi.org/10.1038/35104644.

[16] Statista Research Department, "Projected global battery demand from 2020 to 2030, by application." Accessed: Oct. 13, 2023. [Online]. Available: https://www.statista.com/statistics/1103218/global-battery-demand-forecast/

[17] A. Kim, S. Woo, M. Kang, H. Park, and B. Kang, "Research Progresses of Garnet-Type Solid Electrolytes for Developing All-Solid-State Li Batteries," *Front Chem*, vol. 8, 2020, doi: 10.3389/fchem.2020.00468.

[18] T. Wu, W. Dai, M. Ke, Q. Huang, and L. Lu, "All-Solid-State Thin Film μ-Batteries for Microelectronics," *Advanced Science*, vol. 8, no. 19, pp. 1–36, 2021, doi: 10.1002/advs.202100774.

[19] J. Schnell *et al.*, "All-solid-state lithium-ion and lithium metal batteries – paving the way to large-scale production," *J Power Sources*, vol. 382, pp. 160–175, 2018, doi: 10.1016/j.jpowsour.2018.02.062.

[20] K. Takada, "Progress and prospective of solid-state lithium batteries," *Acta Mater*, vol. 61, no. 3, pp. 759–770, 2013, doi: 10.1016/j.actamat.2012.10.034.

[21] J. Li, C. Ma, M. Chi, C. Liang, and N. J. Dudney, "Solid electrolyte: The key for high-voltage lithium batteries," *Adv Energy Mater*, vol. 5, p. 1401408, 2015, doi: 10.1002/aenm.201401408.

[22] P. Jiang *et al.*, "Solid-State Li Ion Batteries with Oxide Solid Electrolytes: Progress and Perspective," *Energy Technology*, 2022, doi: 10.1002/ente.202201288.

[23] Y. Xiao, Y. Wang, S. H. Bo, J. C. Kim, L. J. Miara, and G. Ceder, "Understanding interface stability in solid-state batteries," *Nat Rev Mater*, vol. 5, no. 2, pp. 105–126, 2020, doi: 10.1038/s41578-019-0157-5.

[24] H. Liu *et al.*, "Controlling Dendrite Growth in Solid-State Electrolytes," *ACS Energy Lett*, vol. 5, pp. 833–843, 2020, doi: 10.1021/acsenergylett.9b02660.

[25] J. B. Goodenough, "Rechargeable batteries: Challenges old and new," *Journal of Solid State Electrochemistry*, vol. 16, no. 6, pp. 2019–2029, 2012, doi: 10.1007/s10008-012-1751-2.

[26] M. Uitz, V. Epp, P. Bottke, and M. Wilkening, "Ion dynamics in solid electrolytes for lithium batteries: Probing jump rates and activation energies through time-domain Li NMR," *J Electroceram*, vol. 38, no. 2–4, pp. 142–156, 2017, doi: 10.1007/s10832-017-0071-4.

[27] X. Yao *et al.*, "All-solid-state lithium batteries with inorganic solid electrolytes: Review of fundamental science," *Chinese Physics B*, vol. 25, no. 1, 2016, doi: 10.1088/1674-1056/25/1/018802.

[28] R. Korthauer, Ed., *Lithium-ion batteries: Basics and applications*. Kriftel: Springer, 2018. doi: 10.1007/978-3-662-53071-9.

[29] B. Scrosati and J. Garche, "Lithium batteries: Status, prospects and future," *J Power Sources*, vol. 195, no. 9, pp. 2419–2430, 2010, doi: 10.1016/j.jpowsour.2009.11.048.

[30] N. Kireeva and V. S. Pervov, "Materials space of solid-state electrolytes: Unraveling chemical composition-structure-ionic conductivity relationships in garnet-type metal oxides using cheminformatics virtual screening approaches," *Physical Chemistry Chemical Physics*, vol. 19, no. 31, pp. 20904–20918, 2017, doi: 10.1039/c7cp00518k.

[31] K. Daems, P. Yadav, K. B. Dermenci, J. Van Mierlo, and M. Berecibar, "Advances in inorganic, polymer and composite electrolytes: Mechanisms of Lithium-ion transport and pathways to enhanced performance," *Renewable and Sustainable Energy Reviews*, vol. 191, 2024, doi: 10.1016/j.rser.2023.114136.

[32] A. Okos, C. F. Ciobota, A. M. Motoc, and R. R. Piticescu, "Review on Synthesis and Properties of Lithium Lanthanum Titanate," *Materials*, vol. 16, 2023, doi: 10.3390/ma16227088.

[33] S. Yan *et al.*, "Perovskite solid-state electrolytes for Lithium metal batteries," *Batteries*, vol. 7, no. 4, 2021, doi: 10.3390/batteries7040075.

[34] C. Cao, Z. Bin Li, X. L. Wang, X. B. Zhao, and W. Q. Han, "Recent advances in inorganic solid electrolytes for lithium batteries," *Front Energy Res*, vol. 2, 2014, doi: 10.3389/fenrg.2014.00025.

[35] J. Zhu *et al.*, "Insights into the local structure, microstructure and ionic conductivity of silicon doped NASICON-type solid electrolyte $Li_{1.3}Al_{0.3}Ti_{1.7}P_3O_{12}$," *Energy Storage Mater*, vol. 44, pp. 190–196, 2022, doi: 10.1016/j.ensm.2021.10.003.

[36] J.-H. Yin *et al.*, "Recent Advances of LATP and Their NASICON Structure as a Solid-State Electrolyte for Lithium-Ion Batteries," *Adv Eng Mater*, vol. 25, no. 20, 2023, doi: 10.1002/adem.202300566.

[37] R. DeWees and H. Wang, "Synthesis and Properties of NaSICON-type LATP and LAGP Solid Electrolytes," *ChemSusChem*, vol. 12, no. 16, pp. 3713–3725, 2019, doi: 10.1002/cssc.201900725.

[38] X. Xu, Z. Wen, X. Wu, X. Yang, and Z. Gu, "Lithium ion-conducting glass-ceramics of $Li_{1.5}Al_{0.5}Ge_{1.5}(PO_4)_{3-x}Li_2O$ (x=0.0-0.20) with good electrical and electrochemical properties," *Journal of the American Ceramic Society*, vol. 90, no. 9, pp. 2802–2806, 2007, doi: 10.1111/j.1551-2916.2007.01827.x.

[39] G. Yang *et al.*, "Advances in materials design for all-solid-state batteries: From bulk to thin films," *Applied Sciences (Switzerland)*, vol. 10, no. 14, 2020, doi: 10.3390/app10144727.

[40] M. Rawlence, I. Garbayo, S. Buecheler, and J. L. M. Rupp, "On the chemical stability of post-lithiated garnet Al-stabilized $Li_7La_3Zr_2O_{12}$ solid state electrolyte thin films," *Nanoscale*, vol. 8, no. 31, pp. 14746–14753, 2016, doi: 10.1039/c6nr04162k.

[41] X. Yang, J. Luo, and X. Sun, "Towards high-performance solid-state Li-S batteries: From fundamental understanding to engineering design," *Chem Soc Rev*, vol. 49, no. 7, pp. 2140–2195, 2020, doi: 10.1039/c9cs00635d.

[42] O. Bohnke, C. Bohnke, and J. L. Fourquet, "Mechanism of ionic conduction and electrochemical intercalation of lithium into the perovskite lanthanum lithium titanate," *Solid State Ion*, vol. 91, no. 1–2, pp. 21–31, 1996, doi: 10.1016/s0167-2738(96)00434-1.

[43] Y. Meesala, A. Jena, H. Chang, and R. S. Liu, "Recent Advancements in Li-Ion Conductors for All-Solid-State Li-Ion Batteries," *ACS Energy Lett*, vol. 2, pp. 2734–2751, 2017, doi: 10.1021/acsenergylett.7b00849.

[44] Y. Inaguma *et al.*, "High lithium ion conductivity in the perovskite-type compounds," *Solid State Commun*, vol. 86, no. 10, pp. 689–693, 1993.

[45] F. Aguesse, J. M. López Del Amo, V. Roddatis, A. Aguadero, and J. A. Kilner, "Enhancement of the grain boundary conductivity in ceramic $Li_{0.34}La_{0.55}TiO_3$ electrolytes in a moisture-free processing environment," *Adv Mater Interfaces*, vol. 1, no. 7, 2014, doi: 10.1002/admi.201300143.

[46] C. Ma *et al.*, "Atomic-scale origin of the large grain-boundary resistance in perovskite Li-ion-conducting solid electrolytes," *Energy Environ Sci*, vol. 7, no. 5, pp. 1638–1642, 2014, doi: 10.1039/c4ee00382a.

[47] S. Sasano *et al.*, "Grain boundary Li-ion conductivity in $(Li_{0.33}La_{0.56})TiO_3$ polycrystal," *Appl Phys Lett*, vol. 116, 2020, doi: 10.1063/1.5141396.

[48] H. Kawai and J. Kuwano, "Lithium Ion Conductivity of A-Site Deficient Perovskite Solid Solution $La_{0.67-x}Li_{3x}TiO_3$," *J Electrochem Soc*, vol. 141, no. 7, pp. L78–L79, 1994, doi: 10.1149/1.2055043.

[49] N. F. Atta, A. Galal, and E. H. El-Ads, "Perovskite Nanomaterials – Synthesis, Characterization, and Applications," in *Perovskite Materials - Synthesis, Characterisation, Properties, and Applications*, L. Pan and G. Zhu, Eds., InTech, 2016. doi: 10.5772/61280.

[50] R. J. D. Tilley, *Perovskites: Structure–Property Relationships*. West Sussex: John Wiley & Sons, 2016.

[51] L. Pan and G. Zhu, Eds., *Perovskite Materials Synthesis, Characterisation, Properties, and Applications*. ExLi4EvA, 2016.

[52] P. Kaur and K. Singh, "Review of perovskite-structure related cathode materials for solid oxide fuel cells," *Ceram Int*, vol. 46, no. 5, pp. 5521–5535, 2020, doi: 10.1016/j.ceramint.2019.11.066.

[53] W. J. Yin, B. Weng, J. Ge, Q. Sun, Z. Li, and Y. Yan, "Oxide perovskites, double perovskites and derivatives for electrocatalysis, photocatalysis, and photovoltaics," *Energy Environ Sci*, vol. 12, no. 2, pp. 442–462, 2019, doi: 10.1039/c8ee01574k.

[54] R. M. Hazen, "Perovskites gives rise to materials that have a wide array of electrical properties," *Sci Am*, vol. 258, no. 6, pp. 74–81, 1988.

[55] Y. A. Abramov, V. G. Tsirelson, V. E. Zavodnik, S. A. Ivanov, and I. D. Brown, "The chemical bond and atomic displacements in $SrTiO_3$ from X-ray diffraction analysis," *Acta Crystallographica Section B*, vol. 51, no. 6, pp. 942–951, 1995, doi: 10.1107/S0108768195003752.

[56] A. Putnis, *Introduction to Mineral Science*. Cambridge: Cambridge University Press, 1992.

[57] R. H. Mitchell, M. D. Welch, and A. R. Chakhmouradian, "Nomenclature of the perovskite supergroup: A hierarchical system of classification based on crystal structure and composition," *Mineral Mag*, vol. 81, no. 3, pp. 411–461, 2017, doi: 10.1180/minmag.2016.080.156.

[58] M. Johnsson and P. Lemmens, "Perovskites and thin films - Crystallography and chemistry," *Journal of Physics Condensed Matter*, vol. 20, no. 26, 2008, doi: 10.1088/0953-8984/20/26/264001.

[59] A. C. Marques, "Properties of strontium titanate." Accessed: Jul. 08, 2022. [Online]. Available: 12/01/2024https://repositorio.ul.pt/bitstream/10451/1643/10/19741_ulsd_re487_10_Chapter2.pdf

[60] C. Lu *et al.*, "New insight into the structural evolution of $PbTiO_3$: An unbiased structure search," *Physical Chemistry Chemical Physics*, vol. 19, no. 2, pp. 1420–1424, 2017, doi: 10.1039/c6cp07624f.

[61] M. Yashima and R. Ali, "Structural phase transition and octahedral tilting in the calcium titanate perovskite $CaTiO_3$," *Solid State Ion*, vol. 180, no. 2–3, pp. 120–126, 2009, doi: 10.1016/j.ssi.2008.11.019.

[62] A. M. Glazer, "The classification of tilted octahedra in perovskites," *Acta Crystallogr B*, vol. 28, no. 11, pp. 3384–3392, 1972, doi: 10.1107/s0567740872007976.

[63] C. J. Howard and H. T. Stokes, "Group-theoretical analysis of octahedral tilting in ferroelectric perovskites," *Acta Crystallogr B*, vol. 54, pp. 782–789, 1998, doi: 10.1107/S0108768102015756.

[64] Z. Zeng *et al.*, "Rare-earth-containing perovskite nanomaterials: Design, synthesis, properties and applications," *Chem Soc Rev*, vol. 49, no. 4, pp. 1109–1143, 2020, doi: 10.1039/c9cs00330d.

[65] P. Goel *et al.*, "Perovskite materials as superior and powerful platforms for energy conversion and storage applications," *Nano Energy*, vol. 80, p. 105552, 2021, doi: 10.1016/j.nanoen.2020.105552.

[66] M. T. Anderson, K. B. Greenwood, G. A. Taylor, and K. R. Poeppelmeiert, "B-Cation Arrangements in Double Perovskites," *Pros. Solid St. Chem.*, vol. 22, pp. 197–233, 1993.

[67] Y. Zheng *et al.*, "Unique characteristics of 2D Ruddlesden-Popper (2DRP) perovskite for future photovoltaic application," *J Mater Chem A Mater*, vol. 7, no. 23, pp. 13860–13872, 2019, doi: 10.1039/c9ta03217g.

[68] N. A. Benedek, J. M. Rondinelli, H. Djani, P. Ghosez, and P. Lightfoot, "Understanding ferroelectricity in layered perovskites: New ideas and insights from theory and experiments," *Dalton Transactions*, vol. 44, no. 23, pp. 10543–10558, 2015, doi: 10.1039/c5dt00010f.

[69] V. Thangadurai, P. Schmid-Beurmann, and W. Weppner, "Synthesis, structure, and electrical conductivity of $A'[A_2B_3O_{10}]$ (A′ = Rb, Cs; A = Sr, Ba; B= Nb, Ta): New members of Dion-Jacobson-Type layered perovskites," *J Solid State Chem*, vol. 158, no. 2, pp. 279–289, 2001, doi: 10.1006/jssc.2001.9108.

[70] M. Johnsson and P. Lemmens, "Crystallography and Chemistry of Perovskites," *Novel Materials*, 2007, doi: https://doi.org/10.1002/9780470022184.hmm411.

[71] S. N. Ruddlesden and P. Popper, "The compound $Sr_3Ti_2O_7$ and its structure," *Acta Crystallogr*, vol. 11, no. 1, pp. 54–55, 1958, doi: 10.1107/s0365110x58000128.

[72] F. Hatert, S. J. Mills, M. Pasero, R. Miyawaki, and F. Bosi, "CNMNC guidelines for the nomenclature of polymorphs and polysomes," *Mineral Mag*, vol. 87, no. 2, pp. 225–232, 2023, doi: 10.1180/mgm.2023.13.

[73] G. Nirala, D. Yadav, and S. Upadhyay, "Ruddlesden-Popper phase A_2BO_4 oxides: Recent studies on structure, electrical, dielectric, and optical properties," *Journal of Advanced Ceramics*, vol. 9, no. 2, pp. 129–148, 2020, doi: 10.1007/s40145-020-0365-x.

[74] M. Borowski, Ed., *Perovskites : Structure, Properties and Uses*. New York: Nova Science Publishers, Inc., 2010.

[75] M. Zinkevich and F. Aldinger, "Thermodynamic assessment of the gallium-oxygen system," *Journal of the American Ceramic Society*, vol. 87, no. 4, pp. 683–691, 2004, doi: 10.1111/j.1551-2916.2004.00683.x.

[76] P. Ganguly and C. N. R. Rao, "Crystal chemistry and magnetic properties of layered metal oxides possessing the K_2NiF_4 or related structures," *J Solid State Chem*, vol. 53, no. 2, pp. 193–216, 1984, doi: 10.1016/0022-4596(84)90094-X.

[77] D. Lee and H. N. Lee, "Controlling oxygen mobility in ruddlesden-popper oxides," *Materials*, vol. 10, no. 4, 2017, doi: 10.3390/ma10040368.

[78] X. Xu, Y. Pan, Y. Zhong, R. Ran, and Z. Shao, "Ruddlesden-Popper perovskites in electrocatalysis," *Mater Horiz*, vol. 7, no. 10, pp. 2519–2565, 2020, doi: 10.1039/d0mh00477d.

[79] G. Stone *et al.*, "Atomic scale imaging of competing polar states in a Ruddlesden-Popper layered oxide," *Nat Commun*, vol. 7, 2016, doi: 10.1038/ncomms12572.

[80] Y. Tokuda *et al.*, "Growth of Ruddlesden-Popper type faults in Sr-excess $SrTiO_3$ homoepitaxial thin films by pulsed laser deposition," *Appl Phys Lett*, vol. 99, no. 17, 2011, doi: 10.1063/1.3656340.

[81] E. Detemple *et al.*, "Ruddlesden-Popper faults in $LaNiO_3/LaAlO_3$ superlattices," *J Appl Phys*, vol. 112, no. 1, pp. 1–6, 2012, doi: 10.1063/1.4731249.

[82] W. Wang *et al.*, "Atomic structures of Ruddlesden-Popper faults in $LaCoO_3/SrRuO_3$ multilayer thin films induced by epitaxial strain," *J Cryst Growth*, vol. 490, pp. 110–115, 2018, doi: 10.1016/j.jcrysgro.2018.03.029.

[83] J. Bak and S. Y. Chung, "Observation of fault-free coherent layer during Ruddlesden–Popper faults generation in LaNiO3 thin films," *Journal of the Korean Ceramic Society*, 2020, doi: 10.1007/s43207-020-00080-7.

[84] M. M. Islam, P. Heitjans, and T. Bredow, "Structural Analysis and Li Migration Pathways in Ramsdellite $Li_2Ti_3O_7$: A Theoretical Study," *Journal of Physical Chemistry C*, vol. 120, no. 1, pp. 5–10, 2016, doi: 10.1021/acs.jpcc.5b07942.

[85] T. F. Yi, S. Y. Yang, and Y. Xie, "Recent advances of $Li_4Ti_5O_{12}$ as a promising next generation anode material for high power lithium-ion batteries," *J Mater Chem A Mater*, vol. 3, no. 11, pp. 5750–5777, 2015, doi: 10.1039/c4ta06882c.

[86] Y. Kang, Y. Xie, F. Su, K. Dai, M. Shui, and J. Shu, "α-Li_2TiO_3: a new ultrastable anode material for lithium-ion batteries," *Dalton Transactions*, vol. 51, no. 47, pp. 18277–18283, 2022, doi: 10.1039/d2dt03115a.

[87] S. Škapin, D. Kolar, and D. Suvorov, "X-ray Diffraction and Microstructural Investigation of the Al_2O_3-La_2O_3-TiO_2 System," *Journal of the American Ceramic Society*, vol. 76, no. 9, pp. 2359–2362, 1993, doi: 10.1111/j.1151-2916.1993.tb07777.x.

[88] S. De Cliff, M. L. Post, and I. Davidson, "Synthesis and Characterization of Lithium-Doped Lanthanum Titanate Oxide Materials for the Fabrication of a Solid-State Microbattery Rectifier for Use in Direct Methanol Fuel Cell Powered Device," *East African Journal of Sciences (2012)*, vol. 6, no. 1, pp. 1–10, 2012.

[89] M. Abe and K. Uchino, "X-ray study of the deficient perovskite $La_{2/3}TiO_3$," *Mater Res Bull*, vol. 9, pp. 147–156, 1974.

[90] A. D. Robertson, S. G. Martin, A. Coats, and A. R. West, "Phase diagrams and crystal chemistry in the Li+ ion conducting perovskites, $Li_{0.5-3x}RE_{0.5+x}TiO_3$: RE = La, Nd," *J Mater Chem*, vol. 5, no. 9, pp. 1405–1412, 1995, doi: 10.1039/JM9950501405.

[91] A. G. Belous, G. N. Novitskaya, S. V. Polyanetskaya, and Yu. I. Gornikov, "Investigation into complex oxides of $La_{2/3-x}Li_{3x}TiO_3$ composition," *Inorganic Materials*, vol. 23, no. 3, p. 412, 1987.

[92] K. Toda and J. Watanave, "Crystal structure determination of ion-exchangeable layered perovskite compounds, $K_2La_2Ti_3O_{10}$ and $Li_2La_2Ti_5O_{10}$," *Mater Res Bull*, vol. 31, no. 11, pp. 1427–1435, 1996.

[93] S. J. Fanah, M. Yu, A. Huq, and F. Ramezanipour, "Insight into lithium-ion mobility in $Li_2La(TaTi)O_7$," *J Mater Chem A Mater*, vol. 6, no. 44, pp. 22152–22160, 2018, doi: 10.1039/c8ta05187a.

[94] A. Rivera and J. Sanz, "Lithium dynamics in the fast ionic conductor $Li_{0.18}La_{0.61}TiO_3$ probed by ^{7}Li NMR spectroscopy," *Phys Rev B Condens Matter Mater Phys*, vol. 70, no. 9, 2004, doi: 10.1103/PhysRevB.70.094301.

[95] J. Sanz, A. Varez, J. A. Alonso, and M. T. Fernandez, "Structural changes produced during heating of the fast ion conductor $Li_{0.18}La_{0.61}TiO_3$. A neutron diffraction study," *J Solid State Chem*, vol. 177, no. 4–5, pp. 1157–1164, 2004, doi: 10.1016/j.jssc.2003.10.036.

[96] X. Zhou *et al.*, "Revealing the dominant factor of domain boundary resistance on bulk conductivity in lanthanum lithium titanates," *Journal of Energy Chemistry*, vol. 73, pp. 354–359, 2022, doi: 10.1016/j.jechem.2022.06.020.

[97] Y. Inaguma, "Fast Percolative Diffusion in Lithium Ion-conducting Perovskite-type Oxide," *Journal of the Ceramic Society of Japan*, vol. 114, no. 12, pp. 1103–1110, 2006.

[98] K. Mori, S. Tomihira, K. Iwase, and T. Fukunaga, "Visualization of conduction pathways in a lanthanum lithium titanate superionic conductor synthesized by rapid cooling," *Solid State Ion*, vol. 268, no. Part A, pp. 76–81, 2014, doi: 10.1016/j.ssi.2014.09.030.

[99] M. Catti, M. Sommariva, and R. M. Ibberson, "Tetragonal superstructure and thermal history of $Li_{0.3}La_{0.567}TiO_3$ (LLTO) solid electrolyte by neutron diffraction," *J Mater Chem*, vol. 17, no. 13, pp. 1300–1307, 2007, doi: 10.1039/b614345h.

[100] A. Várez *et al.*, "Influence of quenching treatments on structure and conductivity of the $Li_{3x}La_{2/3-x}TiO_3$ series," *Chemistry of Materials*, vol. 15, no. 1, pp. 225–232, 2003, doi: 10.1021/cm020172q.

[101] A. Varez, M. T. Fernández-Ðaz, J. A. Alonso, and J. Sanz, "Structure of fast ion conductors $Li_{3x}La_{2/3-x}TiO_3$ deduced from powder neutron diffraction experiments," *Chemistry of Materials*, vol. 17, no. 9, pp. 2404–2412, 2005, doi: 10.1021/cm047841f.

[102] J. Ibarra, A. Várez, C. León, J. Santamaría, L. M. Torres-Martínez, and J. Sanz, "Influence of composition on the structure and conductivity of the fast ionic conductors $La_{2/3-x}Li_{3x}TiO_3$ ($0.03 \leq x \leq 0.167$)," *Solid State Ion*, vol. 134, no. 3–4, pp. 219–228, 2000, doi: 10.1016/S0167-2738(00)00761-X.

[103] J. L. Fourquet, H. Duroy, and M. P. Crosnier-Lopez, "Structural and Microstructural Studies of the Series $La_{2/3-x}Li_{3x}TiO_3$," *J Solid State Chem*, vol. 127, no. 1996, pp. 283–294, 1996.

[104] O. Bohnke, H. Duroy, J.-L. Fourquet, S. Ronchetti, and D. Mazza, "In search of the cubic phase of the Li + ion-conducting perovskite $La_{2/3-x}Li_{3x}TiO_3$: structure and properties of quenched and in situ heated samples," *Solid State Ion*, vol. 149, pp. 217–226, 2002.

[105] Y. Harada, Y. Hirakoso, H. Kawai, and J. Kuwano, "Order–disorder of the A-site ions and lithium ion conductivity in the perovskite solid solution $La_{0.67-x}Li_{3x}TiO_3$ (x=0.11)," *Solid State Ion*, vol. 121, pp. 245–251, 1999.

[106] A. D. Robertson, S. G. Martin, A. Coats, and A. R. West, "Phase diagrams and crystal chemistry in the Li+ ion conducting perovskites, $Li_{0.5-3x}RE_{0.5+x}TiO_3$: RE = La, Nd," *J Mater Chem*, vol. 5, no. 9, pp. 1405–1412, 1995, doi: 10.1039/JM9950501405.

[107] Y. Inaguma, T. Katsumata, M. Itoh, and Y. Morii, "Crystal structure of a lithium ion-conducting perovskite $La_{2/3-x}Li_{3x}TiO_3$ (x = 0.05)," *J Solid State Chem*, vol. 166, no. 1, pp. 67–72, 2002, doi: 10.1006/jssc.2002.9560.

[108] Y. Harada, T. Ishigaki, H. Kawai, and J. Kuwano, "Lithium ion conductivity of polycrystalline perovskite $La_{0.67-x}Li_{3x}TiO_3$ with ordered and disordered arrangements of the A-site ions," *Solid State Ion*, vol. 108, pp. 407–413, 1998.

[109] S. J. Fanah and F. Ramezanipour, "Strategies for Enhancing Lithium-Ion Conductivity of Triple-Layered Ruddlesden − Popper Oxides : Case Study of $Li_{2-x}La_{2-y}Ti_{3-z}Nb_zO_{10}$," *Inorg Chem*, vol. 59, pp. 9718–9727, 2020, doi: 10.1021/acs.inorgchem.0c00962.

[110] B. Zhang *et al.*, "Mechanisms and properties of ion-transport in inorganic solid electrolytes," *Energy Storage Mater*, vol. 10, no. August 2017, pp. 139–159, 2018, doi: 10.1016/j.ensm.2017.08.015.

[111] Y. Inaguma, L. Chen, M. Itoh, and T. Nakamura, "Candidate compounds with perovskite structure for high lithium ionic conductivity," *Solid State Ion*, vol. 70–71, pp. 196–202, 1994, doi: 10.1016/0167-2738(94)90309-3.

[112] Y. Tanaka and T. Ohnoz, "Two dimensional li diffusion in ion-conductive lithium lanthanum titanates," *ECS Electrochemistry Letters*, vol. 2, no. 7, 2013, doi: 10.1149/2.008306eel.

[113] K. Y. Yang *et al.*, "Mechanism of the interfacial reaction between cation-deficient $La_{0.56}Li_{0.33}TiO_3$ and metallic lithium at room temperature," *J Mater Res*, vol. 23, no. 7, pp. 1813–1825, 2008, doi: 10.1557/jmr.2008.0255.

[114] Y. Inaguma, Y. Matsui, Y. J. Shan, M. Itoh, and T. Nakamura, "Lithium ion conductivity in the perovskite-type $LiTaO_3$-$SrTiO_3$ solid solution," *Solid State Ion*, vol. 79, pp. 91–97, 1995, doi: 10.1016/0167-2738(95)00036-6.

[115] H. Geng, A. Mei, Y. Lin, and C. Nan, "Effect of sintering atmosphere on ionic conduction and structure of $Li_{0.5}La_{0.5}TiO_3$ solid electrolytes," *Mater Sci Eng B Solid State Mater Adv Technol*, vol. 164, no. 2, pp. 91–95, 2009, doi: 10.1016/j.mseb.2009.07.011.

[116] Y. Harada, H. Watanabe, J. Kuwano, and Y. Saito, "Lithium ion conductivity of A-site deficient perovskite solid solutions," *J Power Sources*, vol. 81–82, pp. 777–781, 1999.

[117] X. Hu *et al.*, "Mechanical and electrochemical properties of cubic and tetragonal $Li_xLa_{0.557}TiO_3$ perovskite oxide electrolytes," *Ceram Int*, vol. 44, no. 2, pp. 1902–1908, 2018, doi: 10.1016/j.ceramint.2017.10.129.

[118] A. R. Symington, J. Purton, J. Statham, M. Molinari, M. S. Islam, and S. C. Parker, "Quantifying the impact of disorder on Li-ion and Na-ion transport in perovskite titanate solid electrolytes for solid-state batteries," *J Mater Chem A Mater*, vol. 8, no. 37, pp. 19603–19611, 2020, doi: 10.1039/d0ta05343k.

[119] W. Araki, K. Suzuki, and Y. Arai, "Lithium diffusion in $La_{2/3-x}Li_{3x}TiO_3$ (x = 0.115) with 3D-ordered configurations," *Solid State Ion*, vol. 368, 2021, doi: 10.1016/j.ssi.2021.115706.

[120] X. Gao *et al.*, "Lithium atom and A-site vacancy distributions in lanthanum lithium titanate," *Chemistry of Materials*, vol. 25, no. 9, pp. 1607–1614, 2013, doi: 10.1021/cm3041357.

[121] S. De Cliff, M. L. Post, and I. Davidson, "Synthesis and Characterization of Lithium-Doped Lanthanum Titanate Oxide Materials for the Fabrication of a Solid-State Microbattery Rectifier for Use in Direct Methanol Fuel Cell Powered Device," *East African Journal of Sciences*, vol. 6, no. 1, pp. 1–10, 2012.

[122] Y. Sun, P. Guan, Y. Liu, H. Xu, S. Li, and D. Chu, "Recent Progress in Lithium Lanthanum Titanate Electrolyte towards All Solid-State Lithium Ion Secondary Battery," *Critical Reviews in Solid State and Materials Sciences*, vol. 44, no. 4, pp. 265–282, 2018, doi: 10.1080/10408436.2018.1485551.

[123] J. Wei, D. Ogawa, T. Fukumura, Y. Hirose, and T. Hasegawa, "Epitaxial strain-controlled ionic conductivity in li-ion solid electrolyte $Li_{0.33}La_{0.56}TiO_3$ thin films," *Cryst Growth Des*, vol. 15, no. 5, pp. 2187–2191, 2015, doi: 10.1021/cg501834s.

[124] S. Zhang, H. Zhao, J. Guo, Z. Du, J. Wang, and K. Świerczek, "Characterization of Sr-doped lithium lanthanum titanate with improved transport properties," *Solid State Ion*, vol. 336, no. March, pp. 39–46, 2019, doi: 10.1016/j.ssi.2019.03.015.

[125] A. Morata-Orrantia, S. García-Martín, and M. Á. Alario-Franco, "Optimization of Lithium Conductivity in La/Li Titanates," *Chemistry of Materials*, vol. 15, no. 21, pp. 3991–3995, 2003, doi: 10.1021/cm0300563.

[126] J. Lu, Y. Li, and Y. Ding, "Structure, stability, and ionic conductivity of perovskite $Li_{2x-y}Sr_{1-x-y}La_yTiO_3$ solid electrolytes," *Ceram Int*, vol. 46, no. 6, pp. 7741–7747, 2020, doi: 10.1016/j.ceramint.2019.11.277.

[127] G. X. Wang, P. Yao, D. H. Bradhurst, S. X. Dou, and H. K. Liu, "Structure characteristics and lithium ionic conductivity of $La_{(0.57-2x/3)}Sr_xLi_{0.3}TiO_3$ perovskites," *J Mater Sci*, vol. 35, pp. 4289–4291, 2000.

[128] T. Teranishi, A. Kouchi, H. Hayashi, and A. Kishimoto, "Dependence of the conductivity of polycrystalline $Li_{0.33}Ba_xLa_{0.56-2/3x}TiO_3$ on Ba loading," *Solid State Ion*, vol. 263, pp. 33–38, 2014, doi: 10.1016/j.ssi.2014.05.001.

[129] R. Li *et al.*, "Realizing fourfold enhancement in conductivity of perovskite $Li_{0.33}La_{0.557}TiO_3$ electrolyte membrane via a Sr and Ta co-doping strategy," *J Memb Sci*, vol. 582, no. March, pp. 194–202, 2019, doi: 10.1016/j.memsci.2019.03.074.

[130] J. Q. Zheng, Y. F. Li, R. Yang, G. Li, and X. K. Ding, "Lithium ion conductivity in the solid electrolytes $(Li_{0.25}La_{0.25})_{1-x}M_{0.5x}NbO_3$ (M=Sr, Ba, Ca, x=0.125) with perovskite-type structure," *Ceram Int*, vol. 43, no. 2, pp. 1716–1721, 2017, doi: 10.1016/j.ceramint.2016.08.144.

[131] H.-T. Chung, J.-G. Kim, and H.-G. Kim, "Dependence of the lithium ionic conductivity on the B-site ion substitution in $(Li_{0.5}La_{0.5})Ti_{1-x}M_xO_3$ (M=Sn, Zr, Mn, Ge)," *Solid State Ion*, vol. 107, pp. 153–160, 1998.

[132] V. Thangadurai and W. Weppner, "Effect of B-site substitution of (Li,La)TiO_3 perovskites by di-, tri-, tetra- and hexavalent metal ions on the lithium ion conductivity," *Ionics (Kiel)*, vol. 6, no. 1–2, pp. 70–77, 2000, doi: 10.1007/BF02375549.

[133] A. Jonderian, R. Peng, D. Davies, and E. McCalla, "Benefits and Limitations of 226 Substitutions into Li-La-Ti-O Perovskites," *Chemistry of Materials*, vol. 35, no. 16, pp. 6227–6234, 2023, doi: 10.1021/acs.chemmater.3c00505.

[134] X. Gao *et al.*, "Domain boundary structures in lanthanum lithium titanates," *J Mater Chem A Mater*, vol. 2, no. 3, pp. 843–852, 2014, doi: 10.1039/c3ta13726k.

[135] W. J. Kwon *et al.*, "Enhanced Li^+ conduction in perovskite $Li_{3X}La_{2/3-x}\square_{1/3-2x}TiO_3$ solid-electrolytes via microstructural engineering," *J Mater Chem A Mater*, vol. 5, no. 13, pp. 6257–6262, 2017, doi: 10.1039/c7ta00196g.

[136] F. Zhu *et al.*, "Single-atom-layer traps in a solid electrolyte for lithium batteries," *Nat Commun*, vol. 11, no. 1, pp. 1–9, 2020, doi: 10.1038/s41467-020-15544-x.

[137] L. Xu, L. Zhang, Y. Hu, and L. Luo, "Structural origin of low Li-ion conductivity in perovskite solid-state electrolyte," *Nano Energy*, vol. 92, 2022, doi: 10.1016/j.nanoen.2021.106758.

[138] A. R. Symington *et al.*, "Elucidating the nature of grain boundary resistance in lithium lanthanum titanate," *J Mater Chem A Mater*, vol. 9, no. 10, pp. 6487–6498, 2021, doi: 10.1039/d0ta11539h.

[139] J. F. Wu and X. Guo, "Origin of the low grain boundary conductivity in lithium ion conducting perovskites: $Li_{3x}La_{0.67-x}TiO_3$," *Physical Chemistry Chemical Physics*, vol. 19, no. 8, pp. 5880–5887, 2017, doi: 10.1039/c6cp07757a.

[140] H. Moriwake *et al.*, "Domain boundaries and their influence on Li migration in solid-state electrolyte (La,Li)TiO_3," *J Power Sources*, vol. 276, pp. 203–207, 2015, doi: 10.1016/j.jpowsour.2014.11.139.

[141] S. Peng *et al.*, "Intrinsic layered defects in solid-state electrolyte $Li_{0.33}La_{0.56}TiO_3$," *Mater Today Energy*, vol. 23, 2022, doi: 10.1016/j.mtener.2021.100912.

[142] L. Zhang, L. Xu, Y. Nian, W. Wang, Y. Han, and L. Luo, "Atomic Defect Mediated Li-Ion Diffusion in a Lithium Lanthanum Titanate Solid-State Electrolyte," *ACS Nano*, vol. 16, no. 4, pp. 6898–6905, 2022, doi: 10.1021/acsnano.2c02250.

[143] A. Mei, Q. H. Jiang, Y. H. Lin, and C. W. Nan, "Lithium lanthanum titanium oxide solid-state electrolyte by spark plasma sintering," *J Alloys Compd*, vol. 486, no. 1–2, pp. 871–875, 2009, doi: 10.1016/j.jallcom.2009.07.091.

[144] P. Braun, C. Uhlmann, A. Weber, H. Störmer, D. Gerthsen, and E. Ivers-Tiffée, "Separation of the bulk and grain boundary contributions to the total conductivity of solid lithium-ion conducting electrolytes," *J Electroceram*, vol. 38, no. 2–4, pp. 157–167, 2017, doi: 10.1007/s10832-016-0061-y.

[145] R. B. De Oliveira, M. R. B. Andreeta, D. M. P. F. De Souza, J. E. F. S. Rodrigues, and P. S. Pizani, "Innovative Design for the Enhancement of Lithium Lanthanum Titanate Electrolytes," *Cryst Growth Des*, vol. 19, no. 9, pp. 4897–4901, 2019, doi: 10.1021/acs.cgd.9b00825.

[146] K. Takatori, H. Kadoura, H. Matsuo, and T. Tani, "Microstructural analyses and improved ionic conductivity of $La_{0.62}Li_{0.16}TiO_3$ ceramics prepared by a reactive-templated grain growth (RTGG) process," *J Eur Ceram Soc*, vol. 39, no. 2–3, pp. 384–388, 2019, doi: 10.1016/j.jeurceramsoc.2018.09.038.

[147] A. Morata-Orrantia, S. García-Martín, and M. Á. Alario-Franco, "Optimization of Lithium Conductivity in La/Li Titanates," *Chemistry of Materials*, vol. 15, no. 21, pp. 3991–3995, 2003, doi: 10.1021/cm0300563.

[148] S. J. Lee, J. J. Bae, and J. T. Son, "Structural and Electrical Effects of Y-doped $Li_{0.33}La_{0.56-x}Y_xTiO_3$ Solid Electrolytes on All-Solid-State Lithium Ion Batteries," *Journal of the Korean Physical Society*, vol. 74, no. 1, pp. 73–77, 2019, doi: 10.3938/jkps.74.73.

[149] T. Teranishi, M. Yamamoto, H. Hayashi, and A. Kishimoto, "Lithium ion conductivity of Nd-doped (Li, La)TiO_3 ceramics," *Solid State Ion*, vol. 243, pp. 18–21, 2013, doi: 10.1016/j.ssi.2013.04.014.

[150] A. Mei *et al.*, "Enhanced ionic transport in lithium lanthanum titanium oxide solid state electrolyte by introducing silica," *Solid State Ion*, vol. 179, no. 39, pp. 2255–2259, 2008, doi: 10.1016/j.ssi.2008.08.013.

[151] H. Zhang, X. Liu, Y. Qi, and V. Liu, "On the $La_{2/3-x}Li_{3x}TiO_3/Al_2O_3$ composite solid-electrolyte for Li-ion conduction," *J Alloys Compd*, vol. 577, pp. 57–63, 2013, doi: 10.1016/j.jallcom.2013.04.195.

[152] R. M. German, *Sintering : from empirical observations to scientific principles*, First Edition. Oxford: Elsevier, 2014.

[153] B. Carter and G. Norton, *Ceramic Materials: Science and Engineering*. New York: Springer Science+Business Media, LLC., 2007.

[154] S. Hampshire, "Fundamental Aspects of Hard Ceramics," in *Comprehensive Hard Materials*, vol. 2, Elsevier Ltd., 2014, pp. 3–28. doi: 10.1016/B978-0-08-096527-7.00020-9.

[155] S.-J. L. Kang, *Sintering: densification, grain growth and microstructure*. Oxford: Elsevier, 2004.

[156] W. D. Callister and D. G. Rethwisch, *Materials Science and Engineering: An introduction*. John Wiley & Sons, Inc., 2014. doi: 10.1016/0168-583X(93)95111-H.

[157] J. D. Powers and A. M. Glaeser, "Grain Boundary Migration in Ceramics," *Interface Science*, vol. 6, pp. 23–39, 1998.

[158] S.-J. L. Kang, "Abnormal grain growth," in *Sintering*, Elsevier, 2005, pp. 117–135.

[159] D. Kolar, U. Kunaver, and A. Recnik, "Exaggerated anisotropic grain growth in hexagonal barium titanate ceramics," *Physica Status Solidi A Appl Res*, vol. 166, no. 1, pp. 219–230, 1998.

[160] N. Daneu, S. Bernik, and A. Renik, "Inversion boundary induced grain growth in ZnO ceramics: From atomic-scale investigations to microstructural engineering," *J Phys Conf Ser*, vol. 326, no. 1, 2011, doi: 10.1088/1742-6596/326/1/012003.

[161] J. Wong, "Sintering and varistor characteristics of ZnO-Bi_2O_3 ceramics," *J Appl Phys*, vol. 51, no. 8, pp. 4453–4459, 1980, doi: 10.1063/1.328266.

[162] V. Y. Novikov, "Microstructure evolution during grain growth in materials with disperse particles," *Mater Lett*, vol. 68, pp. 413–415, 2012, doi: 10.1016/j.matlet.2011.10.101.

[163] U. Kunaver and D. Kolar, "Computer simulation of anisotropic grain growth in ceramics," *Acta metall. mater*, vol. 41, no. 8, pp. 2255–2263, 1993.

[164] M. Čeh, Gu. H., H. Mullejans, and A. Rečnik, "Analytical electron microscopy of planar faults in SrO-doped $CaTiO_3$," *J Mater Res*, vol. 12, no. 9, pp. 2438–2446, 1997.

[165] A. Rečnik, M. Čeh, and D. Kolar, "Polytype induced exaggerated grain growth in ceramics," *J Eur Ceram Soc*, vol. 21, no. 10–11, pp. 2117–2121, 2001, doi: 10.1016/S0955-2219(01)00184-4.

[166] S. Šturm, A. Rečnik, C. Scheu, and M. Čeh, "Formation of Ruddlesden–Popper faults and polytype phases in SrO-doped $SrTiO_3$," *J Mater Res*, vol. 15, no. 10, pp. 2131–2139, 2000, doi: 10.1557/JMR.2000.0307.

[167] S. Drev, A. Rečnik, and N. Daneu, "Twinning and epitaxial growth of taaffeite-type modulated structures in BeO-doped $MgAl_2O_4$," *CrystEngComm*, vol. 15, no. 14, pp. 2640–2647, 2013, doi: 10.1039/c3ce26997c.

[168] B.-K. Lee, S.-Y. Chung, and S.-J. L. Kang, "Control of {111| twin formation and abnormal grain growth in $BaTiO_3$," *Metals and Materials*, vol. 6, no. 4, pp. 301–304, 2000, doi: 10.1007/BF03028075.

[169] M. Čeh, "Scanning Transmission Electron Microscopy (STEM) of Ruddlesden-Popper Faults in Nonstoichiometric $CaTiO_3$," *Acta Chim Slov*, vol. 48, pp. 63–76, 2001.

[170] M. Čeh and D. Kolar, "Solubility of CaO in $CaTiO_3$," *J Mater Sci*, vol. 29, no. 23, pp. 6295–6300, 1994, doi: 10.1007/BF00354574.

[171] J. A. Alonso, J. Sanz, J. Santamaría, C. León, A. Várez, and M. T. Fernández-Díaz, "On the location of Li^+ cations in the fast Li-cation conductor $La_{0.5}Li_{0.5}TiO_3$ perovskite," *Angewandte Chemie - International Edition*, vol. 39, no. 3, pp. 619–621, 2000.

[172] T. Shioya, "Neutron Diffraction Study of Cathode Materials for Lithium Ion Batteries," Tsukuba, 2011.

[173] A. Svirinovsky-Arbeli, M. Juelsholt, R. May, Y. Kwon, and L. E. Marbella, "Using NMR spectroscopy to link structure to function at the Li solid electrolyte interphase," *Joule*, 2024, doi: 10.1016/j.joule.2024.04.016.

[174] K. Gerwert and C. Kotting, "Fourier transform infrared (FTIR) spectroscopy," in *Encyclopedia of Life Sciences (ELS)*, no. 2–3, Chichester: John Wiley & Sons, Ltd, 2010. doi: 10.1002/9780470015902.a0003112.pub2.

[175] A. R. Neale, D. C. Milan, F. Braga, I. V. Sazanovich, and L. J. Hardwick, "Lithium Insertion into Graphitic Carbon Observed via Operando Kerr-Gated Raman Spectroscopy Enables High State of Charge Diagnostics," *ACS Energy Lett*, vol. 7, no. 8, pp. 2611–2618, 2022, doi: 10.1021/acsenergylett.2c01120.

[176] R. Baddour-Hadjean and J. P. Pereira-Ramos, "New structural approach of lithium intercalation using Raman spectroscopy," *J Power Sources*, vol. 174, no. 2, pp. 1188–1192, 2007, doi: 10.1016/j.jpowsour.2007.06.177.

[177] K. P. Abhilash, P. Sivaraj, P. C. Selvin, B. Nalini, and K. Somasundaram, "Investigation on spin coated LLTO thin film nano-electrolytes for rechargeable lithium ion batteries," *Ceram Int*, vol. 41, no. 10, pp. 13823–13829, 2015, doi: 10.1016/j.ceramint.2015.08.067.

[178] F. A. Stevie and C. L. Donley, "Introduction to x-ray photoelectron spectroscopy," *Journal of Vacuum Science & Technology A: Vacuum, Surfaces, and Films*, vol. 38, no. 6, 2020, doi: 10.1116/6.0000412.

[179] L. E. Strange, M. H. Engelhard, C. D. Easton, J. M. Kim, and D. R. Baer, "Surface analysis insight note: X-ray photoelectron spectroscopy analysis of battery electrodes—Challenges with nickel–manganese–cobalt and Li examples using an Al Kα x-ray source," *Surface and Interface Analysis*, vol. 55, no. 10, pp. 715–729, 2023, doi: 10.1002/sia.7237.

[180] K. N. Wood and G. Teeter, "XPS on Li-Battery-Related Compounds: Analysis of Inorganic SEI Phases and a Methodology for Charge Correction," *ACS Appl Energy Mater*, vol. 1, no. 9, pp. 4493–4504, 2018, doi: 10.1021/acsaem.8b00406.

[181] Y. Waseda, E. Matsubara, and K. Shinoda, *X-Ray Diffraction Crystallography*. Berlin, Heidelberg: Springer Berlin Heidelberg, 2011.

[182] A. C. Sutorik, M. D. Green, C. Cooper, J. Wolfenstine, and G. Gilde, "The comparative influences of structural ordering, grain size, Li-content, and bulk density on the Li^+-conductivity of $Li_{0.29}La_{0.57}TiO_3$," *J Mater Sci*, vol. 47, no. 19, pp. 6992–7002, 2012, doi: 10.1007/s10853-012-6650-5.

[183] A. A. Ammann, "Inductively coupled plasma mass spectrometry (ICP MS): a versatile tool," *Journal of Mass Spectrometry*, vol. 42, no. 4, pp. 419–427, 2007, doi: 10.1002/jms.1206.

[184] J. W. Olesik, "Elemental analysis using ICP-OES and ICM/MS," *Anal Chem*, vol. 63, no. 1, pp. 12A-21A, 1991.

[185] J. Koch and D. Günther, "Laser Ablation Inductively Coupled Plasma Mass Spectrometry," in *Encyclopedia of Spectroscopy and Spectrometry*, Elsevier, 2017, pp. 526–532. doi: 10.1016/B978-0-12-803224-4.00024-8.

[186] O. Laurent, M. Guillong, C. A. Heinrich, K. Neubauer, and C. Stephan, "Advantages of a fast-scanning quadrupole for LA-ICP-MS analysis of fluid inclusions," *J Anal At Spectrom*, vol. 36, no. 10, pp. 2043–2050, 2021, doi: 10.1039/D1JA00193K.

[187] M. Bonta, A. Limbeck, C. D. Quarles Jr, D. Oropeza, R. E. Russo, and J. J. Gonzalez, "A metric for evaluation of the image quality of chemical maps derived from LA-ICP-MS experiments," *J Anal At Spectrom*, vol. 30, no. 8, pp. 1809–1815, 2015, doi: 10.1039/C5JA00056D.

[188] J. T. Van Elteren, V. S. Šelih, and M. Šala, "Insights into the selection of 2D LA-ICP-MS (multi)elemental mapping conditions," *J Anal At Spectrom*, vol. 34, no. 9, pp. 1919–1931, 2019, doi: 10.1039/c9ja00166b.

[189] W. Zhou and L. Z. Wang, Eds., *Scanning Microscopy for Nanotechnology Techniques and Applications*, 1st ed. New York: Springer New York, 2007.

[190] C. Zhang, Y. Feng, Z. Han, S. Gao, M. Wang, and P. Wang, "Electrochemical and Structural Analysis in All-Solid-State Lithium Batteries by Analytical Electron Microscopy: Progress and Perspectives," *Advanced Materials*, vol. 32, no. 27, 2020, doi: https://doi.org/10.1002/adma.201903747.

[191] D. A. Muller, "Structure and bonding at the atomic scale by scanning transmission electron microscopy," *Nat Mater*, vol. 8, no. 4, pp. 263–270, 2009, doi: 10.1038/nmat2380.

[192] A. R. Lupini *et al.*, "Chapter 2: Scanning transmission electron microscopy," in *Nanocharacterisation*, no. 37, Royal Society of Chemistry, 2015, pp. 30–79. doi: 10.1039/9781782621867-00030.

[193] S. J. Pennycook and P. D. Nellist, Eds., *Scanning Transmission Electron Microscopy: Imaging and Analysis*. Oxford: Springer Science+Business Media, 2011.

[194] S. J. Pennycook, "Z-Contrast Transmission Electron Microscopy: Direct Atomic Imaging of Materials," *Annual Review of Materials Science*, vol. 22, no. 1, pp. 171–195, 1992, doi: 10.1146/annurev.ms.22.080192.001131.

[195] P. Yang, Z. Li, Y. Yang, R. Li, L. Qin, and Y. Zou, "Effects of Electron Microscope Parameters and Sample Thickness on High Angle Annular Dark Field Imaging," *Scanning*, vol. 2022, pp. 1–9, 2022, doi: 10.1155/2022/8503314.

[196] J. Woo, A. Orisevich, C. Koch, and V. V Guliants, "Quantitative Analysis of HAADF-STEM Images of MoVTeTaO M1 Phase Catalyst for Propane Ammoxidation to Acrylonitrile," *ChemCatChem*, vol. 7, pp. 3731–3737, 2015.

[197] N. Nakanishi, "Retrieval process of high-resolution HAADF-STEM images," *J Electron Microsc (Tokyo)*, vol. 51, no. 6, pp. 383–390, 2002, doi: 10.1093/jmicro/51.6.383.

[198] K. Watanabe *et al.*, "Atomic-resolution incoherent high-angle annular dark field STEM images of Si(011)," *Phys Rev B*, vol. 63, no. 8, p. 085316, 2001, doi: 10.1103/PhysRevB.63.085316.

[199] M. D. Croitoru, D. Van Dyck, S. Van Aert, S. Bals, and J. Verbeeck, "An efficient way of including thermal diffuse scattering in simulation of scanning transmission electron microscopic images," *Ultramicroscopy*, vol. 106, no. 10, pp. 933–940, 2006, doi: 10.1016/j.ultramic.2006.04.006.

[200] M. Shiojiri, "Imaging of High-Angle Annular Dark Field Scanning Transmission Electron Microscopy and Microscopy Studies of GaN-based Light Emitting Diodes and Laser Diodes," *Chiang Mai J. Sci.*, vol. 35, no. 3, pp. 495–520, 2008.

[201] D. O. Klenov and S. Stemmer, "Contributions to the contrast in experimental high-angle annular dark-field images," *Ultramicroscopy*, vol. 106, no. 10, pp. 889–901, 2006, doi: 10.1016/j.ultramic.2006.03.007.

[202] J. J. Liu, "Advances and Applications of Atomic-Resolution Scanning Transmission Electron Microscopy," *Microscopy and Microanalysis*, vol. 27, no. 5, pp. 943–995, 2021, doi: 10.1017/S1431927621012125.

[203] X. Wu, M. D. Robertson, M. Kawasaki, and J. M. Baribeau, "Effects of small specimen tilt and probe convergence angle on ADF-STEM image contrast of $Si_{0.8}Ge_{0.2}$ epitaxial strained layers on (100) Si," *Ultramicroscopy*, vol. 114, pp. 46–55, 2012, doi: 10.1016/j.ultramic.2012.01.001.

[204] J. Y. Zhang, J. Hwang, B. J. Isaac, and S. Stemmer, "Variable-angle high-angle annular dark-field imaging: Application to three-dimensional dopant atom profiling," *Sci Rep*, vol. 5, 2015, doi: 10.1038/srep12419.

[205] N. Baladés *et al.*, "Influence of the crosstalk on the intensity of HAADF-STEM images of quaternary semiconductor materials," *J Microsc*, vol. 273, no. 1, pp. 81–88, 2019, doi: 10.1111/jmi.12763.

[206] G. R. Anstis, D. Q. Cai, and D. J. H. Cockayne, "Limitations on the s-state approach to the interpretation of sub-angstrom resolution electron microscope images and microanalysis," *Ultramicroscopy*, vol. 94, no. 3–4, pp. 309–327, 2003, doi: 10.1016/S0304-3991(02)00341-8.

[207] C. Wouters, T. Markurt, M. Albrecht, E. Rotunno, and V. Grillo, "Influence of 2s Bloch wave state excitations on quantitative HAADF STEM imaging," *Phys Rev B*, vol. 100, no. 18, 2019, doi: 10.1103/PhysRevB.100.184106.

[208] B. D. Esser *et al.*, "Quantitative STEM Imaging of Order-Disorder Phenomena in Double Perovskite Thin Films," *Phys Rev Lett*, vol. 117, no. 17, pp. 1–5, 2016, doi: 10.1103/PhysRevLett.117.176101.

[209] K. A. Mkhoyan, S. E. Maccagnano-Zacher, E. J. Kirkland, and J. Silcox, "Effects of amorphous layers on ADF-STEM imaging," *Ultramicroscopy*, vol. 108, no. 8, pp. 791–803, 2008, doi: 10.1016/j.ultramic.2008.01.007.

[210] T. Grieb *et al.*, "Quantitative HAADF STEM of SiGe in presence of amorphous surface layers from FIB preparation," *Ultramicroscopy*, vol. 184, pp. 29–36, 2018, doi: 10.1016/j.ultramic.2017.09.012.

[211] T. Yamazaki, K. Watanabe, A. Recnik, M. Ceh, M. Kawasaki, and M. Shiojiri, "Simulation of atomic-scale high-angle annular dark field scanning transmission

electron microscopy images," *J Electron Microsc (Tokyo)*, vol. 49, no. 6, pp. 753–759, 2000, doi: 10.1093/oxfordjournals.jmicro.a023868.

[212] S. Hillyard and J. Silcox, "Detector geometry, thermal diffuse scattering and strain effects in ADF STEM imaging," *Ultramicroscopy*, vol. 58, pp. 6–17, 1995.

[213] D. A. Blom, X. Li, S. Mitra, T. Vogt, and D. J. Buttrey, "STEM HAADF Image Simulation of the Orthorhombic M1 Phase in the Mo-V-Nb-Te-O Propane Oxidation Catalyst," *ChemCatChem*, vol. 3, no. 6, pp. 1028–1033, 2011, doi: 10.1002/cctc.201100049.

[214] K. Watanabe, "Theory for HAADF-STEM and its Image Simulation," in *Scanning Transmission Electron Microscopy of Nanomaterials*, 2014, pp. 179–216.

[215] R. F. Loane, P. Xu, and J. Silcox, "Incoherent imaging of zone axis crystals with ADF STEM," *Ultramicroscopy*, vol. 40, pp. 121–138, 1992.

[216] J. M. LeBeau and S. Stemmer, "Experimental quantification of annular dark-field images in scanning transmission electron microscopy," *Ultramicroscopy*, vol. 108, no. 12, pp. 1653–1658, 2008, doi: 10.1016/j.ultramic.2008.07.001.

[217] P. D. Robb and A. J. Craven, "Column ratio mapping: A processing technique for atomic resolution high-angle annular dark-field (HAADF) images," *ltramicroscopy*, vol. 109, no. 1, pp. 61–69, 2008, doi: 10.1016/j.ultramic.2008.08.001.

[218] J. Verbeeck, S. Hens, P. Potapov, and D. Schryvers, "Electron Energy Loss Spectrometry," in *Encyclopedia of Analytical Science*, Elsevier, 2005, pp. 324–331. doi: 10.1016/B0-12-369397-7/00605-1.

[219] J. A. Hunt and D. B. Williams, "Electron energy-loss spectrum-imaging," *Ultramicroscopy*, vol. 38, no. 1, pp. 47–73, 1991, doi: 10.1016/0304-3991(91)90108-I.

[220] J. M. LeBeau and S. Stemmer, "Experimental quantification of annular dark-field images in scanning transmission electron microscopy," *Ultramicroscopy*, vol. 108, no. 12, pp. 1653–1658, 2008, doi: 10.1016/j.ultramic.2008.07.001.

[221] A. Benčan, G. Dražić, H. Uršič, M. Makarovič, M. Komelj, and T. Rojac, "Domain-wall pinning and defect ordering in $BiFeO_3$ probed on the atomic and nanoscale," *Nat Commun*, vol. 11, no. 1, 2020, doi: 10.1038/s41467-020-15595-0.

[222] C. Koch, "Determination of core structure periodicity and point defect density along dislocations," Doctoral Degree, Arizona State University, 2002.

[223] K. Momma and F. Izumi, "VESTA 3 for three-dimensional visualization of crystal, volumetric and morphology data," *J Appl Crystallogr*, vol. 44, no. 6, pp. 1272–1276, 2011, doi: 10.1107/S0021889811038970.

[224] M. J. Hytch, "Geometric phase analysis high resolution electron microscope images," *Scanning Microsc*, vol. 11, pp. 53–66, 1997.

[225] M. J. Hytch, E. Snoeck, and R. Kilaas, "Quantitative measurement of displacement and strain fields from HREM micrographs," *Ultramicroscopy*, vol. 74, pp. 131–146, 1998.

[226] J. T. van Elteren, M. Šala, and D. Metarapi, "Comparison of single pulse, multiple dosage, and 2D oversampling / deconvolution LA-ICPMS strategies for mapping of (ultra)low-concentration samples," *Talanta*, vol. 235, 2021, doi: 10.1016/j.talanta.2021.122785.

[227] A. D. Becke, "Density-functional exchange-energy approximation with correct asymptotic behavior," *Phys Rev A*, vol. 38, no. 6, pp. 3098–3100, 1988.

[228] J. P. Perdew, K. Burke, and M. Ernzerhof, "Generalized Gradient Approximation Made Simple," *Phys Rev Lett*, vol. 77, no. 18, 1996.

[229] P. E. Blochl, "Projector augmented-wave method," *Phys Rev B*, vol. 50, no. 24, 1994.

[230] G. Kresse and J. Furthmuller, "Efficiency of ab-initio total energy calculations for metals and semiconductors using a plane-wave basis set," *Comput Mater Sci*, vol. 6, pp. 15–50, 1996.

[231] G. Kresse and J. Furthmuller, "Efficient iterative schemes for ab initio total-energy calculations using a plane-wave basis set," *Phys Rev B*, vol. 54, no. 16, 1996.

[232] C. an Lin *et al.*, "Low-temperature sintering of $Li_{0.33}La_{0.55}TiO_3$ electrolyte for all-solid-state Li batteries," *J Eur Ceram Soc*, vol. 43, no. 16, pp. 7543–7552, 2023, doi: 10.1016/j.jeurceramsoc.2023.08.018.

[233] A. Jain *et al.*, "Commentary: The materials project: A materials genome approach to accelerating materials innovation," *APL Mater*, vol. 1, 2013, doi: 10.1063/1.4812323.

[234] C. A. Lin, R. N. Nasara, and S. K. Lin, "Ab Initio Exploration of Co-Free Layered Oxides as Cathode Materials in Li Ion Batteries," *ACS Sustain Chem Eng*, vol. 9, no. 34, pp. 11342–11350, 2021, doi: 10.1021/acssuschemeng.1c02861.

[235] G. Izquierdo and A. R. West, "Phase equilibria in the system Li_2O-TiO_2," *Mater Res Bull*, vol. 15, no. 11, pp. 1655–1660, 1980, doi: 10.1016/0025-5408(80)90248-2.

[236] T. Zinkevich, B. Schwarz, P. Braun, A. Weber, H. Ehrenberg, and S. Indris, "Effect of sintering temperature on Li diffusivity in $Li_{0.29}La_{0.57}TiO_3$: Local hopping and long-range transport," *Solid State Ion*, vol. 357, p. 115486, 2020, doi: 10.1016/j.ssi.2020.115486.

[237] H. Geng, J. Lan, A. Mei, Y. Lin, and C. W. Nan, "Effect of sintering temperature on microstructure and transport properties of $Li_{3x}La_{2/3-x}TiO_3$ with different lithium contents," *Electrochim Acta*, vol. 56, no. 9, pp. 3406–3414, 2011, doi: 10.1016/j.electacta.2010.06.031.

[238] D. Tirupathi Swamy, K. Ephraim Babu, and V. Veeraiah, "Evidence for high ionic conductivity in lithium-lanthanum titanate, $Li_{0.29}La_{0.57}TiO_3$," *Bulletin of Materials Science*, vol. 36, no. 6, pp. 1115–1119, 2013, doi: 10.1007/s12034-013-0551-3.

[239] J. G. Kim, H. G. Kim, and H. T. Chung, "Microstructure-ionic conductivity relationships in perovskite lithium lanthanum titanate," *J Mater Sci Lett*, vol. 18, no. 6, pp. 493–496, 1999, doi: 10.1023/A:1006606817633.

[240] D. L. Lu *et al.*, "Investigations on the properties of $Li_{3x}La_{2/3-x}TiO_3$ based all-solid-state supercapacitor: Relationships between the capacitance, ionic conductivity, and temperature," *J Eur Ceram Soc*, vol. 40, no. 6, pp. 2396–2403, 2020, doi: 10.1016/j.jeurceramsoc.2020.02.006.

[241] D. W. Richerson and W. E. Lee, *Modern Ceramic Engineering*. Boca Raton: CRC Press is an imprint of the Taylor & Francis Group, an informa business, 2018.

[242] B. V. Beznosikov and K. S. Aleksandrov, "Perovskite-Like Crystals of the Ruddlesden–Popper Series," *Crystallography Reports*, vol. 45, no. 5, pp. 792–798, 2000.

[243] S. N. Ruddlesden and P. Popper, "New compounds of the K_2NiF_4 type," *Acta Crystallographica* , vol. 10, pp. 538–539, 1957.

[244] J. Woo, A. Borisevich, C. Koch, and V. V. Guliants, "Quantitative Analysis of HAADF-STEM Images of MoVTeTaO M1 Phase Catalyst for Propane Ammoxidation to Acrylonitrile," *ChemCatChem*, vol. 7, pp. 3731–3737, 2015, doi: 10.1002/cctc.201500402.

[245] L. J. Allen, S. D. Findlay, M. P. Oxley, and C. J. Rossouw, "Lattice-resolution contrast from a focused coherent electron probe. Part I," *Ultramicroscopy*, vol. 96, no. 1, pp. 47–63, 2003, doi: 10.1016/S0304-3991(02)00380-7.

[246] S. Peng *et al.*, "Intrinsic layered defects in solid-state electrolyte $Li_{0.33}La_{0.56}TiO_3$," *Mater Today Energy*, vol. 23, p. 100912, 2022, doi: 10.1016/j.mtener.2021.100912.

[247] G. T. Martinez *et al.*, "Quantitative STEM normalisation: The importance of the electron flux," *Ultramicroscopy*, vol. 159, no. P1, pp. 46–58, 2015, doi: 10.1016/j.ultramic.2015.07.010.

[248] B. H. Zhang, D. Xu, B. H. Chen, X. Q. Liu, J. R. Hester, and X. M. Chen, "Hybrid improper ferroelectricity in A -site cation ordered $Li_2La_2Ti_3O_{10}$ ceramic with triple-layer Ruddlesden-Popper structure," *Appl Phys Lett*, vol. 118, no. 5, pp. 1–6, 2021, doi: 10.1063/5.0038142.

[249] R. E. Schaak and T. E. Mallouk, "Topochemical synthesis of three-dimensional perovskites from lamellar precursors," *J Am Chem Soc*, vol. 122, no. 12, pp. 2798–2803, 2000, doi: 10.1021/ja993306i.

[250] M. J. Hytch, E. Snoeck, and R. Kilaas, "Quantitative measurement of displacement and strain fields from HREM micrographs," *Ultramicroscopy*, vol. 74, pp. 131–146, 1998.

[251] T. Tanaka, K. Matsunaga, Y. Ikuhara, and T. Yamamoto, "First-principles study on structures and energetics of intrinsic vacancies in $SrTiO_3$," *Phys Rev B Condens Matter Mater Phys*, vol. 68, no. 20, 2003, doi: 10.1103/PhysRevB.68.205213.

[252] J. He and S. B. Sinnott, "Ab initio calculations of intrinsic defects in rutile TiO_2," *Journal of the American Ceramic Society*, vol. 88, no. 3, pp. 737–741, 2005, doi: 10.1111/j.1551-2916.2005.00107.x.

[253] M. Maček Kržmanc *et al.*, "$SrTiO_3/Bi_4Ti_3O_{12}$ Nanoheterostructural Platelets Synthesized by Topotactic Epitaxy as Effective Noble-Metal-Free Photocatalysts for pH-Neutral Hydrogen Evolution," *ACS Appl Mater Interfaces*, vol. 13, no. 1, pp. 370–381, 2021, doi: 10.1021/acsami.0c16253.

[254] S. Šturm, M. Shiojiri, and M. Čeh, "Atomic-scale structural and compositional analyses of Ruddlesden-Popper planar faults in AO-excess $SrTiO_3$ (A = Sr^{2+}, Ca^{2+}, Ba^{2+}) ceramics," *J Mater Res*, vol. 24, no. 8, pp. 2596–2604, 2009, doi: 10.1557/jmr.2009.0321.

[255] J. Moškon, J. Žuntar, S. Drvarič Talian, R. Dominko, and M. Gaberšček, "A Powerful Transmission Line Model for Analysis of Impedance of Insertion Battery

Cells: A Case Study on the NMC-Li System," *J Electrochem Soc*, vol. 167, no. 14, p. 140539, 2020, doi: 10.1149/1945-7111/abc769.

[256] R. Morasch, J. Keilhofer, H. A. Gasteiger, and B. Suthar, "Methods—Understanding Porous Electrode Impedance and the Implications for the Impedance Analysis of Li-Ion Battery Electrodes," *J Electrochem Soc*, vol. 168, no. 8, p. 080519, 2021, doi: 10.1149/1945-7111/ac1892.

[257] S. Devan, V. R. Subramanian, and R. E. White, "Analytical Solution for the Impedance of a Porous Electrode," *J Electrochem Soc*, vol. 151, no. 6, p. A905, 2004, doi: 10.1149/1.1739218.

[258] P. Braun, C. Uhlmann, A. Weber, H. Störmer, D. Gerthsen, and E. Ivers-Tiffée, "Separation of the bulk and grain boundary contributions to the total conductivity of solid lithium-ion conducting electrolytes," *J Electroceram*, vol. 38, no. 2–4, pp. 157–167, 2017, doi: 10.1007/s10832-016-0061-y.

[259] M. Shirpour, R. Merkle, C. T. Lin, and J. Maier, "Nonlinear electrical grain boundary properties in proton conducting Y-$BaZrO_3$ supporting the space charge depletion model," *Physical Chemistry Chemical Physics*, vol. 14, no. 2, pp. 730–740, 2012, doi: 10.1039/c1cp22487e.

[260] E. A. Fortalnova *et al.*, "Microstructure and ionic conductivity of $(La_{1/2}Li_{1/3+x})TiO_3$ perovskite-like solid solutions," *Inorganic Materials*, vol. 43, no. 10, pp. 1103–1108, 2007, doi: 10.1134/S0020168507100135.

[261] Q. Y. Wu, D. Y. Zheng, R. Y. Mao, C. Liu, X. Wang, and W. B. Han, "Influence of tetragonal/cubic phase composition on the total ionic conductivity of Li3xLa2/3−xTiO3," *AIP Adv*, vol. 13, no. 10, 2023, doi: 10.1063/5.0161316.

[262] L. D. Trong, T. T. Thao, and N. N. Dinh, "Characterization of the Li-ionic conductivity of $La_{(2/3-x)}Li_{3x}TiO_3$ ceramics used for all-solid-state batteries," *Solid State Ion*, vol. 278, pp. 228–232, 2015, doi: 10.1016/j.ssi.2015.05.027.

[263] F. Aguesse, J. M. López Del Amo, V. Roddatis, A. Aguadero, and J. A. Kilner, "Enhancement of the grain boundary conductivity in ceramic $Li_{0.34}La_{0.55}TiO_3$ electrolytes in a moisture-free processing environment," *Adv Mater Interfaces*, vol. 1, no. 7, pp. 1–9, 2014, doi: 10.1002/admi.201300143.

[264] J. F. Wu and X. Guo, "Origin of the low grain boundary conductivity in lithium ion conducting perovskites: $Li_{3x}La_{0.67-x}TiO_3$," *Physical Chemistry Chemical Physics*, vol. 19, no. 8, pp. 5880–5887, 2017, doi: 10.1039/c6cp07757a.

[265] J. C. M. Madrid, A. Jonderian, E. McCalla, and K. K. Ghuman, "Impact of TiO_2 at the Grain Boundaries in Lithium Lanthanum Titanate Solid Electrolytes," *ACS Appl Energy Mater*, 2024, doi: 10.1021/acsaem.4c00883.

Bibliography

Original Scientific Articles

P. Borštnar, G. Dražić, M. Šala, C. Lin, S. Lin, M. Spreitzer, N. Daneu. "Transient Ruddlesden–Popper-Type Defects and Their Influence on Grain Growth and Properties of Lithium Lanthanum Titanate Solid Electrolyte," *ACS Nano*, vol. 18, no. 16, pp. 10850–10862, 2024, doi:10.1021/acsnano.4c00706.

P. Borštnar, J. Žuntar, M. Spreitzer, G. Dražić, N. Daneu. "Exaggerated grain growth and the development of coarse-grained microstructures in lithium lanthanum titanate perovskite ceramics," *Journal of the European Ceramic Society*, vol. 43, iss. 3, pp. 1017-1027, 2023, https://doi.org/10.1016/j.jeurceramsoc.2022.11.004.

Published Scientific Conference Contribution Abstracts

P. Borštnar, G. Dražić, M. Spreitzer, N. Daneu. "Effect of amorphous layer on HAADF-STEM image contrast," in *5. slovensko posvetovanje mikroskopistov*, Rogla, Slovenia, 2024.

P. Borštnar, M. Spreitzer, N. Daneu. "Quantitative STEM analysis of Ruddlesden-Popper-type defects in $Li_{3x}La_{2/3-x}TiO_3$ solid electrolyte," in *20th International Microscopy Congress*, Busan, Korea, 2023.

P. Borštnar, M. Spreitzer, N. Daneu. "HAADF-STEM characterization of $Li_{(3x)}La_{(2/3-x)}TiO_3$ solid electrolyte with lithium-rich RP-defects," in *International Workshop on the Characterisation and Quantification of Lithium from the Micro- to the Nano-Scale, from Mining to Energy,* Paris, France, 2023.

P. Borštnar, M. Spreitzer, N. Daneu. "Characterization of polytypic defects in $Li_{3x}La_{2/3-x}TiO_3$," in *15th Jožef Stefan International Postgraduate School Students' Conference,* Kamnik, Slovenia, 2023.

P. Borštnar, M. Spreitzer, G. Dražić, N. Daneu. "Atomic-scale characterization of polytypic defects in $Li_{0.33}La_{0.56}TiO_3$," in *16th Multinational Congress on Microscopy,* Brno, Czech Republic, 2022.

P. Borštnar, M. Spreitzer, G. Dražić, N. Daneu. "HAADF-STEM analysis of Ruddlesden-Popper-type defects in nonstoichiometric $Li_{0.33}La_{0.56}\square_{0.11}TiO_3$," in *4. slovensko posvetovanje mikroskopistov*, Ankaran, Slovenia, 2022.

P. Borštnar, M. Spreitzer, N. Daneu. "Tailoring the microstructure of $Li_{0.33}La_{0.56}\square_{0.11}TiO_3$ through exaggerated grain growth," in *14th Jožef Stefan International Postgraduate School Students' Conference,* Kamnik, Slovenia, 2022.

P. Borštnar, M. Spreitzer, G. Dražić, N. Daneu. “Synthesis and characterization of $Li_{3x}La_{2/3-x}TiO_3$ ceramics for applications in all-solid-state batteries,” in *13th Jožef Stefan International Postgraduate School Students' Conference and 15th Young Researchers' Day of Chemistry, material science, biochemistry and environment,* Ljubljana, Slovenija, 2021.

Biography

Petruša Borštnar completed her bachelor and master studies in Geology at the Faculty of Natural Sciences and Engineering, University of Ljubljana, Slovenia. In October 2020, she enrolled in a doctoral study program of Nanosciences and Nanotechnologies at the Jožef Stefan International Postgraduate School and began working as a young researcher in the Advanced Materials Department at Jožef Stefan Institute in Ljubljana, Slovenia. Her research is primarily focused on the solid-state synthesis and analysis of ceramics and thin films using various characterization techniques, with an emphasis on scanning and transmission electron microscopy and quantitative analysis of atomic-scale images using simulations.